Organic-Inorganic Interfaces for Applications in Organic Electronics

Von der Fakultät für Mathematik und Physik
der Universität Stuttgart
zur Erlangung der Würde eines Doktors der Naturwissenschaften
(Dr. rer. nat.) genehmigte Abhandlung

Vorgelegt von

STEFAN SELLNER

aus Rottweil

Hauptberichter:	Prof. Dr. H. Dosch
Mitberichter:	Prof. Dr. J. Wrachtrup

Eingereicht am:	04.10.2005
Tag der Mündlichen Prüfung:	16.12.2005

Institut für Theoretische und Angewandte Physik
der Universität Stuttgart

2006

Contents

1 Deutsche Zusammenfassung

1.1 Motivation

Die halbleitenden Eigenschaften π-konjugierter organischer Moleküle sind seit Beginn des letzten Jahrhunderts bekannt [1–3], erfahren aber insbesondere in jüngerer Zeit große Aufmerksamkeit aufgrund ihrer elektrischen und optischen Eigenschaften [4–8]. Die Möglichkeit, solche organischen Halbleiter bei niedrigen Substrattemperaturen und großflächig [6,9] aufzubringen eröffnet neue Anwendungsmöglichkeiten wie zum Beispiel organische Leuchtdioden und organische Feldeffekttransistoren.

Für die Anwendung in organischen Feldeffekttransistoren eignen sich insbesondere kleine aromatische Moleküle die, unter Ultrahoch-Vakuum Bedingungen sublimiert, hochgeordnete dünne Filme ausbilden können. Die elektrischen Charakteristika solcher Bauelement werden unter anderem durch die strukturelle Ordnung der organischen Schicht und ihrer Grenzflächen mit den anorganischen Materialien (Kontakte und Isolatorschicht) beeinflußt. Daher kommt der Präparation und Charakterisierung der organischen und anorganischen Schichten eine wichtige Rolle zu.

Solche Bauelemente sind allerdings empfindlich gegenüber Umgebungsgasen und erhöhten Temperaturen. Geeignete Einkapselungen stellen daher eine Möglichkeit dar, die elektrischen und optischen Eigenschaften organischer Bauelemente zu konservieren und deren Langlebigkeit zu erhöhen [10].

Aluminiumoxidschichten finden aufgrund ihrer außergewöhnlichen Materialeigenschaften (hohe thermische Stabilität, hohe Dielektrizitätskonstante und hohe Härte, um nur einige zu nennen) zunehmend Anwendung in der Industrie. So werden Aluminiumoxideschichten zum Beispiel zur Beschichtung von Lebensmittelverpackungen verwendet, und in der Mikroelektronik dienen Aluminiumoxidschichten seit langem schon als Isolatorschichten. Aus diesen Gründen stellt Aluminiumoxid ein mögliches Material zur Einkapselung von organischen Bauelementen dar. Allerdings muß sich erst erweisen, ob

die Aufbringung von Aluminiumoxidschichten auf organische Bauelemente deren elektrische Eigenschaften beeinträchtigen oder nicht. Eine gut definierte Grenzfläche zum organischen Film und deren thermische Stabilität ist dabei zwingend erforderlich.

Ziel dieser Arbeit ist die Untersuchung der Grenzfächen des organischen Halbleiters Diindenoperylen (DIP) mit Metal- und Isolatorschichten und die Untersuchung von gesputterten Aluminiumoxidschichten als mögliches Material zur Einkapselung von organischen Bauelementen wie zum Beispiel organische Leuchtdioden (OLEDs) oder organische Feldeffekttransistoren (OFETs). Die Präparation und Charakterisierung von auf DIP Filmen gesputterten Aluminiumoxidschichten und die Untersuchung der thermischen Stabilität solcher anorganisch/organischen Heterostrukturen war dabei im Fokus dieser Arbeit. Eine vorhergehende Untersuchung des Wachstums, der Struktur und Morphologie von organischen Filmen war dabei unerläßlich.

1.2 Experimentelle Ergebnisse

Die Untersuchung der thermischen Stabilität mit Aluminiumoxidschichten eingekapselter organischer Filme setzt voraus, daß Morphologie und Struktur der organischen Filme vor und nach Aufbringen der Aluminiumoxiddeckschicht gut charakterisiert wurden. Deshalb ging dem Hauptteil dieser Arbeit, der Untersuchung der thermischen Stabilität eingekapselter organischer Filme, eine ausführliche Untersuchung des Wachstums und der Struktur organischer Halbleiterfilme voraus. Außerdem mußten die Präparationsbedingungen für gesputterte Aluminiumoxidschichten so gewählt werden, daß der organische Film während des Sputterns so wenig wie möglich beeinträchtigt wird und eine gut definierte Grenzfäche zwischen Oxid und organischem Film gewährleistet ist. Die Aluminiumoxidschichten wurden aus diesen Gründen durch Aufbringen direkt auf Siliziumoxidsubstraten optimiert unter dem Gesichtspunkt, daß auch eine Präparation auf organischen Filmen möglich ist. Nach Optimierung der Präparationsparameter wurden Aluminiumoxiddeckschichten auf zuvor präparierten DIP Filme aufgesputtert und die resultierende anorganische/organische Heterostruktur untersucht. Nach ausreichender Charakterisierung wurde das thermische Verhalten dieser Schichtsysteme mit unterschiedlichen Meßmethoden untersucht.

1.2.1 Untersuchung organischer Filme

Bevor komplexere anorganisch/organische Heterostrukturen untersucht werden konnten, mußte die Struktur der organischen Filme kontrolliert werden. Deshalb untersuchten wir das Wachstum, die Struktur und die Morphologie von DIP Filmen auf Siliziumoxidsubstraten und verglichen diese mit Filmen des perfluorierten Kupfer-Phthalocyanins (F_{16}CuPc) und des Pentacens.

F_{16}CuPc bildet bei Substrattemperaturen von $T_{substr.} = 230\,°C$ nadelförmige hochkristalline Strukturen aus mit einem Netzebenabstand von $d_{\perp} = 14.4\,Å$. Pentacenfilme, die bei $T_{substr.} = 40\,°C$ präpariert wurden, bilden hingegen große Terrassen monomolekularen Abstandes. Der Netzebenenabstand für die Dünnfilmphase beträgt 15.48 Å. Unter optimalen Präparationsbedingungen ($T_{substr.} = 145\,°C$, $R = 12\,Å/min$) [11, 12], bilden DIP Filme auf Siliziumoxid hochgeordnete Filme mit vielversprechenden elektrischen Eigenschaften. Aus Röntgenstreuuntersuchungen der Struktur von DIP Filmen in Abhängigkeit von den Präparationsbedingungen, insbesondere der Substrattemperatur und der Wachstumsrate, konnten Informationen über das Wachstum dieser Filme gewonnen werden. Sowohl die Substrattemperatur als auch die Wachstumsrate zeigten nicht nur einen Einfluß auf die Rauhigkeit, sondern auch auf die gesamt Filmstruktur. Dünne Filme des organischen Halbleiters DIP stellen ein sehr geeignetes System zur weiteren Untersuchung der Wechselwirkung mit anorganischen Schichten, wie zum Beispiel den Deckelschichten aus Aluminiumoxid, dar.

1.2.2 Anorganisch-organische Heterostrukturen

In einem ersten Teil untersuchten wir Aluminiumoxidschichten, die mittels r.f. Magnetron Sputtern in reiner Argon Atmosphere auf SiO_x aufgebracht wurden. Die amorphen Filme zeigten eine granulare Morphologie niedriger Rauhigkeit. Aus Röntgenmessungen an Aluminiumoxidfilmen verschiedener Dicke konnte die Rauhigkeit in Abhängigkeit von der Filmdicke ermittelt werden und daraus konnte ein Wachstumsexponent von $\beta = 0.37$ bestimmt werden. Die Stöchiometrie dieser Filme wurde mittels Rutherford Rückstreuung (RBS) ermittelt, wobei bei höherer Sputterleistung vermehrt Filme mit höherem metallischen Anteil hergestellt wurden, während bei niedrigerer Sputterleistung ein höherer Sauerstoffanteil festgestellt wurde.

In einem zweiten Teil wurden anorganisch/organische Heterostrukturen untersucht.

Als Vergleich zu den Aluminiumoxidschichten auf DIP, wurde auch das Wachstum von Gold auf DIP Filmen mittels *in-situ* Echtzeit Röntgenstreuung untersucht. Während der Verdampfung von Gold wurden dabei mehrere Messungen des spekulären Pfades durchgeführt, so daß die Veränderungen aufgrund des Filmwachstums als Funktion der Zeit aufgenommen wurden. Diese Veränderungen des spekulären Signals erwiesen sich allerdings als sehr gering. Die sehr niedrige Aufdampfrate von 0.025 Å/min und die mit zunehmender Depositionszeit leicht zunehmende Elektronendichte des DIP (ohne daß sich dabei ein geschlossener Gold Film ausbildete), deutet darauf hin, daß das aufgedampfte Gold (bei Substrattemperaturen von 18 °C) in den DIP Film eindiffundierte und homogen über die gesamte Schichtdicke verteilt war.

Eine Voraussetzung für den Einsatz von Aluminiumoxidschichten als Einkapselungen für organische Bauelemente ist eine gut definierte Grenzfläche zur organischen Schicht. Für die Anwendung in organischen Feldeffekttransistoren ist außerdem wichtig, daß die kristalline Struktur der organischen Schicht erhalten bleibt, wenn die Deckelschicht aufgesputtert wird. Mittels XRD, AFM und Transmissionselektronenmikroskopie (TEM) wurden die Struktur und Morphologie des Aluminiumoxid/DIP Systems auch im Vergleich zum System Aluminiumoxid/SiO_x untersucht. Aus den Daten geht hervor, daß Aluminiumoxid eine lateral gut definierte Grenzfläche mit den DIP Filmen ausbildet und nur wenig Diffusion in den organischen Film beobachtet werden kann. Mittels TEM konnten auch die individuellen molekularen Lagen des DIP aufgelöst werden, was die hohe strukturelle Ordnung in den DIP Filmen bestätigte. Ein Vergleich der Rauhigkeitsentwicklung entsprechend dem Skalierungsgesetz $\sigma = L^{\beta}$ ergab vergleichbare Wachstumsexponenten von $\beta = 0.37$ für Aluminiumoxid auf Siliziumoxid und $\beta = 0.34$ für Aluminiumoxid auf DIP Filmen. Die Ähnlichkeit der AFM-Bilder der Aluminiumoxidschichten auf Siliziumoxid und auf DIP, zusammen mit den vergleichbaren Werten des Wachstumsexponenten β deutet darauf hin, daß das Wachstum und die Struktur auf diesen sehr unterschiedlichen Substraten erstaunlicherweise sehr ähnlich ist [13].

1.2.3 Thermische Stabilität eingekapselter DIP Filme

Aufgrund der gut definerten Filmstruktur der Aluminiumoxid/DIP Proben führten wir Untersuchungen der thermischen Stabilität dieser Systeme durch.

Erstaunlicherweise konnte die thermische Stabilität mit Aluminiumoxid abgedeck-

ter DIP Filme stark erhöht werden [14]. Im Vergleich zur Desorptionstemperatur von DIP Filmen ohne Deckelschicht (200 °C) lässt sich die Zusammenbruchstemperatur abgedeckter DIP Filme um über 200 °C erhöhen. Dabei bleibt die kristalline Ordnung der organischen Filme bis zur Zusammenbruchstemperatur erhalten. Die Aluminiumoxidschicht wirkt offenbar als fast perfekter Deckel, der die Desorption der DIP Moleküle verhindert. Letztendlich bricht die Schichtstruktur aber bei Temperaturen zusammen, die für jede Probe spezifisch sind. Um die Frage zu klären, welche Effekte zum Zusammenbruch der Schichtstruktur führten, wurden die Dicke der Aluminiumoxidschicht, deren Stöchiometrie und die Heizrate variiert.

Aus TDS und XRD Daten geht hervor, daß die thermische Stabilität weiter erhöht werden kann, wenn dickere Aluminiumoxidschichten verwendet werden. Die Heizrate spielt für Relaxierungsprozesse, die mit den thermisch induzierten Spannungen an der Aluminiumoxid/DIP Grenzfläche konkurrieren, eine Rolle. Kleinere Heizraten erhöhen die thermische Stabilität. Da sich die thermischen und mechanischen Eigenschaften der Aluminiumoxidschichten mit ihrer Stöchiometrie ändern, hat diese auch einen Einfluß auf die thermische Stabilität der gedeckelten DIP Filme. Aus unseren Daten geht hervor, daß Deckelschichten mit höherem metallischem Anteil eine geringere Zusammenbruchstemperatur haben im Vergleich zu stöchiometrischen (Al_2O_3) Deckelschichten.

Während ungedeckelte DIP Filme bei 200 °C in einem lateral homogenen Prozeß desorbieren, fanden wir bei den abgedeckelten DIP Filmen während des gesamten Heizvorgangs eine konstante kohärente Schichtdicke, was auf einen lateral inhomogenen Desorptionsprozeß schließen läßt. Da die Desorption des abgedeckelten DIP Films an lokalen Defekten in der Deckelschicht stattfindet, stellt sich die Frage nach dem Ursprung dieser Defekte. Die TDS Daten zeigten in einem Temperaturfenster oberhalb der Desorptionstemperatur ungedeckelter DIP Filme keine Desorption, was darauf schließen läßt, daß die Defekte in der Deckelschicht thermisch induziert sind. Dies wird durch Messungen des thermischen Verhaltens der DIP Einheitszellenparameter (a, b in der Ebene und c senkrecht zur Oberfläche) bestätigt. Da sich die thermischen Expansionskoeffizienten von DIP und Aluminiumoxid um etwa eine Größenordnung unterscheiden, stellen sich an ihrer Grenzfläche starke thermische Spannungen ein. Durch die charakteristische pyramidale Terrassenstruktur der DIP Filme wirken nicht nur lateral, sondern auch vertikal Spannungen an der Aluminiumoxid/DIP Grenzfläche.

In einem möglichen Szenario für den Zusammenbruch der Schichtstruktur wer-

den durch thermische Spannungen, aber auch durch Einschlüsse von Argon in der Aluminiumoxidschicht, Risse oder Defekte thermisch induziert, die zur Desorption der darunterliegenden Moleküle führt. Wie sich durch Langzeitmessungen gezeigt hat, nimmt die Kristallinität der organischen Schicht auch bei mittleren Temperaturen als Funktion der Zeit ab. Dies bedeutet, daß auch Moleküle von gut abgedeckelten Stellen zu den Defekten diffundieren können und dann von dort desorbieren [15].

1.3 Schlußfolgerungen

Am Beispiel von hochgeordneten Filmen des organischen Halbleiters Diindenoperylen haben wir gezeigt, daß sich deren thermische Stabilität durch Deckelschichten aus gesputtertem Aluminiumoxid stark erhöhen läßt [14,15]. Durch die Einkapselung solcher organischer Schichten wird auf sehr effektive Weise die Desorption der Moleküle bei Temperaturen weit oberhalb des Desoprtionspunktes ungedeckelter DIP Filme verhindert und gleichzeitig die kristalline Struktur erhalten. Teilweise bricht das Schichtsystem erst 300 °C oberhalb der Desorptionstemperatur unabgedeckter DIP Schichten zusammen. Solche Deckelschichten sollen nicht nur die Moleküle daran hindern, bei erhöhten Temperaturen zu desorbieren, sondern sie sollen auch das Eindiffundieren von Umgebungsgasen in die organische Schicht verhindern, was zur Beeinträchtigung der elektrischen und optischen Eigenschaften organischer Bauelemente führen kann.

Die Erhöhung der thermischen Stabilität organischer Schichten durch Deckelschichten beschränkt sich nicht nur auf das spezifische System Aluminiumoxid/DIP, sondern stellt ein grundlegendes Konzept zur Stabilisierung von organischen Schichten dar. Kürzlich konnten Meyer *et al.* [16] mit Aluminiumoxid eingekapselte organische Feldeffekttransistoren basierend auf dem weitverbreiteten Molekül Pentacen bei Temperaturen oberhalb der Desorptionstemperatur von Pentacene betreiben. Wir denken deshalb, daß sich Aluminiumoxidschichten als Material zur Einkapselung organischer Bauelemente eignen. Außerdem eröffnen Deckelschichten die Möglichkeit, organische Halbleitermoleküle mit bisher für praktische Anwendungen zu niedrigen Desorptionstemperaturen zu verwenden [17]. Neben dem praktischen Nutzen von Deckelschichten möchten wir auch darauf hinweisen, daß solche Deckelschichten die Untersuchung von Materialeigenschaften oberhalb der Desorptionstemperatur des verwendenten Moleküls erlauben und daher Untersuchungen unter ansonsten unzugängliche Bedingungen erlauben.

2 Introduction

Organic semiconductors have attracted much attention in the last years and it has become clear that these materials are also promising for the application in electronic devices [4–8]. In particular, the unique possibilities offered by the tunability and synthesis of organic molecules together with the possibility of low-cost and large-area fabrication at moderate substrate temperatures appear attractive [6,9]. Some fields of applications are organic field-effect transistors (OFETs), organic light-emitting diodes (OLEDs), photovoltaic cells [18, 19] and optically pumped organic semiconductor LASERs [20]. There are two basic routes, namely polymeric systems and 'small molecules'. The solubility of many semiconducting polymers makes the ink-jet printing of electrical circuits and displays a realistic vision [21–24]. These advantages have to be balanced by the inferior semiconducting performance compared to small organic conjugated molecules.

While the first displays based on OLEDs have already turned into commercial products, the peformance characteristics of OFETs based on organic thin films still have to be improved. In particular, the charge carrier mobility, μ, which is essential for many other performance criteria such as the switching frequency and the I_{on}/I_{off} ratio between the current in the 'on' and in the 'off' state of the transistor, is far beyond what can be obtained with polycrystalline silicon technology. Therefore, improving the effective charge carrier mobility in OFETs is a major task. Nevertheless, mobilities in the range of amorphous silicon have already been obtained for OFETs based on small conjugated molecules (~ 1 cm^2/Vs) [7].

Semiconducting polymers present the advantage of solubility and therefore thin films can be produced by deposition techniques compatible with low-cost electronics. However, these films are mostly disordered and the mobilities measured in such systems are rather low. On the other side, relatively high charge carrier mobilities could be obtained from highly ordered films of small conjugated molecules evaporated in ultra-high vacuum (UHV) [7]. Obviously, the use of UHV is not compatible with the concept of true

low-cost fabrication but the preparation of highly ordered films allows to better understand the electrical transport mechanisms in such materials. Therefore, the controlled growth of highly ordered organic films is a very active field of present research.

In OFETs the charge carrier injection takes place at the organic/metal contact interface and the free charge carriers are induced at the organic/dielectric interface (see Fig. 2.1). Therefore, besides the structural order of the active (organic semiconducting) layer the organic/inorganic interfaces play a crucial role in organic thin film transistors. Inorganic materials deposited on top of organic films can diffuse into the organic film and influence the device performances [25, 26].

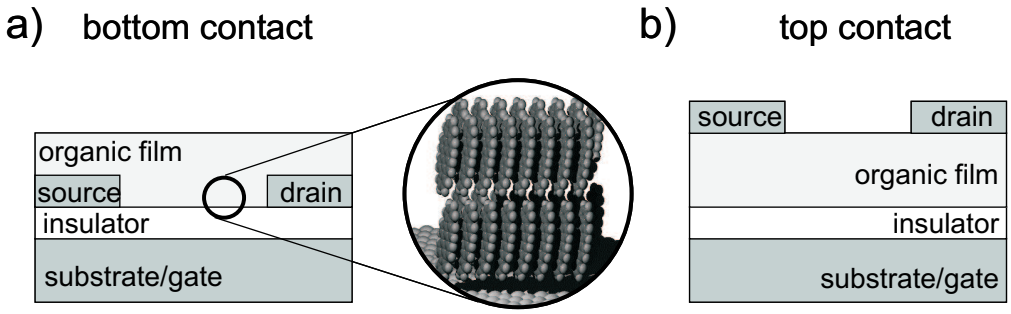

Figure 2.1: Schematic representation of frequent OFET geometries. (a) Bottom contact and (b) top contact geometry.

Besides the obvious performance requirements, the devices have to meet certain stability standards, which in some cases are actually the limiting factor of technological progress [27]. Indeed, stability at elevated temperatures, high electrical-field gradients, and against exposure to corrosive gases like oxygen is crucial for many commercial applications. Typically high reliability and storage at up to 85 °C is required and the degradation of the performance of such devices with temperature during operation has to be small. Because of the sensitivity to water and oxygen encapsulation is frequently required that has to be stable under these conditions [10].

It has turned out that the thermal stability of thin organic films is not only related to technical details of the fabrication procedures, but constitutes rather fundamental challenges [28]. It is thus a prerequisite to understand and to control [29]:

- diffusion at inorganic/organic interfaces during and after growth,

- thermally induced de-wetting effects at inorganic/organic interfaces,

- structural phase transformations of the organic material at temperatures often not far from temperatures of operation,

- the vapor pressure of low-weight organics at elevated temperatures.

Moreover, interfaces of organic films are often chemically and structurally heterogeneous, and their controlled preparation is often non-trivial [28, 30]. This applies to metallic contacts [25, 31–33] and to insulating layers [34, 35] which are typically required in field-effect geometries.

In this work, the interfaces of organic films of diindenoperylene (DIP) with metals and insulators, and encapsulation strategies relevant for organic electronic devices were studied.

The main part is concerned with sputtered aluminum oxide layers as a potential dielectric and encapsulation material in organic devices. Aluminum oxide is frequently used in device and coating technology due to its specific physical and chemical properties [36, 37]. We used sputtered aluminum oxide layers to encapsulate organic semiconductor films of DIP. For the oxide film to work as a capping layer the preparation conditions have to be optimized. We therefore studied the film structure and morphology of sputtered aluminum oxide layers as a function of the preparation conditions on silicon oxide and on organic films of DIP. The understanding of the deposition and possible diffusion of inorganic materials into an underlying organic film is essential for the preparation of contacts (metals), insulators and capping layers. The aluminum oxide/DIP heterostructure was studied in detail to ensure a well-defined system. Stability at elevated temperatures is important to guarantee a good longterm performance of such devices [10, 38–44]. A major part of this thesis is therefore devoted to study the thermal stability of DIP films capped by sputtered aluminum oxide layers.

In order to ensure that the surfaces and interfaces were well-defined, we carefully studied the growth and the structure of the DIP films using several techniques before deposition of the inorganic capping layers. As a comparison to the aluminum oxide/DIP system we also investigated the deposition of gold on DIP films. From previous works on the deposition of gold on DIP [25, 26] it was clear that the diffusion of metals into the organic film strongly depends on the preparation conditions. As a comparison to aluminum oxide on DIP we studied the *in-situ* real-time deposition of gold films on

top of DIP films.

This thesis is organized as follows. Chapter 3 provides an introduction to organic semiconductors, the electrical transport in such materials and the concept of organic field-effect transistors. In Chapter 4 some general aspects of thin film growth and in more detail the specific techniques of organic molecular beam deposition (OMBD) and sputtering are described. The experimental methods for the preparation of the organic and inorganic films and the different experimental techniques used within this thesis are described in Chapter 5. Chapter 6 is devoted to the experimental results of structural investigations of organic semiconductor films of diindenoperylene (DIP), perfluorinated copper-phthalocyanine (F_{16}CuPc), and pentacene. In Chapter 7 the *in-situ* real time investigations of the deposition of gold on DIP, the characterization of sputtered aluminum oxide films deposited on silicon wafers and on DIP films are presented. The thermal stability of DIP films capped by sputtered aluminum oxide layers is discussed in Chapter 8 and Chapter 9 summarizes the results.

3 Organic semiconductors

This chapter is devoted to a brief introduction to organic molecules with semiconducting properties. The electronic properties of these molecular solids do not only depend on the structural arrangement but also on the properties of the individual molecules.

The charge transport mechanism can be separated in an intramolecular and an intermolecular transport. For organic molecules, electronic conduction is typically established by so-called π conjugated binding arrangements. The C atoms in such chains or rings are sp^2 hybridised with one p-orbital per atom left to form π-orbitals which spread over either all or a large part of the atoms participating in the connected system. The transport within the molecule is very efficient due to the conjugated electrons but occurs only over small distances. The intermolecular hopping or tunneling of the charge between adjacent molecules is slower and depends drastically on the structural organization of the material, namely the intermolecular overlap.

For the application in organic field-effect transistors (OFETs) where a film of organic semiconductors constitutes the transport layer the intermolecular overlap between adjacent molecules is crucial for the device performance.

The chapter is organized as follows. In the first part (Sec. 3.1), the organic semiconductor molecules diindenoperylene (DIP), perfluorinated copper phthalocyanine (F_{16}CuPc), pentacene and some of its relevant properties for this work will be presented. Section 3.2 is devoted to the application of such small aromatic molecules as transport layer in organic thin-film transistors. Such devices obviously expect certain requirements on the structure of the organic thin-films and its interfaces (to contacts and dielectrics). These requiremets will be discussed at the end of this chapter (Sec. 3.3).

3.1 Organic semiconductor molecules

The choice of the appropriate molecules is also coupled to the ease of purification which is crucial for the electrical properties and their thermal and chemical stability. Furthermore, the molecular structure should favor self-organization within the organic film to obtain large grains of high structural order which guarantees an optimum π-orbital overlap between adjacent molecules.

The organic semiconductor molecule diindenoperylene and some of its relevant properties will be introduced and described in detail in the following while perfluorinated copper-phthalocyanines and pentacene which are only treated marginally in this work will be presented briefly.

3.1.1 Diindenoperylene

Diindeno-[1,2,3-cd:1',2',3'-Im]perylene (DIP) is a polyaromatic hydrocarbon (PAH) with the chemical formula $C_{32}H_{16}$. The red dye is also known as *periflanthene* and was first synthesized in 1934 by von Braun [45] by the pyrolysis of fluoranthene ($C_{16}H_{10}$). DIP is a perylene-derivate with two indeno units connected to the central perylene ($C_{20}H_{10}$) core as is illustrated in Fig. 3.1.

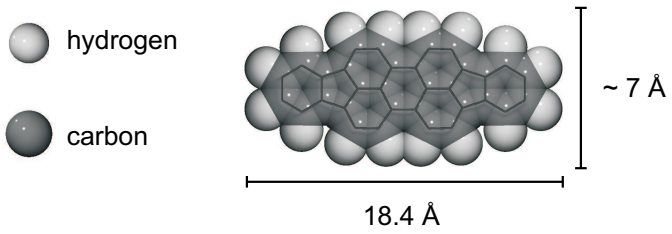

Figure 3.1: Schematic representation of the molecular structure of the diindenoperylene molecule.

It has a molecular weight of 400.48 g/mol. The dimensions of the DIP molecule were estimated on the basis of the 'Cambridge Crystallographic Database' by a combination of the crystallographic data of fluoranthene and perylene to 18.4 Å in length and 7 Å in width (with the H-atoms and their van-der-Waals radii taken into acount).

DIP has no polar groups and is only weakly soluble in most solvents. It has a high decomposition temperature with a sublimation temperature of ca. 350 °C. This relative

	Pflaum *et al.* Single crystal	Hoshino *et al.* DIP/NaCl	Hoshino *et al.* DIP/Perylene	Dürr *et al.* [51] DIP/SiO_x
	Triclinic	Monoclinic	Monoclinic	2D rectangular
a(Å)	11.59	8.67	11.0	8.55
b(Å)	12.97	6.96	10.6	7.09
c(Å)	14.88	18.55	17.5	-
α	98.11°	90.0°	90.0°	-
β	98.10°	93.5°	106.0°	-
γ	114.43°	90.0°	90.0°	90.0°
Z	4	2	2	2

Table 3.1: Several DIP crystal structures determined on single crystals and thin films. The triclinic structure has been determined in DIP single crystals by Pflaum *et al.*, with four molecules per unit cell and $P\bar{1}$ symmetry [49]. Different crystalline structures in thin films with monoclinic symmetry have been reported by Hoshino [52]. An in-plane rectangular unit cell has also been proposed [51] (Table taken from [53])

stability makes this molecules well suited for the deposition from the vapor-phase. DIP starts to carbonize below 540 °C [46].

DIP structures

For a rapid identification of organic compounds the most intense X-ray powder diffraction lines of DIP have been reported in the 1950s and 1960s by Hofer *et al.* [47, 48]. However, the bulk crystal structure of DIP has only recently been studied by Pflaum *et al.* [49] from X-ray diffraction measurements on DIP single crystals and a triclinic structure with four molecules in the unit cell of space group $P\bar{1}$ was determined (see Tab. 3.1). The density of the DIP bulk structure was $\rho = 1.354\,\mathrm{g/cm^3}$.

Compared to single crystals different structures were found for thin films of DIP. The strong influence of the molecule-substrate coupling leads to different thin film structures as is illustrated by the flat-lying DIP molecules on graphite (HOPG), Ag(111) [50] and polycrystalline gold [51] substrates compared to the almost upright-standing conformations of DIP deposited on single crystals of NaCl and perylene as reported by Hoshino *et al.* [52] (see also Tab. 3.1).

DIP films deposited on amorphous SiO_x/Si substrates displayed an exceptionally high degree of order with pronounced Laue-oscillations and narrow rocking widths which was attributed to a tendency for structural self-organization of the molecules [11, 54]. These films showed a substrate-mediated β-phase (thin-film phase) while the single-crystal α-phase (volume phase) could not be observed in these films at this low film thickness [11]. The degree of order of DIP films on silicon oxide varied according to the deposition conditions (substrate temperature, deposition rate) and films of high crystallinity were obtained at substrate temperatures of 145 °C and 12 Å/min [12]. From structural characterizations based on XRD and AFM measurements a typical lattice spacing of 16.5 Å was found [12]. Dürr *et al.* [55] also succeeded to prepare cross-sectional TEM specimens from which even the individual lattice planes of DIP could be resolved. Despite the good ordering, these DIP films showed a strong increase in roughness with increasing film thickness [56] referred to as 'rapid roughening' phenomenon.

On stepped a-plane sapphire the DIP molecules were also found in an upright-standing configuration with a lattice plane distance of around 1.6 nm [53]. Compared to the randomly oriented domains for the films on SiO_x an anisotropic in-plane orientation was found for DIP on stepped Al_2O_3 [53, 57] and for certain growth conditions Ossó *et al.* also observed the growth with screw dislocations [53].

Optical and electrical properties of DIP films

DIP in combination with Au contacts shows p-conduction and thin-film transistor (TFT) characteristics with hole mobilities in the range of $10^{-2}\,cm^2/Vs$ were measured [11]. Karl *et al.* [54, 58] could correlate the mosaicity of adjacent grains with the transport properties in a film and reported that the charge carrier mobility increased drastically with decreasing rocking width.

The electrical transport properties of TFTs based on DIP could be improved by thermal annealing procedures due to a reduction of trap density [11]. Münch *et al.* [11] also investigated the influence of ambient gases (*i.e.*, oxygen, nitrogen and water vapor) on the electrical properties of field-effect transistors with a DIP active-layer and found that the water vapor increases the charge carrier density which results in a more efficient filling of trap states and thus in a reduction of the threshold voltage.

DIP films have been investigated with respect to morphology and optical emission spectra by Heilig *et al.* [59]. Ossó *et al.* reported on a detailed comparison of the influ-

ence of DIP film structures on SiO_x and stepped Al_2O_3 substrates with their optical properties [53].

DIP in combination with other materials

DIP has also been studied in more complex *inorganic-organic* and *organic-organic* heterostructures. Dürr *et al.* [25, 31] found optimized preparation conditions for the deposition of gold contacts on crystalline thin films of DIP and they investigated the morphology and thermal stability of these systems. The diffusion of Ag into crystalline films of DIP by means of radio-tracer measurements was investigated by Scharnberg *et al.* [26]. Ossó *et al.* [53] studied the organic-organic interface of F_{16}CuPc (perfluorinated copper-phthalocyanines) and DIP as a function of the deposition order (DIP on F_{16}CuPc *vs.* F_{16}CuPc on DIP).

3.1.2 F_{16}CuPc and pentacene

Two other organic semiconducting molecules, perfluorinated copper-phthalocyanine (F_{16}CuPc) and pentacene, will be discussed briefly in the following.

F_{16}CuPc

Phthalocyanines are found in a broad variety and they are used since long as dyes in industry. The perfluorinated copper pthalocyanine (F_{16}CuPc) is a planar molecule with a central copper atom and 16 fluorine atoms substituting the hydrogen atoms of copper-phthalocyanine (CuPc : $C_{32}H_{16}N_8Cu$) as illustrated in Fig. 3.2 thus resulting in a molecular weigth of 863.9 g/mol.

The bulk structures of different phthalocyanines have been explored [60–64] and recently, Ossó *et al.* have performed X-ray powder diffraction measurements to reveal the bulk structure of perfluorinated copper-phtalocyanines [53].

In thin films of various phthalocyanines, two structural phases have been reported, a metastable α and a stable β form [65] (for F_{16}CuPc the α form was not observed). The growth of the α-form is obtained in thin films when the substrate temperature is maintained below a phase transition temperature during growth [66]. Irreversible phase transformations can be induced by a thermal treatment [67].

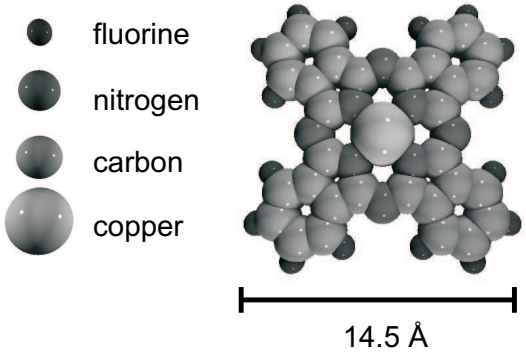

Figure 3.2: Schematic representation of the molecular structure of the $F_{16}CuPc$ molecule. $F_{16}CuPc$ consists of 32 carbon atoms, 18 fluorine atoms, 8 nitrogen atoms and one central copper atom.

The substitution of the 16 hydrogen atoms does not only influence the structure but also the electrical and optical properties – in combination with Au contacts $H_{16}CuPc$ for example is a p-type semiconductor while hexadecafluoro copper-phthalocyanine is one of the most air-stable n-type semiconductors with electron field-effect mobilities of $0.03\,cm^2/Vs$ [68]. The good electron mobilities are attributed to highly ordered films upon vacuum deposition [69].

Deposited on amorphous SiO_x substrates $F_{16}CuPc$ films show a well-defined out-of-plane stacking of the molecular lattice planes with a lattice plane separation ranging from 14.5 Å to 15.3 Å depending on the substrate temperature during deposition while in-plane randomly oriented crystallites are formed [53]. Thin films of $F_{16}CuPc$ vacuum-deposited on $Al_2O_3(11\bar{2}0)$ surfaces showed a strong in-plane anisotropy induced by the specific stepped morhology of the Al_2O_3 surface [70, 71].

Pentacene

Pentacene, $C_{22}H_{14}$, in combination with Au contacts is a p-type organic semiconductor with a molecular mass of 278.35 g/mol. It is a planar molecule [72] composed of five linearly linked benzene rings (resulting in a length of 16.1 Å [73]) as shown in Fig. 3.3(a).

In its bulk phase, pentacene has a triclinic structure (space group $P\bar{1}$) with two molecules per unit cell arranged in a herringbone configuration [75]. The density of

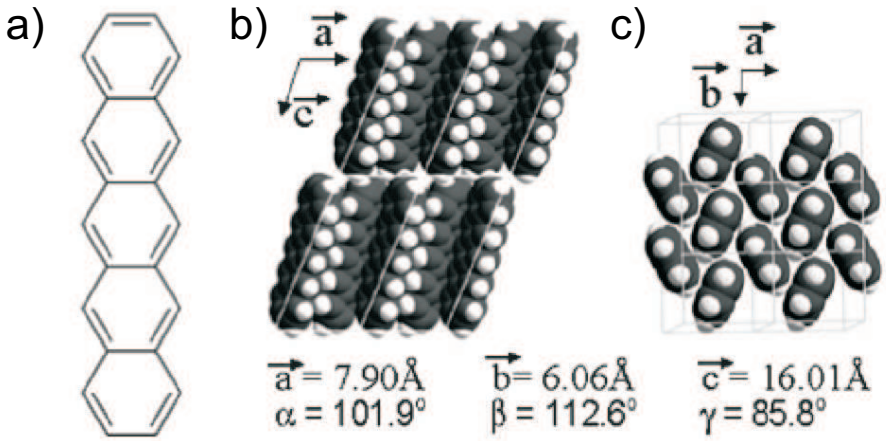

Figure 3.3: (a) Chemical structure and (b-c) bulk crystalline structure of pentacene (from Ref. [74]).

pentacene is 1.32 g/cm^3. Two polymorphs of the pentacene bulk structure are reported [76,77]. For thin pentacene films vacuum-deposited on SiO_x two crystallographic phases were found, one phase (α-phase) is characterized by an interlayer distance d_0 of 15.5 Å and is referred to as 'thin film phase' [78] while the other phase (β-phase) with a layer separation of 14.5 Å is only found beyond a critical film thickness [79] and dominates for thicker films. It corresponds to the bulk polymorph shown in Fig. 3.3(b-c).

For pentacene films relatively high hole mobilities up to ca. 0.6 cm^2/Vs are reported [80–83] which can be attributed to the high degree of crystallinity of the evaporated thin films.

3.2 Organic field-effect transistors (OFET)

Organic semiconductors are known since the late 1906 [1–3]. However, the first field-effect in such materials was only reported in 1970 [84–86] and the first field-effect transistors based on organic semiconductors was described in 1986 for conducting polymers [87] and in 1989 for small conjugated molecules [88]. Since then, tremendous progress was achieved in purifying organic semiconductors and some organic field-effect transistors (OFET) now compete with amorphous silicon FETs.

Due to their low charge carrier mobilities field-effect transistors based on organic

molecules adopt the architecture of the thin film transistor (TFT) [89] which has proven its adaptability with low conductivity materials such as amorphous silicon.

Beside its relevance for industrial applications, OFETs also present a powerful tool for the determination of fundamental transport properties (*i.e.*, charge carrier mobility, μ) in organic assemblies which can help to understand the transport mechanisms in such materials.

In this section, the principle of operation of organic field-effect transistors and some of its relevant characteristics are briefly described. From a precise analysis of the TFT characteristics information on the relationship between structure and charge transport can be obtained.

3.2.1 Basic concept of the organic field-effect transistor

Organic field-effect transistors are realized in several geometries but their basic concept remains the same [5, 90, 91]. Two electrodes (source and drain) are in contact with the semiconducting film at a typical distance of some hundred nanometers while a third electrode (gate) is separated from the semiconducting film by an insulating layer as illustrated in Fig. 3.4(a).

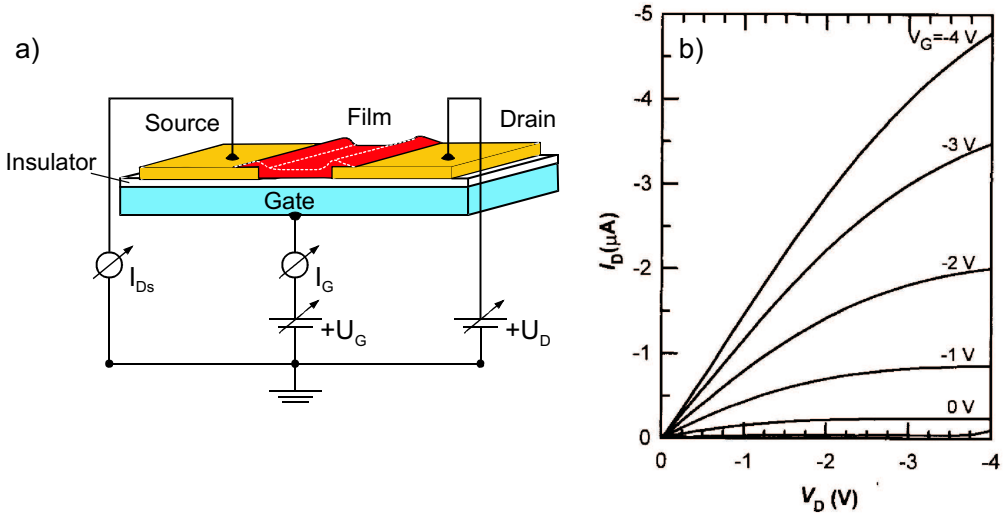

Figure 3.4: (a) Schematic representation of an OFET. (b) OFET characteristics of pentacene based TFT on polycarbonate substrate (from Ref. [92]).

When a voltage is applied between the source and gate electrodes (V_G), charge carriers

are capacitively induced at the insulator-semiconductor interface forming a conducting channel. In first order the number of induced charge carriers is proportional to the gate voltage V_G and the capacitance C of the dielectric film. Thus, the drain current, I_D, that flows between source and drain when applying a source-drain voltage, V_D, depends strongly on the gate bias, V_G.

Under certain assumptions (the electric charge density related to a variation of the electric field along the channel is much smaller than that related to a variation across the channel, and the charge carrier mobility is constant) [93–95], which are not always fulfilled, the drain current can be described by the basic equations from conventional semiconducting devices [96]. For $V_G - V_T \gg V_D$ the charge carrier concentration is nearly uniform along the conducting channel and Eq. 3.1 yields the standard *linear regime* equation,

$$I_D = \frac{W}{L} C\mu \Big[(V_G - V_T)V_D - \frac{V_D^2}{2} \Big] , \tag{3.1}$$

where, μ is the charge carrier mobility, W is the channel width, L is the channel length, and V_T is the threshold voltage which takes into account the field-free carrier concentration as well as details of the internal charge distribution and trapping at the interface and at the contacts.

At $V_G - V_T \sim V_D$ the region near the drain contact is completely depleted of free charge carriers and the drain current becomes independent of V_D. The *saturation regime* can be described by

$$I_{D,sat} = \frac{W}{2L} C\mu_{sat} (V_G - V_T)^2 . \tag{3.2}$$

3.2.2 TFT characteristics

Some of the important parameters which can be extracted from current-voltage characteristics of OFETs (as shown in Fig. 3.4(b)) are the field-effect mobility, μ, the threshold voltage, V_T, and the I_{on}/I_{off} ratio and the subthreshold rise.

In the linear regime, the field-effect mobility can either be determined from the so-called transconductance, g_m, or from the conductance, g_d, given by,

$$g_m = \frac{\partial I_D}{\partial V_G}\Big|_{V_D} = \frac{W}{L} C\mu V_D \quad , \tag{3.3}$$

$$g_d = \frac{\partial I_D}{\partial V_D}\Big|_{V_G} \sim \frac{W}{L} C\mu (V_G - V_T) . \tag{3.4}$$

According to Eq. 3.2, the field-effect mobility, μ, can also be determined from the saturation regime.

The on/off current ratio, I_{on}/I_{off}, is another important characteristic of TFTs and is typically reported as 10^x. It depends on the ratio between field-effect mobility and conductivity of the semiconductor, μ/σ. A high I_{on}/I_{off} ratio thus generally requires a large mobility and a low conductivity value. The low mobility of these materials will lead to low frequency electronics since the frequency is proportional to the charge carrier mobility ($f \propto \mu/L^2$, L: length of the transport channel). However, in terms of current ratio (I_{on}/I_{off}), field-effect mobility (μ_{FET}), and threshold voltage (V_T), the performance of the best organic TFTs now rivals that of commercial amorphous silicon TFTs.

3.2.3 Thickness of the conducting channel

Horowitz *et al.* [5] have determined the thickness of the conducting channel by calculating the charge carrier distribution across the semiconductor film and they received for typical values a thickness of ca. 1.8 nm which for the case of DIP ($d_{DIP} = 1.65$ nm) would mean that practically all the charge is concentrated in the first monolayer.

Experimental evidence for such a behavior was found by Muck *et al.* [97] when performing *in-situ* electrical characterization of DH4T field-effect transistors.

3.3 Correlation between thin film structure and electrical properties

One of the key parameters, controlling the charge transport in conjugated materials, represents the structural organization of such films. High charge carrier mobilities are achieved for a strong overlap of the π-orbitals of adjacent molecules which depends on the intermolecular bonding, the size of the molecules, the molecular symmetry, and, on the symmetry of the crystal packing [91]. In this sense, organic single-crystals represent a bench mark in terms of intrinsic mobilities [98–100]. However, due to their expensive production costs and their limited size OFETs based on single-crystals are not well suited for low-cost and large-area electronics.

At this point, the intrinsic and effective mobilities have to be distinguished. Only the

effective mobility (as found in thin films) can be improved by better structural organization of the molecules as for example by functionalization of the substrate surface. The intrinsic mobilities in organic single crystals are for example measured by time-of-flight (TOF) [54] measurements.

Thin oligomer (small aromatic molecules) films evaporated under UHV conditions have shown the potential to fulfill the structural requirements mentioned above [7, 28, 101, 102] and OFETs based on such films have shown good charge carrier mobilities [7, 103]. The fact that small aromatic molecules quite often have a two-dimensional anisotropic shape, and therefore the van-der-Waals interaction strongly varies with direction, introduces an additional degree of freedom in film growth and polymorphisms are frequently encountered in such materials [7, 104].

For the application in OFETs it is highly desirable that the aromatic molecules form a continuous ordered film with the preferred transport directions in the grains oriented parallel to the conducting channel (upright-standing molecules on the dielectric layer) [91]. The grain size and grain boundaries in these polycrystalline films have been shown to influence the charge carrier mobility [58, 105, 106]. Horowitz *et al.* [107] have shown that the carrier mobility increases with grain size. Therefore, from an idealized point of view (as the growth on contacts will be different than for SiO_x) the highest mobility is expected when the individual grain size exceeds the channel length.

The grain sizes (and the number of grain-boundaries) in a film depends on the nucleation density which can be influenced by the film growth process [7, 108]. A further possibility to increase the grain size and thus the effective mobility is the functionalization of the substrate [109] which influences the interaction between substrate and molecules. The use of stepped Al_2O_3 substrates [70, 71] and vicinal Cu(111) surfaces [110] has shown a step-induced lateral order with increased grain sizes.

Besides the influence of the π-orbital overlap between adjacent molecules, traps originating from impurities, grain boundaries and defects at the interfaces also influence the device performance [101]. Charges trapped in deep levels, *i.e.* $E_t > kT$, do not contribute to the charge transport and their coulombic charge influences the electric field distribution in a device [111]. Chemical impurities in an organic semiconductor film can also function as dopants and thus compromise the electrical properties such as the I_{on}/I_{off} ratio and the threshold voltage [91]. Especially, as the organic semiconductors are wide band-gap materials, the purity and the purification of the organic materials

therefore is a crucial aspect [6, 54].

The understanding of the initial growth of the first few monolayers in an organic film is crucial not only for the structure of the thicker film but also for the electrical transport in OFETs. It has been shown that the charge carrier distribution in OFETs is mainly restricted to the first few molecular layers [97, 112–114].

4 Thin film growth

The properties of thin films may differ strongly from their bulk material properties due to the interaction with the substrate and the resulting structural constraints. The choice of the right deposition technique depends on the material and on the desired film properties. The deposition method and conditions influence the film characteristics and therefore also the field of application. In this chapter, some general aspects of thin film growth will be discussed for the specific techniques of molecular beam epitaxy (MBE) and sputtering. More precisely, the deposition of organic molecules by organic molecular beam deposition (OMBD) and the sputtering of aluminum oxide layers will be presented.

The present chapter is organized as follows. After discussing some fundamentals of film growth in Sec. 4.1, the MBE and OMBD techniques will be presented in Sec. 4.2. MBE is a widely used technique for the preparation of epitaxial thin films of high structural order and its adaptation to the use of small conjugated molecules yields new aspects in film growth. Section 4.3 is devoted to the sputtering technique and the structure and properties of the resulting films. In the present work, aluminum oxide films were used as capping layers for the encapsulation of organic films. The influence of the sputter conditions on the film properties of aluminum oxide will be discussed in Sec. 4.4.

4.1 Fundamentals of film growth

4.1.1 Thermodynamical aspects of film growth

The formation of a thin film involves the processes of nucleation and growth [115, 116]. In a rather simplistic view, thermally evaporated atoms condense on a substrate and undergo several atomistic processes such as adsorption, surface diffusion, (re-)desorption and nucleation when they agglomerate with other atoms, see Fig. 4.1. If such an atom

adsorbs on a surface, it has an adsorption energy, E_a, and the lifetime before desorption is given by $\tau_a = \nu_a^{-1} \exp(E_a/kT)$, where the pre-exponential frequency ν_a may vary relatively slowly with T [115]. On the surface the adatom may diffuse in a random walk with a diffusion coefficient given by $D = (\nu_d a^2/4) \exp(-E_d/kT)$. From BCF (Burton, Cabrera & Frank [117]) the characteristic diffusion length can be determined to $x_s = (D\tau_a)^{1/2}$.

The formation of clusters generally starts at energetically favorable sites such as steps, defects, etc. The clusters are mobile and incorporate further impinging atoms and smaller clusters thus growing in size. These clusters are still able to decay but above a critical size they are stable and continuously grow.

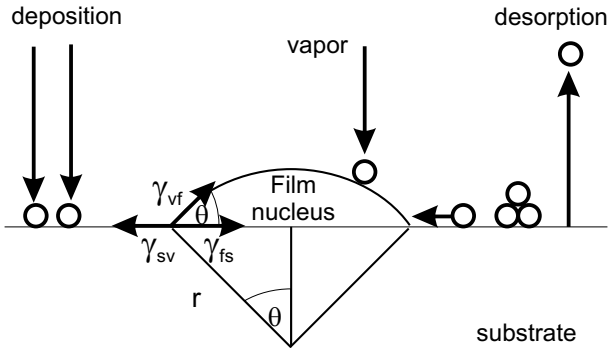

Figure 4.1: Schematic of basic atomistic processes on a substrate surface during vapor deposition (after [118]).

The density of these nuclei saturates quickly and the clusters grow until they merge by a coalescence process. For homoepitaxial systems the substrate will be covered by a network of unfilled channels which are filled until the film is continuous [119].

For heteroepitaxial systems, 'A on B', additional parameters such as the surface free energy, γ, and the stress relaxation energy induced by the lattice mismatch between adsorbate and substrate have to be considered. The resulting energy difference between both contributions can be expressed as [120],

$$\Delta E = \Delta E_{surf} + \Delta E_{relax} = c\gamma r^2 - c' k \xi r^3 \quad , \tag{4.1}$$

where, r is the mean dimension of an aggregate, k is the bulk modulus, and ξ is the strain. Fig. 4.2 illustrates the energy difference between island growth and layer growth.

From a critical value, r_{crit}, island growth is energetically more favorable (but depends on temperature).

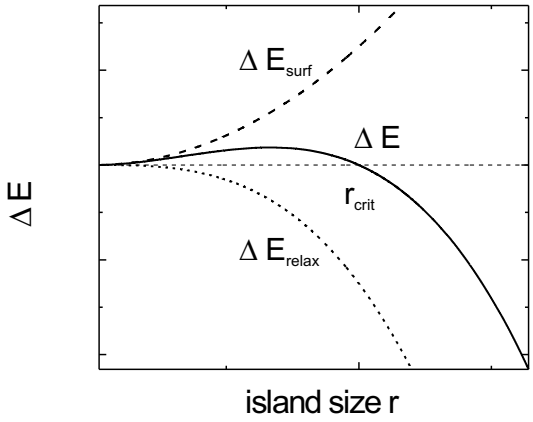

Figure 4.2: Energy contributions as a function of the island size (after [120]).

Considering Fig. 4.1 there are several surface and interface tensions, γ_{sv}, γ_{fs} and, γ_{vf}, corresponding to substrate-vapor, film-substrate and, vapor-film interfacial tensions, respectively. The contact angle θ depends on the surface properties of the involved materials and the mechanical equilibrium among the interfacial tensions yields Young's equation,

$$\gamma_{sv} = \gamma_{fs} + \gamma_{vf} \cos\theta + CkT \ln\left(\frac{p_0}{p}\right). \tag{4.2}$$

The third term on the right side accounts for the equilibrium condition of the whole system including the gas phase above the deposited film [121]. The ratio p/p_0 is called the degree of supersaturation and C is a constant.

4.1.2 Film growth modes

Based on Young's equation (Eq. 4.2) and the stress relaxation energy different growth modes can be distinguished [118, 120]. The three basic growth modes are illustrated in Fig. 4.3.

Fig. 4.3(a) represents island, or Volmer-Weber growth for which $\theta > 0$, and therefore $\gamma_{sv} < \gamma_{fs} + \gamma_{vf}$. In this case, the interatomic (intermolecular) interactions are stronger

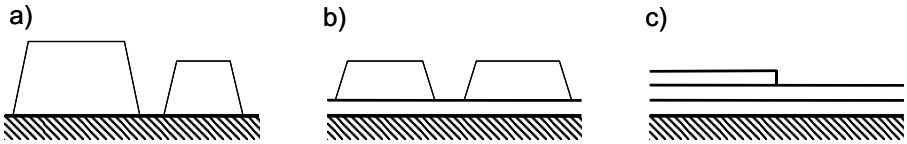

Figure 4.3: Schematic representation of the three growth modes: (a) island, or Volmer-Weber growth; (b) layer-plus-island, or Stranski-Krastankov growth; (c) layer-by-layer, or Frank-van der Merwe growth (after [115]).

then the bonding of the atoms (molecules) to the substrate which leads to clusters growing in three dimensions to form islands.

The opposite happens during layer-by-layer, or Frank-van der Merwe growth (Fig. 4.3(c)). The atoms (molecules) are more strongly bound to the substrate than to each other and the deposit 'wets' the substrate ($\theta = 0$), $\gamma_{sv} = \gamma_{fs} + \gamma_{vf}$ [116,120]. If the decrease in bonding energy is continuous towards the bulk crystal value, the layer growth mode is sustained.

The layer-plus-island, or Stranski-Krastanov growth mechanism (Fig. 4.3(b), $\gamma_{sv} > \gamma_{fs} + \gamma_{vf}$) is an intermediate combination of the layer and island growth. After the formation of one or more monolayers, the strain energy is large with respect to γ_{vf}, and subsequent layer growth becomes energetically unfavorable and islands form.

4.2 Molecular beam epitaxy

For many applications the incorporation of foreign atoms or molecules into a growing film is undesirable. To avoid the incorporation of residual gases into the growing film ultra-high vacuum pressures (UHV, better than 10^{-9} mbar) may be necessary. The molecular beam epitaxy (MBE) [122–124] has proven to supply epitaxially grown films of high purity.

MBE is based on the thermal evaporation of the source material typically in UHV conditions. The compound is thereby evaporated from a special oven in a more or less directed beam which guarantees a uniform thickness of the deposit. By controlling the sublimation temperature very low deposition rates can be obtained. The high purity along with the low deposition rates allow for the growth of films with good crystallinity. The use of the MBE technique together with *in-situ* film diagnostic methods during

and immediately after growth have provided many new insights into growth processes.

The MBE method in combination with the evaporation of organic molecules is assigned as organic molecular beam epitaxy (OMBE) [101,125] or organic molecular beam deposition (OMBD), depending whether a well-defined relationship between the position of the deposited molecules and substrate atoms exists or not.

The MBE technique can easily be adapted to the use of small conjugated molecules. However, there are some issues specific to organic thin film growth which do not apply for the deposition of inorganic materials [28]. Organic molecules have an extended shape and their internal degrees of freedom introduce a spatial anisotropy into film growth. The orientation of a molecule during deposition leads to the distinction between 'lying-down' and 'standing-up' films and transitions between both orientations during the film growth are possible. Due to their size, the unit cells of organic molecules are greater than those of typical (inorganic) substrates. Furthermore, the interaction between molecule-molecule and molecule-substrate is much weaker than for inorganic systems and can usually be described by a van-der-Waals interaction.

4.3 Sputter deposition

In contrast to the MBE technique where the deposits are thermally evaporated, the sputtering technique is based on dislodging atoms from a target by the impact of gaseous ions. The basic sputtering processes can be divided into four categories: (1) direct current (d.c.), (2) radio frequency (r.f.), (3) magnetron and (4) reactive sputtering. Furthermore, there are important variants within and some hybrids between these categories (*e.g.*, reactive r.f., r.f. magnetron) which are well established. Here, only a brief description of the principle of sputtering and the basic technique of r.f. magnetron sputtering which was used within this work is given.

4.3.1 Basic principle of sputtering

The individual sputtering techniques show a similar mode of operation but the basic principle of sputtering can be explained best for d.c. sputtering, which is schematically shown in Fig. 4.4(a). A more detailed description of the individual sputtering techniques can be found in Refs. [118, 120, 126, 127].

The sputtering apparatus is situated in a vacuum chamber with two electrodes facing each other at a potential difference of typically several kilovolts. The target consists of the material to be deposited or from which a film is synthesized (reactive sputtering) and since it is connected to a negative potential of a d.c. power supply it is referred to as the cathode while the substrate for the film is connected to the anode.

When a sputtering gas, typically argon, is introduced into the evacuated chamber a plasma discharge can be initiated for typical pressures of 10^{-1}–10^{-3} mbar. Electrons ejected from the cathode are accelerated on their way to the anode and undergo several collisions with the sputtering gas. If their kinetic energy is high enough they produce secondary electrons and positively charged ions, the latter being accelerated towards the target to sputter off the deposits. After passing the discharge region the deposits arrive on the substrate mostly as neutral atoms. Eventually, when sufficient electrons are generated to produce vice versa sufficient ions to regenerate the same number of initial electrons, the discharge becomes self-sustaining.

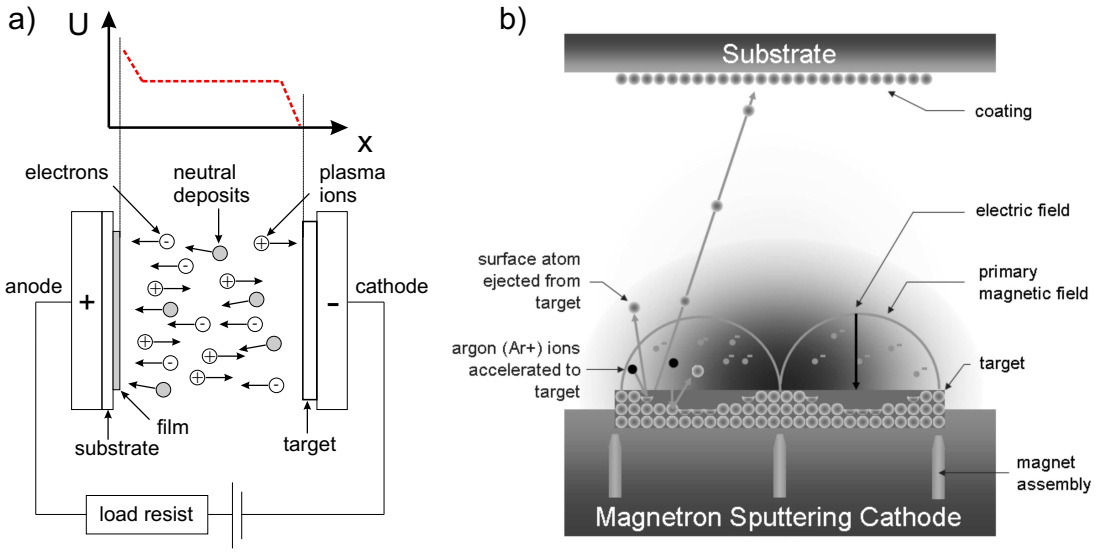

Figure 4.4: Schematic of (a) d.c. (after [120]) and (b) magnetron sputtering.

In Fig. 4.4(a) the dashed line indicates the potential distribution between the electrodes. As the plasma is a good conductor and due to the different mobilities of ions and electrons the main potential drop is observed in the darkspace at the cathode. Within this dark space the positive sputtering gas ions are accelerated towards the cathode.

4.3.2 R.f. magnetron sputtering

The r.f. sputtering technique (see Fig. 4.4(b)) was invented to avoid the accumulation of electrical charges when sputtering from an insulating target. Here, a high-frequency voltage of typically 13.6 MHz is capacitively coupled to the target. The r.f. sputtering essentially works because the target self-biases to a negative potential. This is a consequence of the fact that electrons are much faster than ions and have little difficulty in following the periodic change in the electric field. But for a symmetric arrangement of cathode and anode the alternating electrical field should produce sputtering from both electrodes. Thus, for sputtering from only one electrode, the sputter target must be an insulator and be capacitively coupled to the r.f. generator while the other electrode (substrate stage and system ground) is directly coupled to the r.f. generator. Furthermore, the area of the target electrode should be small compared with the total area of the other electrode.

To improve the deposition rates magnetic fields can be used which force the electron onto helical paths close to the cathode. This prolongs the electron residence time in the plasma and thus enhances the probability of ion collisions. In this so-called magnetron arrangement the magnetic fields reduce the electron bombardment of the substrates and it allows a lower gas pressure.

4.3.3 Film structure and morphology of sputtered films

The structure of films grown from the vapor phase depends strongly on four basic processes: shadowing, surface diffusion, bulk diffusion, and desorption. While the last three processes depend on the bounding energy of the deposited material, shadowing is a simple geometric interaction between the roughness of the growing surface and the angular directions of the arriving atoms. Depending on the dominating process at different substrate temperatures T_s different structures can evolve. Several zone structure models have been introduced to characterize the film structure as a function of the substrate temperature [128–130].

For the sputtering technique, the partial pressure of the sputtering gas has an important impact on the kinetic energy of the impinging deposits and thus also on the film structure. Thornton developed a zone scheme with four zones (1, T, 2, 3) characterizing the structural morphologies of sputtered films as a function of the normalized temper-

ature (T_s/T_m) and the partial pressure of the sputtering gas [130], shown in Fig. 4.5.

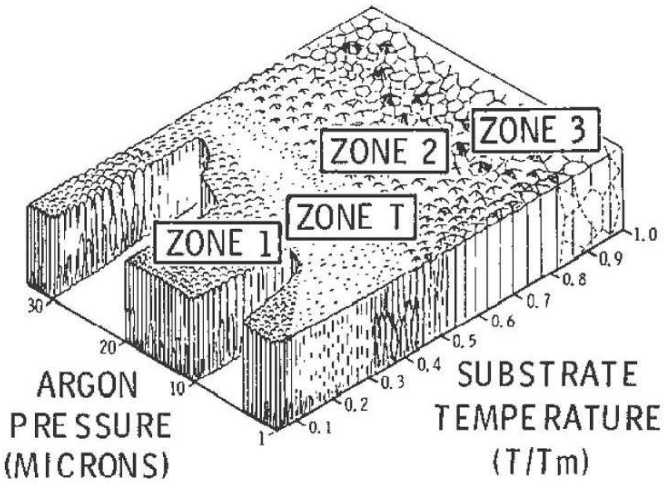

Figure 4.5: Thornton zone model (after [130]) illustrating the dependence of evaporated film morphologies on the sputter gas pressure and on T_S/T_M (T_S: substrate temperature, T_M: melting point of substrate material).

In zone 1 structures ($T_s < 0.2\ T_m$), the adatom surface diffusion is only very limited and shadowing effects dominate. It can occur in amorphous as well as crystalline films. Zone T ($0.2-0.3\ T_m$) is a transition state where adatom diffusion largely overcomes the roughness of the substrate and the initial nucleation, such that crystals of energetically unfavorable orientations are eliminated. In zone 2 and 3 ($T_s > 0.5\ T_m$) the resulting structures are due to surface diffusion controlled growth and bulk diffusion controlled growth, respectively.

Although the zone schemes mentioned above have been developed for evaporated and sputtered metal films, they have also proven their adaptability to metal oxide films [131].

4.4 Sputter deposited aluminum oxide films

Aluminum oxide is frequently used in different fields of application due to its extraordinary properties, its low cost and its relative abundance. The possible high grade of purity makes aluminum oxide also interesting for fundamental research. Among other

properties aluminum oxide excels on its good thermal stability, its large dielectric constant, its mechanical strength, its transparency and its good gas barrier properties.

For many industrial applications high deposition rates, good homogeneity, low surface roughness and good control of the film thickness are important. Depending on the application and environment different properties of the thin films are required. An important class for the deposition of aluminum oxide films are the diverse sputter techniques which were presented in Sec. 4.3. The properties of sputtered aluminum oxide films are strongly dependent on the process parameters and great efforts have been undertaken to improve existing deposition methods [132–136] and to invent new techniques. Sputter-deposited aluminum oxide films have been extensively studied for various applications ranging from microelectronic and optical applications to wear-resistant coatings. In the following, some properties of aluminum oxide films and their dependence on the deposition parameters will be summarized.

4.4.1 Influence of the sputtering parameters on the film properties

Due to the complexity of the sputtering process it is difficult to estimate the dominating influence of a certain sputtering parameter on the film structure and composition. Furthermore, the film properties do not depend linearly on the sputter conditions which makes it difficult to predict the resulting film structure and composition. The interplay between the influences from different sputtering parameters determines the film structure, composition, and therefore its mechanical, electrical and optical properties. In many studies the dependencies of the film properties on different sputtering parameters were investigated [136–144] and it is possible to point out some general dependencies.

In the frame of this work, the working temperature of aluminum oxide did not exceed 400–500 °C. However, a good thermal stability of the films is required at these temperatures. Aluminum oxide has a multitude of polymorphs (see Appendix A for details) with various routes of phase transformations. However, in this temperature range, amorphous aluminum oxide films are expected to be stable against phase transformations [137].

The gas pressure and the sputtering power have an influence on the kinetic energy of the condensing species such as target atoms, argon atoms, and impurity atoms. The bombardment of the film by these energetic species is called 'atom peening' [145–147] and its magnitude increases with increasing sputtering power and with decreasing plasma pressure due to the increased mean free path of the particles. Consequently,

the film structure changes gradually from compact to porous as the sputtering pressure is increased and the sputtering power is reduced [148]. However, due to their high kinetic energy at low deposition pressures, gas atoms can be entrapped in the growing film [137, 139, 148–150]. The content of entrapped argon atoms in a film can also be affected by the substrate temperature such that for higher substrate temperatures the argon content is lower. This effect can be explained by the decrease in sticking probability of inert sputter gas with increasing temperature [137]. The different sputtering parameters can also influence the stoichiometry (Al/O ratio) of the aluminum oxide film. It was observed that for low sputtering power the oxide films become more rich in oxygen with increasing pressure while for high r.f. power the stoichiometric composition (Al/O = 0.67) was obtained independently from the pressure [148]. The substrate temperature can also significantly change the sticking coefficients of the species and the reactivity behavior [137], therefore, with increasing substrate temperature the stoichiometry (Al/O) decreases.

4.4.2 Influence of the film properties on the mechanical, electrical and optical properties

Obviously, the sputtering parameters also influence the mechanical, electrical and optical properties, accordingly. For sputtering in an argon atmosphere the color of aluminum oxide films was observed to change from brownish to yellowish with decreasing stoichiometry (tuned by the substrate temperature) [137].

The stoichiometry of an aluminum oxide film also influences its electrical properties such as the electrical breakdown field. Oxygen-rich films were found to have higher breakdown fields than metal-rich films [139]. This could be explained by the fact that until there is sufficient excess of oxygen in the film, the present aluminum rich defects act as 'randomly distributed weak spots' which provide the mechanism for the breakdown [139].

The mechanical properties of a film are closely related to the residual stresses in the film. Films deposited via sputtering are always found in a state of compressive stress. The stress dependence on pressure and sputtering power is caused by the incorporation of argon and by the 'atom peening' process [146,147,151]. Here, the forward momentum of the bombarding particles is transferred to the lattice which results in densification and the generation of compressive stresses below the surface. Molecular dynamics sim-

ulations of sputter-deposited thin films have recently shown to support a mechanism in which the tight packing of film atoms around injected gas atoms leads to a high compressive stress [152]. Aluminum oxide films become more brittle with decreasing pressure and increasing sputtering power [148]. The evolution of the hardness values may be explained by several of the following factors: microstructural changes, stress evolution, and atom bombardment. In fact, all these phenomena are closely linked but their interdependence and individual contributions in the variation of hardness are difficult to specify.

5 Experimental methods

In the present chapter we focus on the experimental methods for the preparation of organic and inorganic films as well as on the techniques employed to characterize and measure the film properties.

The aim is to prepare organic films and inorganic-on-organic hybrid systems and to study their structural properties as well as their thermal stabiliy. The different materials such as organic molecules, gold and aluminum oxide obviously afford different deposition techniques and especially for the inorganic-on-organic heterostructures the deposition technique for the inorganic material has to be compatible with the (stability) requirements of the underlying organic film.

The organic films were prepared by organic molecular beam deposition (OMBD) in an ultra-high vacuum (UHV) system, gold films were deposited by vacuum-evaporation and aluminum oxide films were deposited by r.f. magnetron sputtering.

The most intensively used experimental techniques to access structural informations on the samples were X-ray diffraction (XRD) and atomic force microscopy (AFM). While AFM measurements only probe the surface of the samples XRD techniques are particularly powerful for investigations of the structure of buried interfaces. Furthermore, complementary techniques such as cross-sectional transmission electron microscopy (TEM), Rutherford backscattering spectroscopy (RBS) and optical microscopy, will be briefly addressed.

5.1 Thin film preparation

In this section, the different techniques for the deposition of organic semiconductor molecules, gold and aluminum oxide are described. Some aspects such as the chemical purity of the source material and the uniformity of the thin-film thickness can be of paramount importance for some applications and thus have to be considered in the film

preparation.

5.1.1 Substrates

The influence of the substrate material on the film formation has been discussed in Chapter 4. Besides the proper choice of the substrate the appropriate cleaning procedures of the latter also has to be considered. The aim is to clean the sample surface such that the film growth and characterization methods are not influenced by the contaminations on the substrate surface.

In the framework of this thesis mostly Si(100)-wafers with a native oxide layer (of 10−20 Å thickness) were used as a substrate. Occasionally also silicon wafers with (111) orientation and/or a thermally oxidized silicon oxide layer of $\sim$ 4000 Å thickness were used. The Si-wafers had a thickness of 356−406 μm and a specific resistivity of 0.005 to 0.02 Ohm/cm. Silicon wafers were cleaned in several cycles in an ultrasonic bath filled first with acetone and then with ethanol. Ethanol was always the last solvent and the wafer then was purged in a nitrogen gas stream. Afterwards the substrates were quickly attached to tantalum or steel sample holders and transferred into the UHV chamber where they were outgased for ca. 12 h at 700 °C.

5.1.2 Organic film preparation

The organic semiconductor molecules used within this thesis were already presented in Sec. 3.1. The DIP molecules were purchased from the Institut für PAH-Forschung (in Greifenberg, Germany) and pentacene and F_{16}CuPc were purchased from Aldrich. The materials were purified by means of gradient sublimation in the group of Dr. Jens Pflaum at the University of Stuttgart.

In this section, the preparation of organic thin films is discussed. Due to their good thermal stability DIP, pentacene and F_{16}CuPc films were prepared by the organic molecular beam desposition (OMBD) technique in a UHV system which allows for high-purity films with a minimum of residual gas atoms incorporated in the organic film.

Evaporation of organic molecules

The OMBD technique is based on the evaporation of the source material under UHV conditions. To achieve an efficient deposition of the evaporant with a uniform thickness

of the deposit, special evaporation cells have been developed which deliver a somewhat directed beam.

In a so-called Knudsen cell, as is shown in Fig. 5.1, the organic molecules are sublimated from a ceramic crucible with a small opening. The temperature of the evaporant can be controlled to obtain the desired vapor pressure [115, 153]. We used home-built Knudsen cells after a design of K. Ritley. The support materials (molybdenum, ceramics, tungsten, tantalum ...) of the evaporation cell were chosen in such a way as they had negligible vapor and dissociation pressures at the operating temperatures (up to $\approx 400\,^{\circ}\mathrm{C}$) to avoid contamination of the deposit. The width of the organic molecular beam emitted from this cell was sufficiently broad to guarantee for a homogeneous film thickness on a substrate with a lateral length scale of 1 cm. The substrate was positioned in such a way that the surface was normal to the direction of the molecular beam.

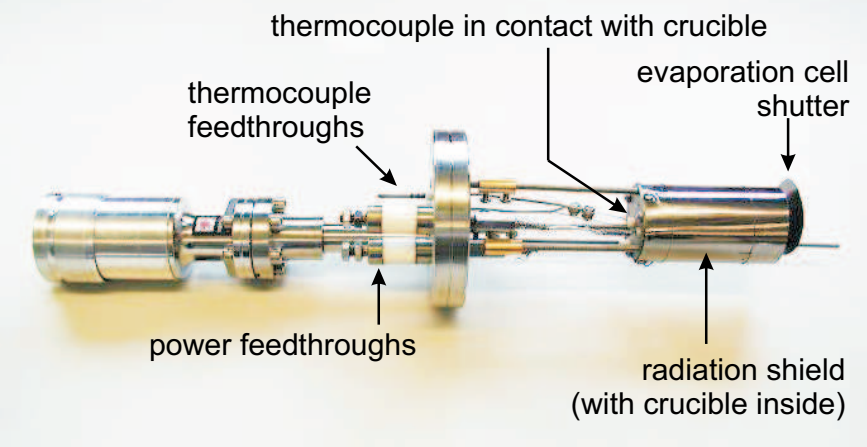

Figure 5.1: Photograph of a home-built Knudsen cell for the evaporation of organic molecules.

Resistance-heated tungsten wires wound around a ceramic cylinder served as a heater and the evaporation temperature (as measured by thermoelement couples mounted close to the crucible) was controlled by temperature controller (*Eurotherm 2408*) with an absolute precision of $\Delta T \leq 1\,^{\circ}\mathrm{C}$.

The deposition could be started (finished) by opening (closing) the evaporation cell shutter and the deposition rate could be determined from a quartz crystal microbalance which has been calibrated before. The substrate temperature during deposition could be varied from -160 °C up to 700 °C (see below, Sec. 5.1.2).

OMBD-System

The UHV system for the deposition of organic semiconductor molecules is displayed in Fig. 5.2. It is a commercial Omicron UHV system which consists of three units con-

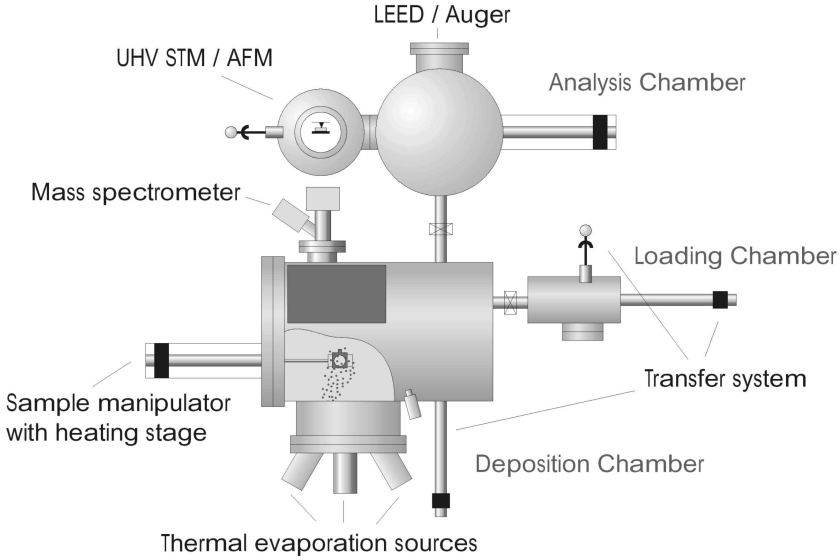

Figure 5.2: UHV system for the deposition of organic semiconductor molecules via organic molecular beam deposition (OMBD) from Knudsen evaporation cells. The system consists of a preparation chamber, an analysis chamber and a load lock system for sample transfer to the outside (from Ref. [154]).

nected via a transfer system. The sample loadlock allows the fast introduction and extraction of samples and it is connected to the deposition chamber. The latter is equipped with several Knudsen cells for the evaporation of organic semiconductors and gold, it has a quartz crystal microbalance (QCM) for the determination of the deposition rates and film thicknesses and a quadrupole mass spectrometer. Its manipulator is equipped with a heater and samples can also be cooled by a liquid nitrogen cooling system. The deposition chamber is connected to the analysis chamber which allows *in-situ* surface analytical measurements such as scanning probe microscopy (combined AFM/STM Omicron system), low energy electron diffraction (LEED) and Auger electron spectroscopy (AES). Additionally, the chamber is staffed with a sputter gun.

The UHV system is equipped with a turbo-molecular pump and the deposition cham-

ber and the analysis chamber are both equipped with an ion-pump and a titanium sublimation pump. Therefore, pressures in the range of $10^{-11}-10^{-10}$ mbar are routinely obtained.

5.1.3 Preparation of organic films and gold films in a portable UHV chamber

For *in-situ* real-time growth experiments with X-ray diffraction methods a transportable UHV chamber as schematically displayed in Fig. 5.3(a) was used.

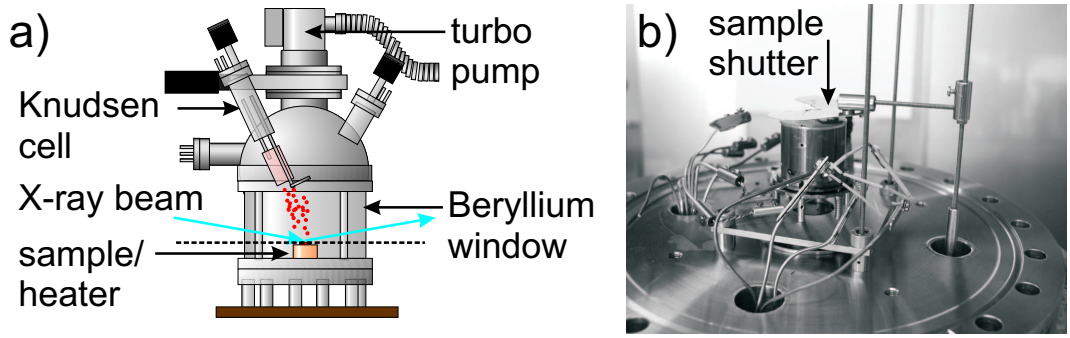

Figure 5.3: (a) Portable UHV chamber for *in-situ* real-time growth experiments. It is equipped with a beryllium window, a QCM and diverse evaporation sources for organic molecules and gold. (b) A shutter has been mounted for the protection of the sample on the heater.

The portable chamber is equipped with a 'X-ray transparent' beryllium window (of 1 mm thickness) and could be mounted on common diffractometer tables. For the evaporation of organic molecules a Knudsen cell is mounted in a top-down configuration and the deposition rate can be monitored by a QCM thermally decoupled but mounted close to a heater stage which can also be cooled with liquid nitrogen. The system is pumped with a turbo-molecular pump and an ion-pump.

A rotatable shutter was developed (see Fig. 5.3(b)) to protect the substrate on the heater while calibrating the deposition rate of the evaporation cells. This shutter also allows to mount two samples on the heater and to expose one of the samples to the molecular beam while the other sample remains protected by the shutter.

The top-down geometry represents also a challenge for usual gold evaporation cells. We therefore used a commercial mini e-beam evaporator (EGCO4 from Oxford Applied

Research[1]) which was designed for use in UHV environment and which is capable to evaporate high melting-point metals, see Fig. 5.4.

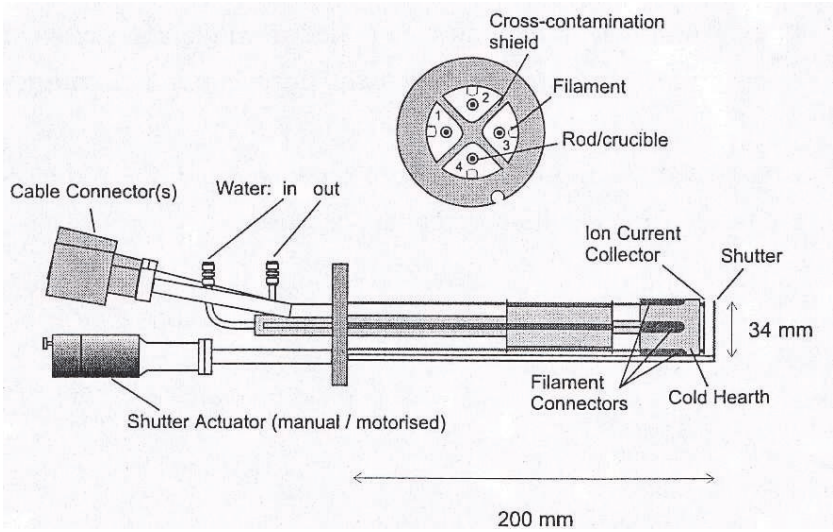

Figure 5.4: E-beam evaporator designed for high melting-point materials. Target rods can be loaded in four pockets (Drawing from EGCO4 manual).

For this e-beam evaporator the target material can be used in the form of rods and the evaporation is achieved by electron-beam induced heating of the rod. The target rod is held at a high potential, up to 2 kV, and the electrons thermally emitted from the dedicated filament (on ground potential) are accelerated in the electric field onto the tip of the rod. This electron beam induces thermal evaporation of the target material. The total available power can be as high as 200 W which is sufficient to evaporate tungsten. This e-beam evaporator has four pockets which can be loaded with different rods and once the desired evaporation rate is reached the emission current is controlled externally by a feedback loop.

5.1.4 Preparation of aluminum oxide films

Among the deposition techniques for aluminum oxide sputtering is of great importance. In this work, the aluminum oxide layers were deposited on top of organic semiconductor films in two different sputtering chambers with different geometries (see Fig. 5.5).

[1]Oxford Applied Research, Mini E-Beam Evaporator Model EGCO4, *Serial No.S1961/D59551*

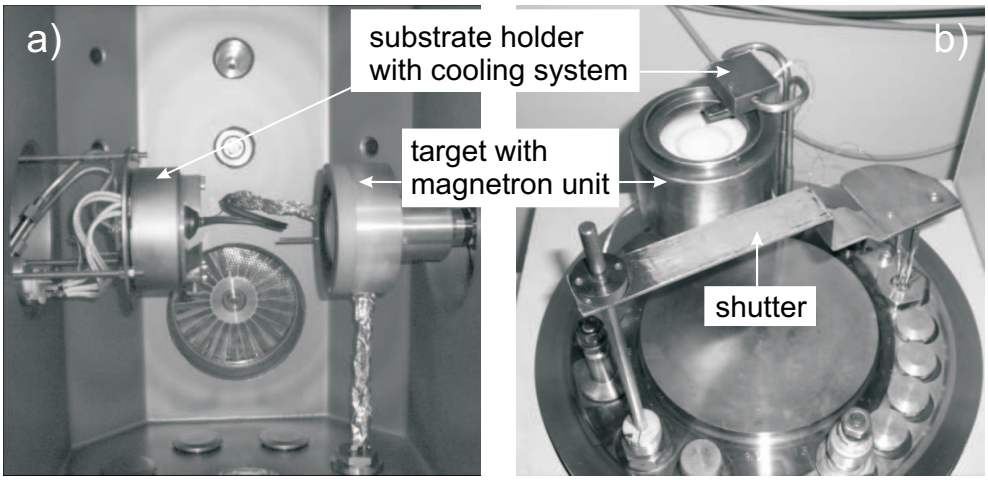

Figure 5.5: Photographs of the r.f. magnetron sputtering systems used. (a) *Leybold UNIVEX 350* vacuum system with a *Stiletto Magnetron sputtering source* from *AJA International* in horizontal geometry. (b) *Edwards Auto 306* system with *Edwards 75 mm magnetron cathode* and homebuilt substrate cooling system and sample stage in vertical geometry.

One sputtering system was a *Leybod UNIVEX 350* vacuum system with an integrated sputtering unit from *AJA International* (see Fig 5.5(a)). It is situated in the department of Prof. Dr. K. von Klitzing at the Max-Planck-Institut für Festkörperforschung in Stuttgart. The system is exclusively used for the sputtering of aluminum oxide films and base pressures in the 10^{-8} mbar regime were achieved. The *Stiletto* magnetron sputtering source (*ST30-ISO160K RF/DC*) from *AJA International* faces the water cooled substrate holder in a horizontal geometry at a distance of ~ 11.5 cm. For the sputtering of our aluminum oxide layers in this system sputtering powers in the range of 120−200 W were used.

The other sputtering system was an *Edwards Auto 306* with an implemented 75 mm planar magnetron cathode from *Edwards*. It is situated in the group of Dr. B. Gompf / Prof. Dr. M. Dressel from the 1. Physikalisches Institut of the University of Stuttgart. The *Edwards Auto 306* is pumped by an oil vapor diffusion pump (*Edwards EO4/160K*), backed by a rotating pump (*Edwards E2M8*) and it is capable of pumping the process chamber down to a pressure below 2×10^{-7} mbar. The sputtering target and the sample stage were mounted in a vertical geometry as shown in the photograph of Fig. 5.5(b). The substrate was mounted on a homebuilt sample stage which consisted of a copper

block for substrate cooling and a shutter system. The film thickness and deposition rate were monitored by a quartz crystal microbalance and the substrate temperature was measured by a thermoelement couple. The target-substrate distance was 3.5 cm. The aluminum oxide films sputtered in this system were prepared at a power range from 60−70 W. Both sputtering systems were supplied by a *Dressler* (CESAR) r.f. power generator (13.56 MHz).

For sputtering the dedicated sputtering chambers were pumped down until a base pressure of 3×10^{-7} mbar or lower was reached. To avoid oxidation of the organic film we used pure argon as sputter gas. Regarding the oxygen content this leads to an understoichiometric target after some sputter cycles which had been overcome by regenerating the target after each deposition in an oxygen/argon atmosphere (p(Ar)$\approx 5\times10^{-3}$ mbar, p(O_2) $\approx 2\times10^{-3}$ mbar). Pure argon was filled into the chamber until a partial pressure of 1×10^{-3} mbar was attained and the plasma could be ignited. The argon partial pressure during sputtering was $2.6-2.8 \times 10^{-3}$ mbar. The deposition rate and film thickness were monitored by a QCM. The deposition rates were about 7 Å/min and aluminum oxide films of 160 Å to 6000 Å thickness were prepared. The substrate was mounted on a copper block which allowed for a substrate temperature of −10°C during the sputtering process (measured by a thermoelement couple). For the *Edwards* sputtering system a feedback system terminated the sputtering process automatically after the desired film thickness was reached by closing a shutter while for the other system no shutter unit was available and therefore the sputtering power had to be ramped.

5.2 Setup for in-situ X-ray diffraction experiments

For the *in-situ* study of the thermal stability of organic films capped with an aluminum oxide layer a so-called Johanna-Otto oven (JOO) was used. Such a sample environment is shown in Fig. 5.6.

The oven is equipped with a small turbo-molecular pump, which allows for working in a pressure regime down to 10^{-6} mbar. It has a sample heater which can also be cooled and a kapton window which by its low absorption for X-rays allows for use in X-ray diffraction measurements. The temperature was measured with a C-type thermocouple fixed close to the sample on the heater and calibrated in preceeding tests.

The design of the JOO allows to be mounted on standard diffraction tables at syn-

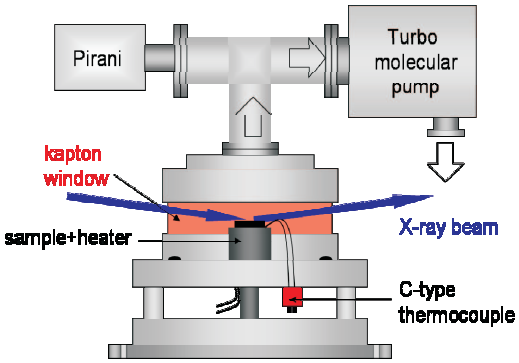

Figure 5.6: Schematic representation of the Johanna-Otto oven used for *in-situ* temperature-dependent XRD measrurements of AlO_x/organic films.

chrotron sources. The heater was controlled by a temperature controller (*Eurotherm 2408*) with a relative precision of $\Delta T \leq 1\,^{\circ}C$.

5.3 X-ray diffraction

For the background of surface and interface sensitive X-ray scattering techniques we refer to [155–162]. Here, only the key points will be mentioned.

5.3.1 The optical index of refraction and total external reflection

The domain of validity of X-ray reflectivity is limited to small angles of incidence where it is possible to consider the electron density as continuous. The elastic scattering of X-rays with matter can then be well described by an index of refraction which characterizes the change of direction of the X-ray beam when traversing the interface of two materials with different electron densities. For X-rays the refractive index,

$$n = 1 - \delta + i\beta\,, \tag{5.1}$$

is slightly less than one so that total external reflection can occur. Here, $\delta = \lambda^2 r_e^2 \rho / 2\pi$ and $\beta = \lambda\mu/4\pi$ account for the dispersion and absorption of the material, respectively (λ is the wavelength, $r_e = 2.82\times10^{-5}$ Å is the classical electron radius, ρ is the electron density and μ is the absorption coefficient).

For the total external reflection to occur, the incident angle, θ_{in}, must be smaller than the so-called critical angle, $\theta_{in} \leq \theta_c = \sqrt{2\delta}$. This is a very useful phenomenon

since under these conditions only an evanescent wave propagates below the surface, and hence surface sensitivity is considerably enhanced [155] (see grazing incidence diffraction below).

5.3.2 The dynamical theory

X-ray reflectivity

The reflection and transmission of X-rays can then be treated as a classical problem of reflection of an electromagnetic wave at an interface [162]. The Fresnel relationship for a flat surface yields,

$$R_F(q_z) = \left| \frac{q_z - \sqrt{q_z^2 - q_c^2 - \frac{32i\pi^2\beta}{\lambda^2}}}{q_z + \sqrt{q_z^2 - q_c^2 - \frac{32i\pi^2\beta}{\lambda^2}}} \right|^2 . \tag{5.2}$$

with the wave vector transfer $\mathbf{q} = (0, 0, q_z = 4\pi \sin\theta/\lambda)$.

The recursive Parratt formalism

For a medium consisting of slabs of different electron densities and thicknesses (see Fig. 5.7(a)) the reflected intensity can be calculated by applying the boundary conditions of the electric and the magnetic fields at each interface. This leads to the dynamical theory which takes multiple reflections into account. The dynamical theory is described in detail in the monographs [163–165]. A recursive formalism was presented the first time by Parratt [165] and the reflected intensity is given by,

$$X_j = \frac{|r_j|^2}{|t_j|^2} = e^{-2ik_{z,j}z_j} \frac{r_{j,j+1} + X_{j+1}\, e^{2ik_{z,j+1}z_j}}{1 + r_{j,j+1} X_{j+1}\, e^{2ik_{z,j+1}z_j}} , \tag{5.3}$$

with the Fresnel coefficients

$$r_{j,j+1} = \frac{k_{z,j} - k_{z,j+1}}{k_{z,j} + k_{z,j+1}} . \tag{5.4}$$

However, real surfaces and interfaces have a certain roughness which can be accounted for by the modified Fresnel coefficient given by,

$$r_{real} = r_{ideal} \cdot e^{-2k_{iz}k_{fz}\sigma^2} , \tag{5.5}$$

where σ is the roughness of the interface.

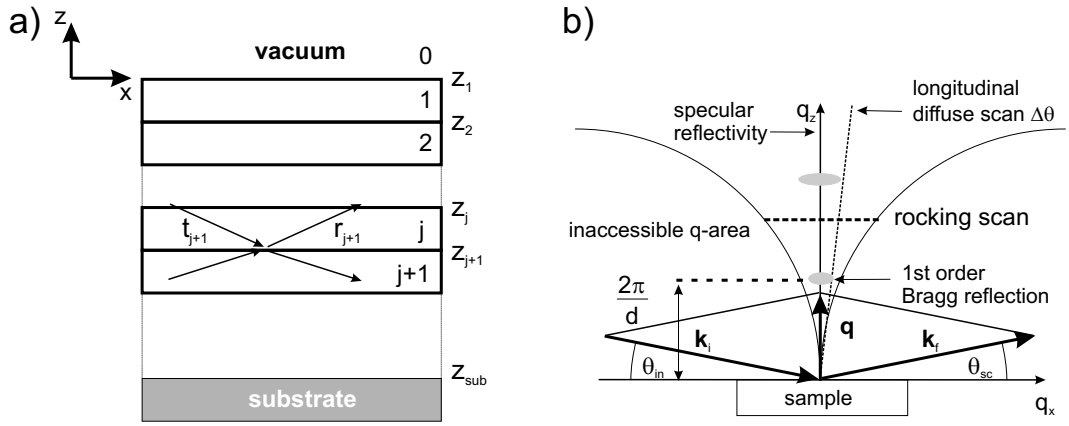

Figure 5.7: Schematic representation of (a) the recursive formalism by Parratt and (b) the accessible q-area with specular-, longitudinal- and rocking-scans.

The reflectivity in Eq. 5.3 does present periodic oscillations in reciprocal space with $\Delta q_{z,j} = 2\pi/D_j$. The oscillations are the result of constructive interferences between the reflected waves at the interfaces and their period gives the thickness, D_j, of the respective layer.

If a film has a periodic structure in the out-of-plane direction the path difference between the reflected waves from two neighboring scattering planes gives rise to Bragg reflections according to the Bragg condition, $n\lambda = 2d_{film} \sin\theta_{Bragg}$.

5.3.3 The kinematical approximation

If the angle of incidence is not too small, multiple scattering can be neglected. With the Born approximation the kinematical theory can be derived which is more flexible to use. The kinematical scattering theory is discussed in more detail in the monographs [163, 166, 167]. In this case, the reflected intensity can be written as

$$R(q_z) = R_F(q_z)\left|\frac{1}{\rho_s}\int_{-\infty}^{\infty}\frac{d\rho(z)}{dz}\,e^{iq_z z}dz\right|^2, \tag{5.6}$$

with the Fresnel-reflectivity given by Eq. 5.2.

A schematic representation of the specular reflectivity geometry is shown in Fig. 5.8(a). The incident and reflected beams are in one plane and its normal is perpendicular to the normal of the substrate surface.

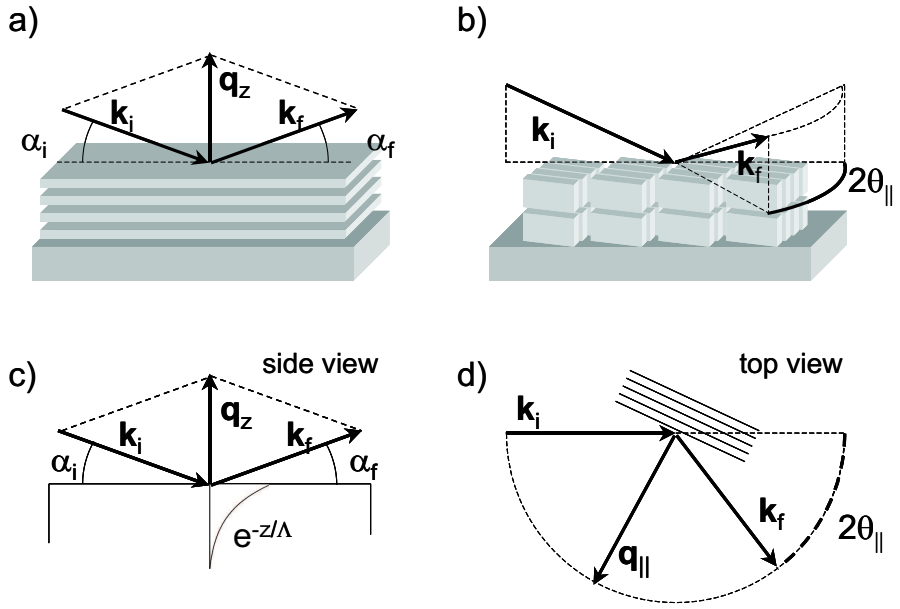

Figure 5.8: Schematic representation of the (a) specular and (b-d) grazing incidence XRD geometries. (a) For the specular geometry $\theta_{in} = \theta_{sc}$ and the normal of the plane spanned by $\mathbf{k}_{in}$ and $\mathbf{k}_{sc}$ is perpendicular to the normal of the substrate surface. (b) Below the critical angle θ_c the incoming X-ray beam forms an evanescent wave which is exponentially damped along the surface normal and which has a component along the interface which gives rise to scattering in-plane. (c) and (d) represent a top and side view of the GIXD geometry.

5.3.4 Diffuse scattering

For rough surfaces (interfaces) a significant part of the reflected intensity is scattered off-specular. These incoherent parts are designated as diffuse scattering. Since the scattering vector $\mathbf{q}$ has now also a component $q_{||}$ in the surface plane the X-ray scattering experiments contain information on the statistical properties of surfaces or interfaces. The lateral length of surface morphologies can be studied via transverse rocking scans and the correlations between buried interfaces can be investigated by performing longitudinal off-specular scans. The different scans in reciprocal space are illustrated in Fig. 5.7(b).

For small angles (in the kinematical approximation), the diffuse scattering can be described after Sinha *et al.* [168] by,

$$I_{diffuse} \propto \frac{(\Delta\rho)^2}{q_z^2} e^{-q_z^2\sigma^2} \int [e^{q_z^2 C(R)} - 1]\, e^{iq_{||}r_{||}} dr_{||}\,. \tag{5.7}$$

For isotropic surfaces Sinha *et al.* have used the following functional form

$$C(R) = \sigma^2 e^{-(R/\xi)^{2h}} . \tag{5.8}$$

The roughness exponent h is the key parameter which describes the height flucutations at the surface. The roughness σ governs the amplitude of the fluctuations and the parameter ξ is the correlation length of the height fluctuations.

5.3.5 Grazing incidence X-ray diffraction

As mentioned already above, for $\theta_{in} < \theta_c$ the X-ray reflection is accompanied by an evanescent wave field which propagates along the interface between the two media. The amplitude of this evanescent wave is exponentially damped along the inward surface normal with a decay length Λ (typically in the range of a few nanometers) [155,160,169],

$$E_t \sim e^{i\mathbf{k}_{||}\mathbf{r}_{||}} e^{-z/\Lambda} . \tag{5.9}$$

Therefore, GIXD is a surface sensitive diffraction method and by varying the angle of incidence the probed depth of the material can be adjusted. A schematic representation of the grazing incidence geometry is shown in Fig. 5.8(b). Figures 5.8(c) and (d) show a side and a top view of the GIXD geometry, respectively. Since the evanescent wave is propagating laterally scattering planes in the surface plane can give rise to Bragg reflections.

5.3.6 Experimental details

X-ray reflectivity (XRR), grazing incidence X-ray diffraction (GIXD) and diffuse X-ray scattering were used to determine the structural properties of organic films and inorganic/organic heterostructures. From X-ray reflectivity measurements the electron density profile, ρ(z), and from the out-of-plane Bragg peaks the lattice parameter of the organic film structure and the coherent thickness were determined.

The X-ray diffraction measurements requiring high intensities were performed at the surface diffraction beamline of the MPI for metals research at the ANKA[2] synchrotron radiation source in Karlsruhe (Germany) and at the beamline ID10B[3] at the

[2] more details on the beamline setup and characteristics are available on the ANKA webpage, *http://hikwww1.fzk.de/anka/*

[3] more details on the beamline setup and characteristics are available on the ESRF webpage, *http://www.esrf.fr*

ESRF synchrotron radiation source in Grenoble (France) (at energies ranging from 11.5–15 keV). For the pre-characterization of the samples and for longterm experiments laboratory X-ray sources at the MPI for metals research in Stuttgart (with Cu_{K_α} radiation, $\lambda = 1.541$ Å) were used.

The surface diffraction beamline at ANKA is a multipurpose beamline. The ANKA storage ring is operated at 2.5 GeV. The optics elements consist of a Rh coated Si toroidal mirror for vertical beam focussing followed by a Si(111) double crystal monochromator with a saggital bender. Figure 5.9 shows schematically the setup, sketching the slit locations and the employed scattering geometries of the surface diffraction beamline at ANKA. σ_{iV} and σ_{iH} are the vertical and horizontal slits in front of the sample, whereas σ_{fV} and σ_{fH} are the detector slits governing the resolution of the experiment. α_i denotes the incident angle of the X-rays on the sample. 2θ is the detector angle in grazing-incident X-ray-diffraction scans. In specular scans, 2θ(HK0) is set to 0° and the detector angle is set to 2 α_i.

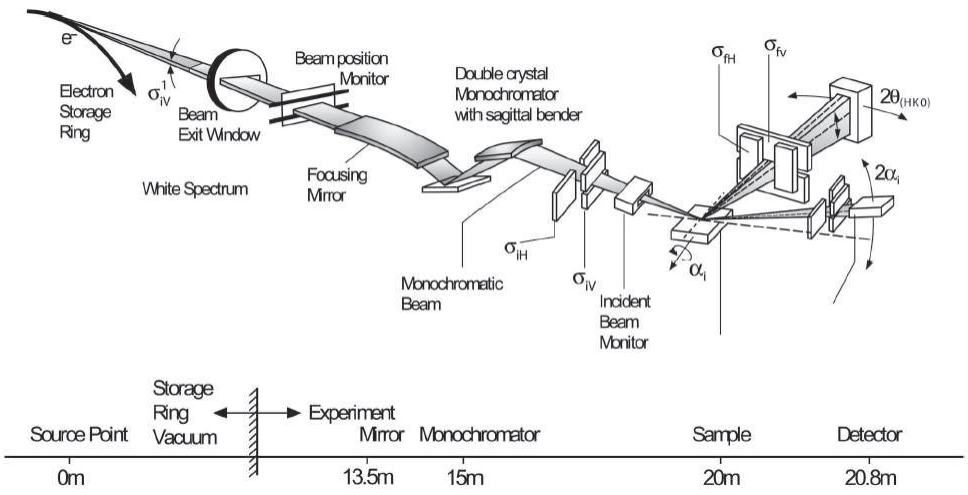

Figure 5.9: Schematic representation of the surface diffraction beamline at ANKA. The slit settings and the distances between the different elements are indicated in the lower panel.

The ID10B beamline is a multi-purpose, high-brilliance undulator beamline for high resolution X-ray scattering. The electron storage ring (ESRF) is operated at 6 GeV. The beamline optics consist of a diamond (111) double crystal monochromator (intrinsic energy resolution $\Delta E/E = 5.9\times10^{-5}$) and a double-mirror setup for a strong suppression

of higher harmonics.

For specular XRR experiments at both synchrotron radiation sources the angular resolution as determined by the detector slit setting was in the range of $\Delta 2\theta = 0.014$– $0.021\,^{\circ}$. For the relatively broad in-plane Bragg reflections a resolution of $\Delta 2\theta = 0.072\,^{\circ}$ was used. Off-specular data were recorded at offset angles between 0.04– $0.05\,^{\circ}$ depending on the rocking width of the sample.

The specular X-ray reflectivity data were normalized and diffuse (off-specular) scattering was subtracted to extract the true specular signal. The data were fitted either with *BOCFIT*, a program based on the Parratt formalism (dynamical theory) or with *MAFFOX*[4], a program based on the kinematical approximation.

5.4 Complementary techniques

5.4.1 Atomic force microscopy

Scanning probe microscope (SPM) techniques are an important tool for surface science and the characterization of surface structures. They provide images of surface properties in real space and with atomic resolution. The principle for the different SPM techniques [170, 171] is based on a small tip on a cantilever scanning the surface of a sample at small distances where different types of interactions (electrical, mechanical, magnetic, etc.) are present. Their spatial variation can be obtained from an SPM image.

Mode of operation

The atomic force microscope (AFM) is based on the van-der-Waals interaction between the tip and the sample surface and therefore has the advantage that it can be used on conductors, semiconductors as well as on insulators. The van-der-Waals interaction can be described by a Lennard-Jones Potential (see Fig. 5.10),

$$U(R) = \frac{A}{R^{12}} - \frac{B}{R^{6}}, \tag{5.10}$$

where A and B are element specific constants and R is the distance between two atoms.

[4] written by A. Gerlach, Physical and Theoretical Chemistry Laboratory, Oxford University

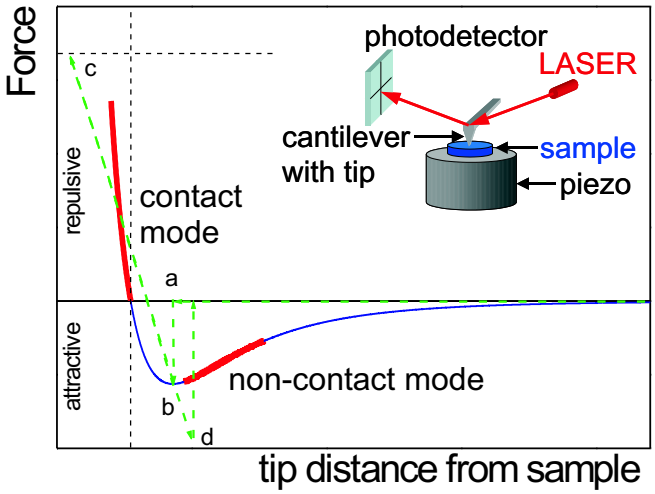

Figure 5.10: Regimes in the force-distance diagram for AFM measurements in the contact and non-contact mode. The dashed line indicates the motion of the cantilever as a function of the distance to the sample surface. At 'a' the interaction is so strong that the tip gets in contact with the sample surface ('b'). In the regime 'b-c' the repulsive forces bend the cantilever in the opposite direction. When removing the cantilever the tip looses contact to the sample surface at 'd'.

At long distances from the sample surface the bending of the cantilever due to the attractive forces is negligable. When the tip is at certain distance a, the bending of the cantilever is so strong that the tip gets in contact with the sample surface (point b). For smaller distances the cantilever is bent in the opposite direction as a result of the repulsive forces. In this regime $(b-c)$ the deflection of the cantilever is a linear function of the distance. Removing the tip from the surface leads to loosing of contact with the sample surface at a point d which is much larger than the distance a.

There are two regions in the force-distance curve (Fig. 5.10) where AFM measurements can be performed. In the region where the tip is in contact with the sample surface (*contact-mode*) the force (and therefore also the deflection of the tip) is very sensitive to small variations of the distance whereas in the *non-contact* region the attractive forces are much weaker and therefore a different detection mode based on the resonance frequency of the cantilever is applied.

The deflection of the cantilever arm due to the van-der-Waals interaction is typically monitored by a laser reflected onto a position sensitive diode array as it is scanned over the surface and thus it provides a topographic image of the sample surface (Fig. 5.10 (inset)).

Experimental details

For the investigation of the as-grown films a commercial room-temperature Omicron AFM/STM system located in the UHV analysis chamber (see Fig. 5.2) was used. It can be operated either in the contact mode or in the non-contact mode and scan ranges up to 5 μm are possible. For AFM measurments in the contact mode rectangular cantilevers with a normal spring constant of 0.1 or 0.01 N/m were used. To avoid damage of the surface the measurements were conducted at low load. For scan ranges beyond 5 μm an AFM in air was used and the measurements were performed in the tapping mode.

5.4.2 Transmission electron microscopy on organic thin films

From cross-sectional transmission electron microscopy (TEM) measurements a real space image of the interface structure of Al_2O_3/DIP can be obtained.

The preparation of cross-sectional TEM specimens is rather difficult due to the sensitivity of the organic material upon local heating. Dürr *et al.* presented a route for the preparation of organic specimens [55] and this route was successfully applied for the preparation of cross-sectional TEM specimens of Al_2O_3/DIP.

The measurements were performed on a Philips CM 200 at 200 kV with a resolution of 2.7 Å in the group of Prof. Dr. M. Rühle at the Max-Planck-Institut for metals research in Stuttgart.

5.4.3 Rutherford backscattering spectroscopy

For the determination of the stoichiometry of the aluminum oxide layers Rutherford backscattering (RBS) was used. The measurements were carried out with He^+ ions of 1 MeV in the group of Prof. Dr. W. Bolse at the Dynamitron in Stuttgart. The RBS-chamber has an IBM-geometry (*i.e.*, the detector is located at $\theta = 165\,^\circ$ scattering angle in the same plane as the beam and the normal to the sample) with a detector resolution

of 14 keV FWHM. The data were analysed with the software RUMP[5].

5.4.4 Optical microscopy

After heating the capped DIP samples the sample surfaces were investigated by optical microscopy. Herefore, the samples were studied in the polarized light of an *Olympus BX61* which allowed for magnifications ranging from 50 to 1000.

[5]Rutherford Backscattering Spectroscopy analysis package built on Genplot, this package provides comprehensive analysis and simulation of RBS and ERD spectra.

6 Growth and structure of organic semiconductor films

The main part of this thesis is devoted to organic semiconductor films capped by an aluminum oxide layer and the thermal stability of such systems. Therefore, first the precise knowledge of the structure and morphology of organic semiconductor films is necessary.

For the application in organic field-effect transistors (OFETs) the preparation of organic films with a high degree of order is desired. Small conjugated molecules (as presented in Sec. 3.1) evaporated under ultra-high vacuum conditions have proven to form highly crystalline films under optimized preparation conditions [7, 12]. The structure of such films drastically depends on the molecular structure, the substrate material and the preparation conditions. To guarantee a high degree of intermolecular π-orbital overlap of adjacent molecules a detailed study of the organic film structure is necessary.

In this chapter the structures and morphologies of thin films of perfluorinated copper phthalocyanines (F_{16}CuPc) (Sec. 6.1), pentacene (Sec. 6.2) and diindenoperylene (DIP) (Sec. 6.3) on silicon wafers are presented. Some recent works have contributed to the understanding of the structural, electrical and optical properties of such films and for more details we refer to these references [11, 53, 57]. In Sec. 6.4 we performed *in-situ* real-time growth experiments of the organic semiconductor DIP.

For the encapsulation of organic films we are looking for a model system which has the potential for use in OFETs and which from a structural point of view offers a wide range of deposition conditions under which it forms highly ordered films.

6.1 F_{16}CuPc on silicon wafers

The perfluorinated copper-phthalocyanine (F_{16}CuPc) was presented in Sec. 3.1. Under optimized preparation conditions films of F_{16}CuPc on silicon oxide form long needles of high crystallinity [53, 172]. A typical AFM (c.m.) image of F_{16}CuPc on silicon oxide is displayed in Fig. 6.1.

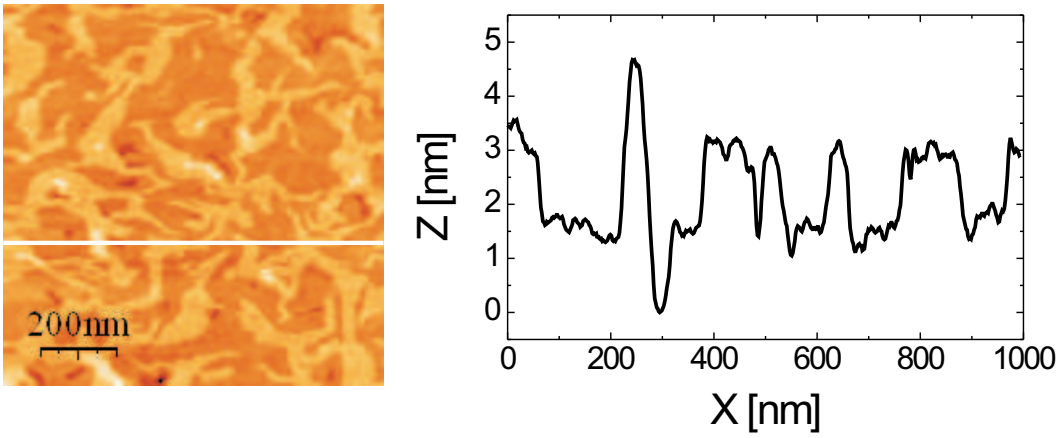

Figure 6.1: AFM (c.m.) image with profile scan of a 57 Å thick F_{16}CuPc film on silicon oxide.

The film was prepared at $T_{substr.} = 230\,^{\circ}C$ at a deposition rate of ~ 1 Å/min. The film thickness of this sample was 57 Å (as determined from XRR measurements, see below) which corresponds to four to five monolayers of upright-standing molecules.

The height distribution of this image is displayed in Fig. 6.2(a). Four different layers can be recognized and the height distribution can be fitted by four Gaussians. From the position of each Gaussian the step height difference can be obtained (see Tab. 6.1) and from the area under each Gaussian the area covered by each layer can be extracted. The step height corresponds to monomolecular layers of essentially upright standing molecules which have a certain tilt angle to the surface normal.

Figure 6.2(b) illustrates the height distribution. The lowest layer (1) is covered to 98.6 % by the layer 2 which again is covered to 43.5 % by the layer 3 and the topmost layer (4) covers 1.2 % of the total scan area. The step heights do also change from one layer to the next. The height differences are 1.26 nm, 1.29 nm and 1.44 nm starting from

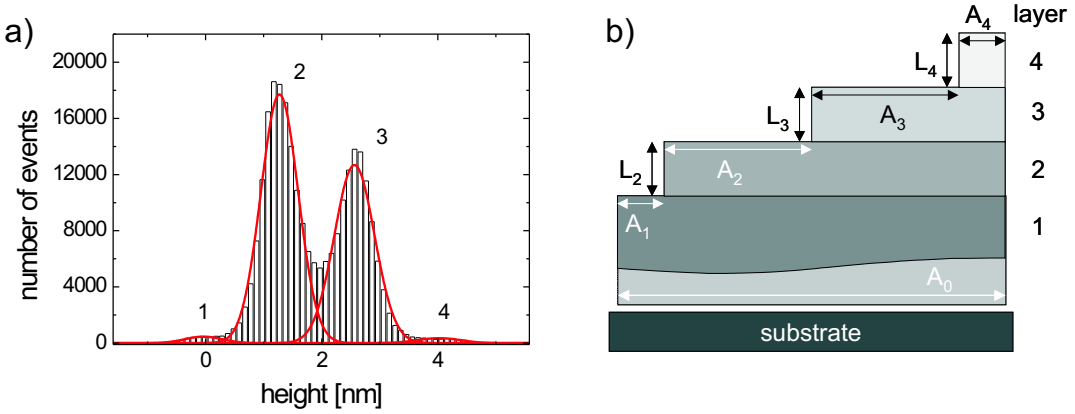

Figure 6.2: (a) Height distribution of a topographic AFM image of $F_{16}CuPc$ on silicon oxide. The analysis of this histogram reveals four contributions (two strong and two weak peaks). The portions of the areas of different height are displayed in (b).

layer	x_c [nm]	width [nm]	Area [nm^2]	step height [nm]	coverage [%]
1	0	0.606	371	0	100.0
2	1.31	0.614	14284	1.31	98.6
3	2.60	0.665	11001	1.29	43.6
4	4.05	0.712	331	1.45	1.3

Table 6.1: Results of Gaussian fit to the height distribution of $F_{16}CuPc$ film on silicon oxide.

the lowest layer. Considering that the phthalocyanine molecule has a length of 1.45 nm this means that the molecules are all standing in an upright configuration with a tilt angle to the surface normal.

The structure of $F_{16}CuPc$ films was investigated by XRR measurements at room temperature on an in-house station (high-resolution six-circle diffractometer, Cu_{K_α}). Figure 6.3 shows two X-ray reflectivity curves of $F_{16}CuPc$ films of different thickness (data are offset for clarity). The thinner film had a thickness of 57 Å and a roughness of $\sigma = 3$ Å while the thicker film had a thickness of 170 Å with a roughness of $\sigma = 9$ Å. The data show pronounced Kiessig fringes and Laue oscillations around the first order Bragg reflection of $F_{16}CuPc$ which is located at $q_z = 0.436$ Å, corresponding to a lattice spacing

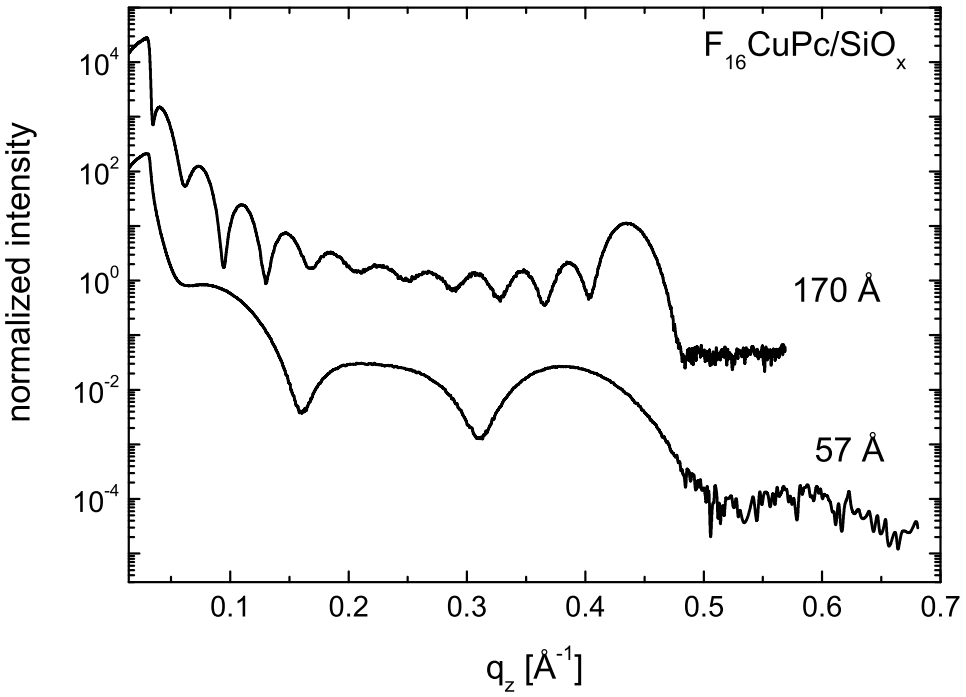

Figure 6.3: Specular X-ray reflectivity scans of two F_{16}CuPc films of different thickness (57 Å and 170 Å) on silicon oxide showing pronounced Kiessig interference fringes and the first order Bragg reflection with Laue oscillations.

of 14.4 Å. A more detailed analysis of the growth of F_{16}CuPc on different substrates can be found in [173].

6.2 Pentacene on silicon wafers

The structure of pentacene films has been studied extensively [74, 78, 174] due to its promising electrical properties. On silicon oxide pentacene forms crystalline films and different polymorphs – a 'thin film' phase and a 'bulk' phase – are reported depending on the preparation conditions [7, 79, 175, 176]. Both phases may be present in a film and their ratio depends on the substrate temperature and on the film thickness. At lower substrate temperatures the 'thin film' phase is formed but from a certain critical

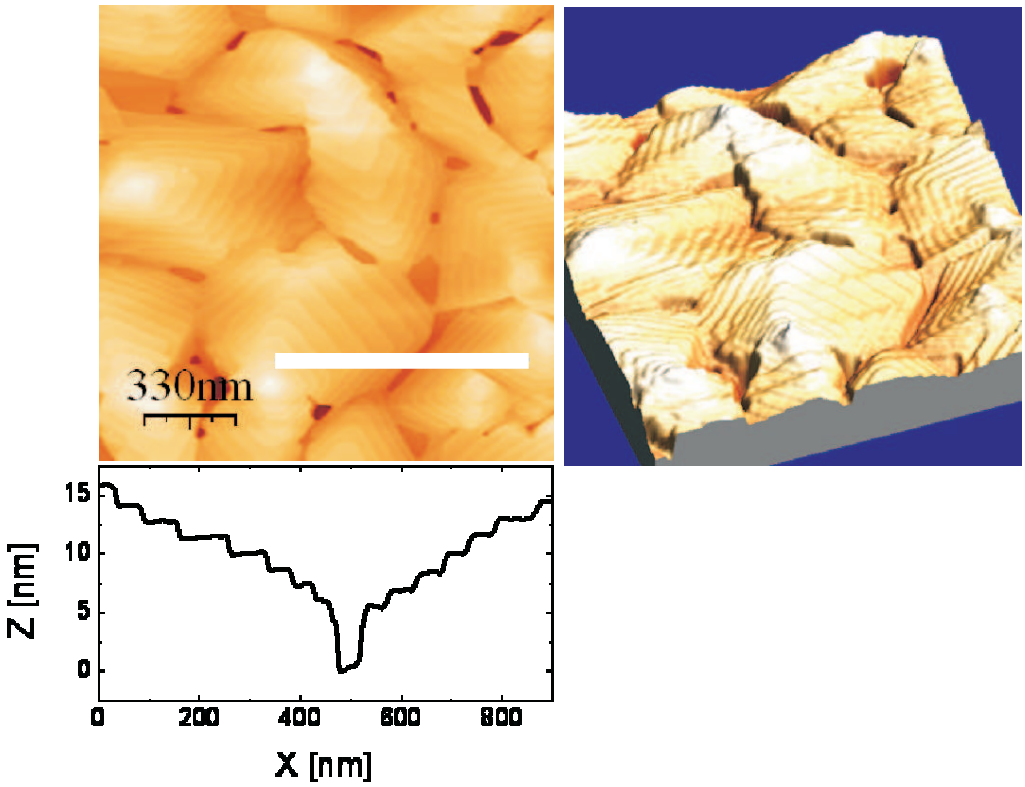

Figure 6.4: AFM (c.m) image of a 170 Å thick pentacene film on silicon oxide.

thickness on (which depends on the substrate temperature) [79] the 'bulk' phase evolves and dominates for thicker films.

We have prepared pentacene films on silicon oxide ($T_{substr.} = 40\,°C$) at thicknesses below the critical film thickness so that only the 'thin film' phase is expected. A typical AFM (c.m.) image of a 170 Å thick pentacene film is shown in Fig. 6.4. From the profile along the white line the step height of the individual monolayers can be obtained. The first layer of pentacene on silicon oxide forms single crystal islands with a lateral size of a few micrometers [108] and subsequent layers grow in a terrace-and-step morphology [7].

The pentacene film in Fig. 6.4 shows grains with a strong facetting behavior which is typical for the 'thin film' phase. The facetting behavior is observed on every terrace. Remarkably, the angles formed by the sides of the individual terraces seem to be consistent with the angles of the *ab*-plane of the triclinic unit cell of pentacene [7, 174] (see

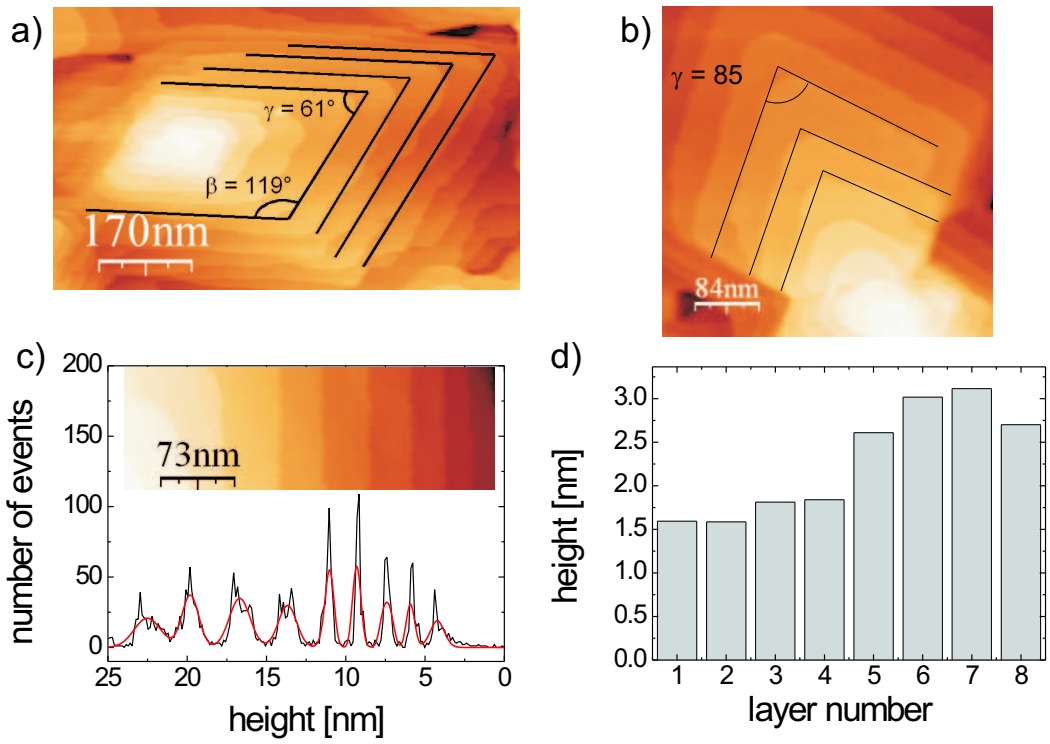

Figure 6.5: Analysis of the angles of the individual terraces of pentacene on silicon oxide. The terraces in AFM image (a) have angles of $\beta = 119\,^\circ$ and $\gamma = 61\,^\circ$ while in (b) the angles are close to $85\,^\circ$. From a profile scan along the long axis of the inset in (c) the height distribution is obtained. The resulting heights for the different layers are displayed in (d).

Fig. 6.5(a,b)) and oriented along the $[1\bar{1}0]$ and the [110] unit cell direction [79].

The terrace structure leads to deep 'valleys' which allow to determine the step height of the individual monolayers. We note, that the pentacene film thickness was about 163.6 Å as determined from the XRR measurements and fitting of the data by the Parratt formalism (see below). The height distribution of the AFM image in Fig. 6.5(c) can be fitted by a series of nine Gaussians. From the separation of the individual Gaussians the height difference of subsequent terraces is obtained (d). The pentacene molecule has a length of 16.1 Å. Therefore, the molecules of the lowest two layers (which are not necessarily the first two monolayers of the film) are standing upright with a tilt angle of ca. $8\,^\circ$ to the surface normal. The next two layers revealed heights of 18.1 and 18.4 Å which is larger than the length of the molecule and the next terraces have a

height of 26.1 Å, 30.2 Å, 31.2 Å and 27.0 Å respectively. These large height differences are probably due to two layers of 13.0−15.6 Å in thickness.

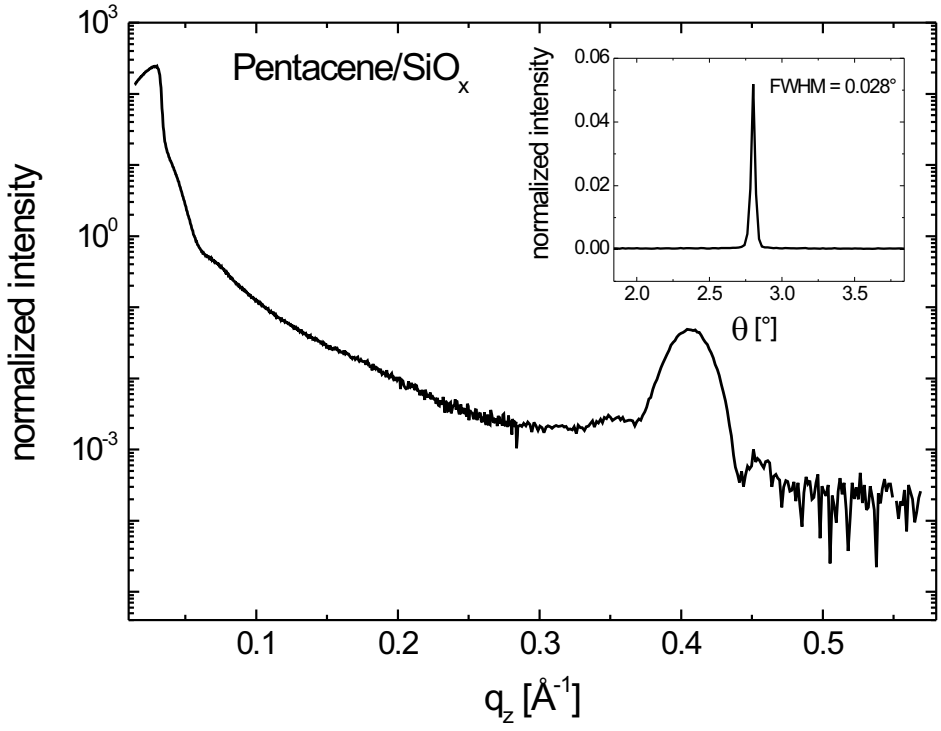

Figure 6.6: Specular X-ray reflectivity of a 170 Å thick pentacene film on silicon oxide. The first order pentacene Bragg reflection at $q_z = 0.406\,\text{Å}^{-1}$ corresponds to the lattice spacing of the 'thin film' phase (15.48 Å).

The lattice plane distance along the surface normal could also be determined from the position of the pentacene Bragg reflection in XRR measurements ($q_z = 0.406\,\text{Å}^{-1}$) in Fig. 6.6 and a value of 15.48 Å was obtained. This value is in good agreement with the AFM data and corresponds to reported values for the 'thin film' phase. From fitting procedures based on the Parratt formalism a film thickness of 170 Å and a film roughness of 35.2 Å was obtained for the reflectivity data.

6.3 DIP on silicon wafers

6.3.1 High substrate temperature

When prepared under suitable conditions ($T_{substr.} = 145\,°C$, deposition rate $R = 12\,Å/min$) [12] organic films of DIP deposited on silicon oxide exhibit a high structural order. These films form large flat terraces with a step height of 16.5 Å as can be seen by the contact AFM image in Fig. 6.7. This value corresponds to the lattice spacing as determined from the position of the DIP Bragg reflection (see below).

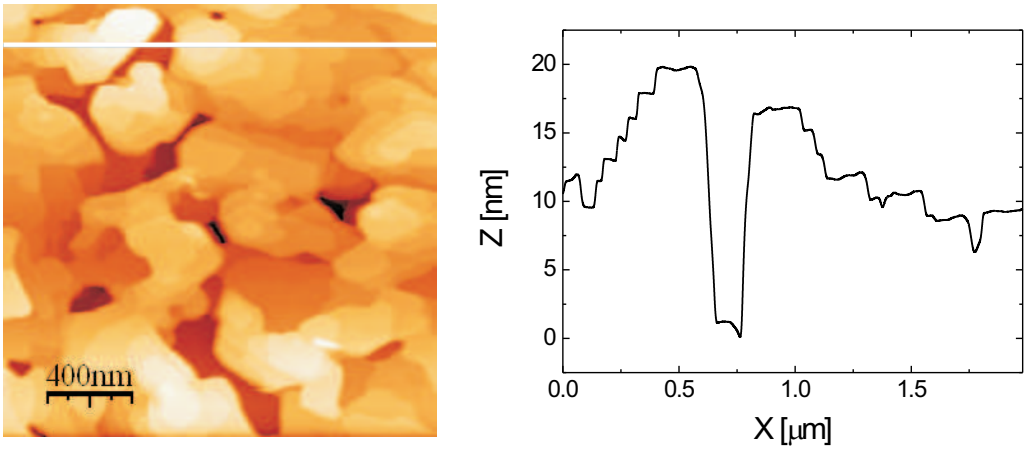

Figure 6.7: AFM (c.m.) image of DIP on silicon oxide prepared at $T_{substr.} = 145\,°C$. DIP forms large flat terraces with a step height of 16.5 Å corresponding to upright standing molecules.

The structure of the organic thin films was investigated by X-ray diffraction measurements. Figure 6.8 shows typical specular X-ray reflectivity curves of DIP films of different thickness on silicon oxide.

The X-ray reflectivity data can be fitted by the Parratt formalism presented in Sec. 5.3.2 and the film thicknesses and roughnesses can be extracted. The DIP film corresponding to the upper curve had a film thickness of $\sim$ 276 Å with a roughness of σ=20.4 Å, the curve in the middle had a film thickness of $\sim$ 333 Å with a roughness of σ=22.1 Å, while the third film had a thickness of $\sim$ 700 Å with a roughness of σ=48.6 Å. All reflectivity curves show Kiessig interference fringes which are more pronounced for the thinner films. The total film thickness can be determined from the

observed Kiessig interference fringes. For the specific case of DIP the coherent thickness, as determined from the Laue oscillations around the first order DIP Bragg reflection (at $q_z = 0.38$ Å^{-1}), corresponds almost to the total film thickness indicating that the DIP films are coherently ordered over their entire thickness. For DIP films rocking widths of about 0.01 ° and lower were measured confirming the high crystalline order of the films in the out-of-plane direction. The films are polycrystalline with an isotropic orientation in-plane [25].

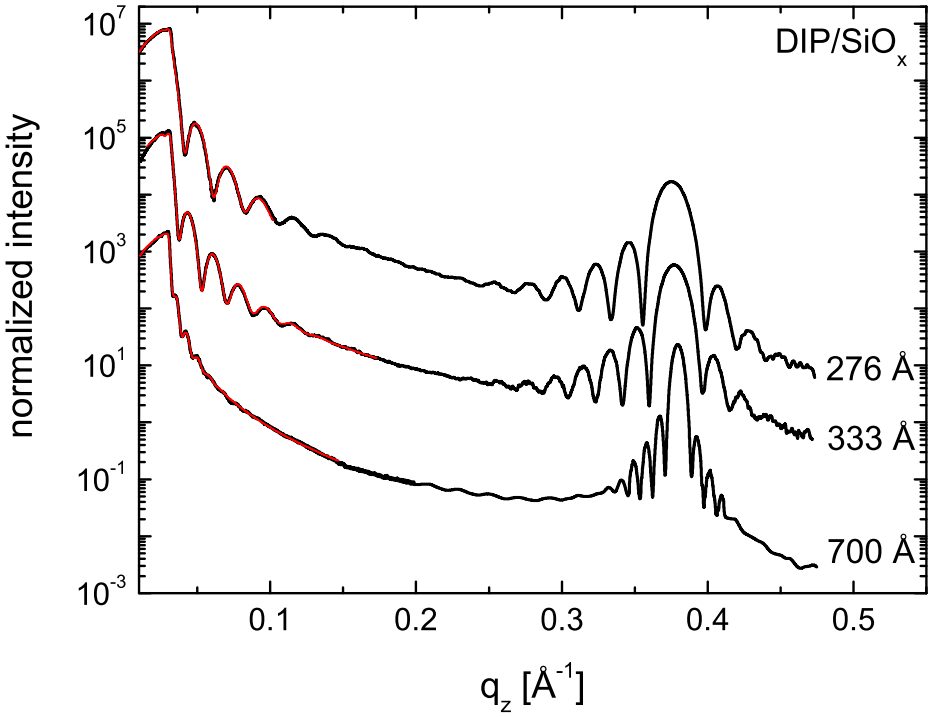

Figure 6.8: Specular X-ray reflectivity of three DIP films of different thickness on silicon oxide. The DIP film corresponding to the upper curve had a film thickness of $\sim$ 276 Å (σ=20.4 Å), the curve below corresponds to a film of $\sim$ 333 Å thickness (σ=22.1 Å) while the film thickness of the lowest curve was $\sim$ 700 Å (σ=48.6 Å). Besides a pronounced first order Bragg reflection at $q_z = 0.38$ Å^{-1} all DIP films show Kiessig interference fringes which damp out with increasing roughness (increasing film thickness).

6.3.2 Low substrate temperature

The growth and structure of DIP films depends also on the diffusion length of the DIP molecules on the substrate surface and thus on the substrate temperature. To study the effect of substrate temperature we prepared DIP films at low substrate temperatures (down to -160 °C) via liquid nitrogen cooling as described in Sec. 5.1.2. Before growth of the DIP film, the silicon wafer was cleaned and outgazed during 12 hours at 700 °C (see also Sec. 5.1.1). During deposition of the DIP film the pressure in the UHV chamber was around 8×10^{-11} mbar which reduced possible adsorption of water on the substrate surface. The AFM (contact mode) measurements were performed *in-situ* without leaving the vacuum but the measurements had to be performed at room temperature. Figure 6.9 shows an AFM (c.m.) image of a DIP film prepared at -160 °C. The morphology differs strongly from the terraced structure of the high substrate temperature sample in Fig. 6.7, see herefore also [53]. Here, the roughness was around 51 Å at a nominal

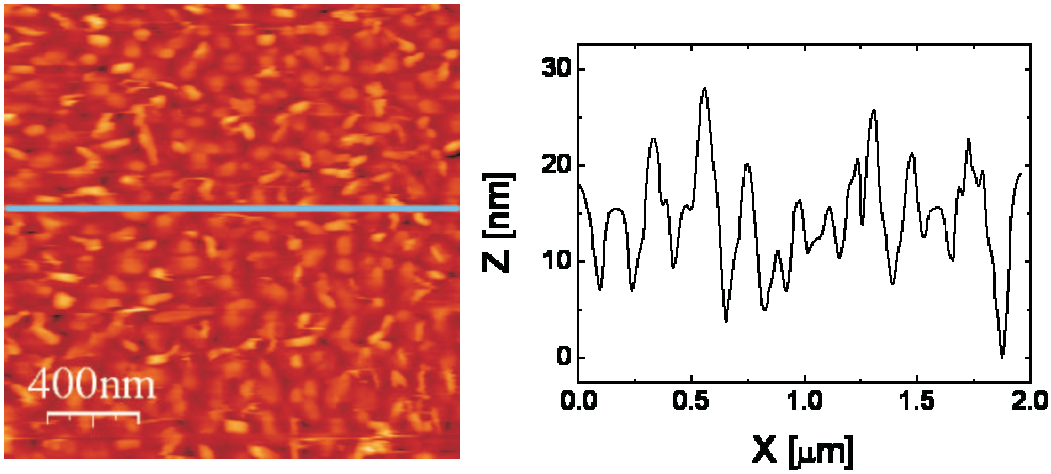

Figure 6.9: AFM (c.m.) image (taken at room temperature) of DIP on silicon oxide prepared at T = -160 °C. The DIP film shows a grainy morphology compared to the large flat terraces as shown in Fig. 6.7.

DIP film thickness of around 386 Å (as determined from XRR measurements).

Figure 6.10 shows a comparison of the XRR of DIP films prepared at substrate temperatures of 136 °C, -90 °C and -160 °C, respectively. While the film preparation was performed at the specific substrate temperatures, the XRR measurements were

performed at T = 80 °C for the sample prepared at 136 °C, and at room temperature for the two other samples.

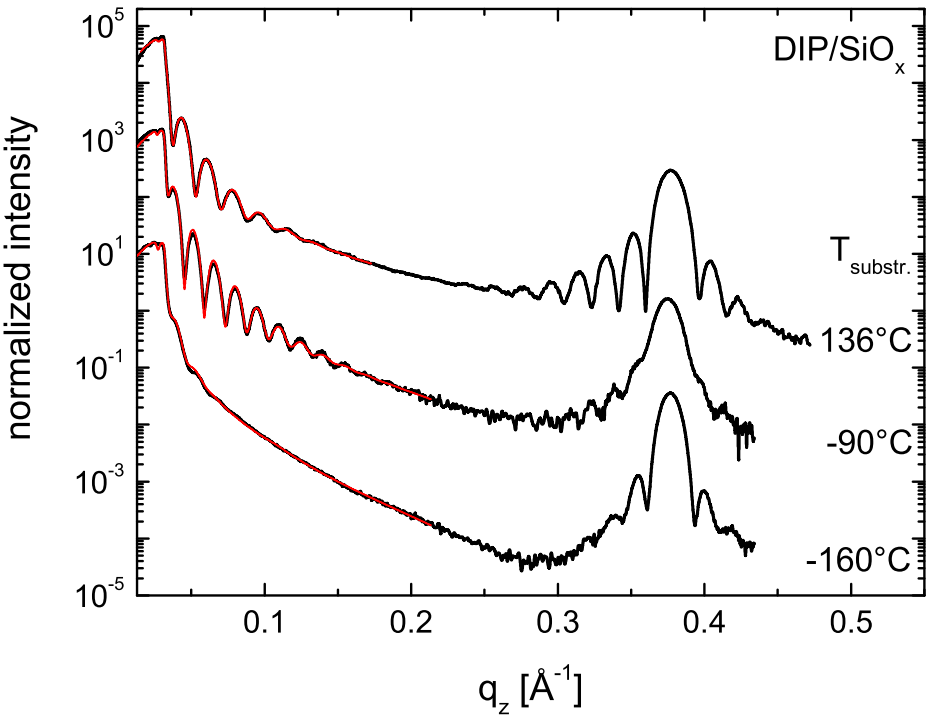

Figure 6.10: Specular X-ray reflectivities of DIP films prepared on silicon oxide at substrate temperatures of 136 °C, -90 °C and -160 °C. Measurements were performed at 80 °C for the 136 °C-sample and at room temperature for the two other samples.

All films showed DIP Bragg reflections with Laue oscillations. For the films prepared at low substrate temperature the Laue oscillations are less pronounced compared to samples prepared under optimized conditions indicating that the films are less coherently ordered. For the low-substrate temperature samples the rocking-widths were significantly higher (0.029 ° for the -90 °C-sample and 0.018 ° for the -160 °C-sample) as compared to the sample prepared at high substrate temperature (0.0087 °).

The substrate temperature, the deposition rate (R_{DIP}), and the results of fitting procedures of the Parratt formalism to the reflectivity curves are listed in Tab. 6.2. The

$T_{substr.}$	R_{DIP} [Å/min]	L_{DIP} [Å]	ρ_{DIP} [el/Å^3]	σ_{DIP} [Å]	$a_\perp$ [Å]	σ_{RD} [Å]
136	4.6	333	0.40	22.1	16.60*	74.3
−90	24.1	410	0.40	19.5	16.76	82.9
−160	12.9	386	0.43	51.1	16.68	80.2

Table 6.2: Comparison of the results (thickness, deposition rate, electron density and roughness) from fitting the XRR curves by the Parratt algorithm for DIP films prepared at different substrate temperatures. The DIP lattice spacings $a_\perp$ and the random deposition limits σ_{RD} are compared for the different samples. [*] The measurements were performed at T=80°C therefore $a_\perp$ has been corrected for the thermal expansion with $\alpha_\perp = 66.6\times10^{-6}$1/K.

comparison of the roughnesses of films prepared at different substrate temperatures and at different deposition rates is difficult since we expect different scaling behaviors ($\sigma = L^\beta$) for these films. The random deposition (RD) limit $\sigma_{RD} = a_\perp\sqrt{L_{DIP}/a_\perp}$, where L_{DIP} is the thickness of the DIP film and $a_\perp$ is the lattice spacing in the out-of-plane direction, is expected to provide an upper bound on the roughness, σ, that random fluctuations can induce during the growth of a thin film [177]. It applies in the absence of any mass transport between different layers of the growing film [178, 179].

Therefore, the random deposition limit σ_{RD} was calculated for each film from the lattice spacing $a_\perp$ as determined from the position of the first order DIP Bragg reflection and the film thickness L_{DIP}. Then the values for each film were compared to the roughnesses as determined from the XRR measurements (see Tab. 6.2). As mentioned above, the reflectivity curve of the sample prepared at $T_{substr.} = 136\,°C$ was measured at $T = 80\,°C$ and therefore $a_\perp$ was corrected for the thermal expansion (with $\alpha_\perp = 66.6\times10^{-6}$1/K, as determined in Sec. 8.6).

While the roughness of the 333 Å thick DIP film prepared at $T_{substr.}$=136 °C was around 22.1 Å the sample prepared at $T_{substr.}$=-160 °C had a film thickness of 386 Å and a roughness of about 51.1 Å. The sample prepared at $T_{substr.}$=-90 °C had a film thickness of 410 Å and a comparatively low roughness of 19.5 Å which can already be seen from the less damped thickness oscillations.

Figure 6.11 shows a *log-log* plot of the roughness of DIP (σ) *vs.* the film thickness (L) for samples prepared at different substrate temperatures. The roughnesses for $T_{substr.}$=136°C, -90°C and -160°C are compared to the random deposition limit

as indicated by the dashed line at β=0.5 and to the linear fit (straight line) as extracted from [56] for DIP films prepared at $T_{substr.}$=145 °C and R=12 Å/min. The data from [56] correspond to a growth exponent of β=0.748. For the roughness of the sample prepared at $T_{substr.}$=136 °C a good agreement with the values from [56] of DIP films prepared at $T_{substr.}$=145 °C was found (β=0.748) while the roughness of the sample prepared at $T_{substr.}$=-160 °C was much closer to the random deposition limit and the sample prepared at $T_{substr.}$=-90 °C exhibited a lower roughness as a film of comparable thickness prepared at $T_{substr.}$=145°C.

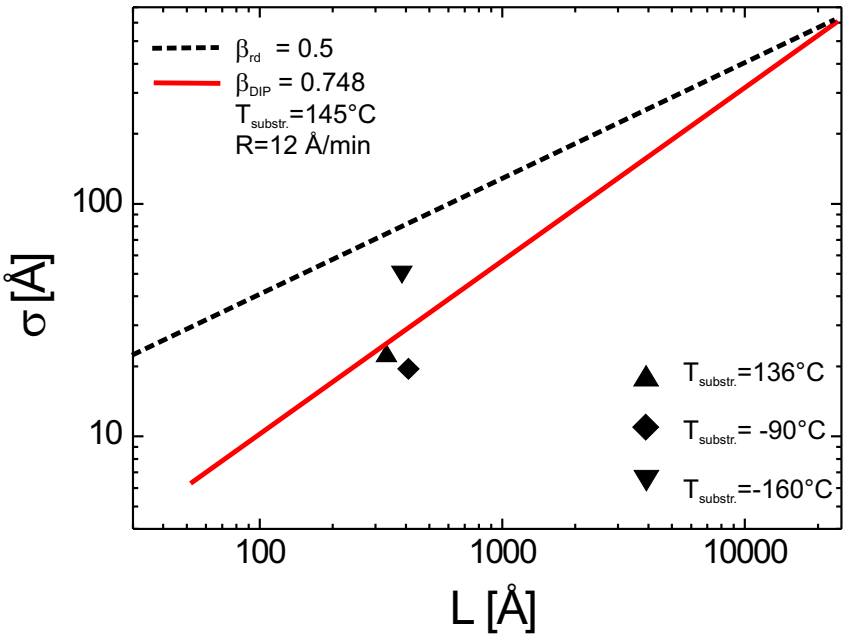

Figure 6.11: *Log-log* plot of the roughness of DIP (σ) *vs.* the film thickness (L) for samples prepared at different substrate temperatures. The data points for $T_{substr.}$=136°C, -90°C and -160°C are compared to the data (the linear fit) from [56] prepared at $T_{substr.}$=145 °C and R=12 Å/min.

6.3.3 Conclusions

From the structure of DIP films prepared at different substrate temperatures it can be concluded that the growth differs strongly depending on the preparation conditions. While films prepared at substrate temperatures close to the desorption temperature of DIP ($\geq$150 °C) exhibit large flat terraces DIP films prepared at low substrate temperatures show a granular surface. Furthermore, DIP films prepared at $T_{substr.}$=136°C have a similar scaling behavior of the roughness with film thickness as films prepared at $T_{substr.}$=145°C. For samples prepared at significantly lower substrate temperatures a different behavior was observed. Due to the influence of the preparation conditions on the film properties further investigations of the growth of DIP films were carried out.

6.4 In-situ real-time growth of DIP on silicon oxide

The structure of as-prepared DIP films on silicon oxide was studied recently as a function of film thickness and preparation conditions [11, 12, 56]. However, these measurements were performed after the deposition of the entire film. Recently, *in-situ* real-time XRD measurements were performed on small conjugated molecules of pentacene [74,180] and perylenetetracarboxylic dianhydride (PTCDA) [181,182] and valuable informations on the growth process could be extracted. Since DIP films deposited on silicon oxide have a high structural order they are well suited to studies of the *in-situ* real-time growth.

6.4.1 X-ray diffraction measurements at the DIP anti-Bragg reflection

The *in-situ* real-time XRD measurements are based on the destructive interference of the scattering of subsequent layers at the anti-Bragg point ($q_z^* = \pi/d_{DIP}$). Therefore, for layer-by-layer growth, the scattered intensity at the anti-Bragg point oscillates as a function of the deposition time.

For organic films with upright standing molecules the anti-Bragg point is in a q_z-region (for DIP, $q_z^* \approx 0.19\,\text{Å}^{-1}$) where the Fresnel-reflectivity is still significant and Kiessig fringes evolving during the film growth may therefore make the interpretation of the scattered intensity more difficult. This can be overcome by measuring at the 3/2-anti-Bragg point, which is accordingly given by, $q_z = 3\pi/d_{DIP}$. For DIP on silicon oxide the Fresnel intensity at this point ($q_z \approx 0.57\,\text{Å}^{-1}$) is rather low which makes the

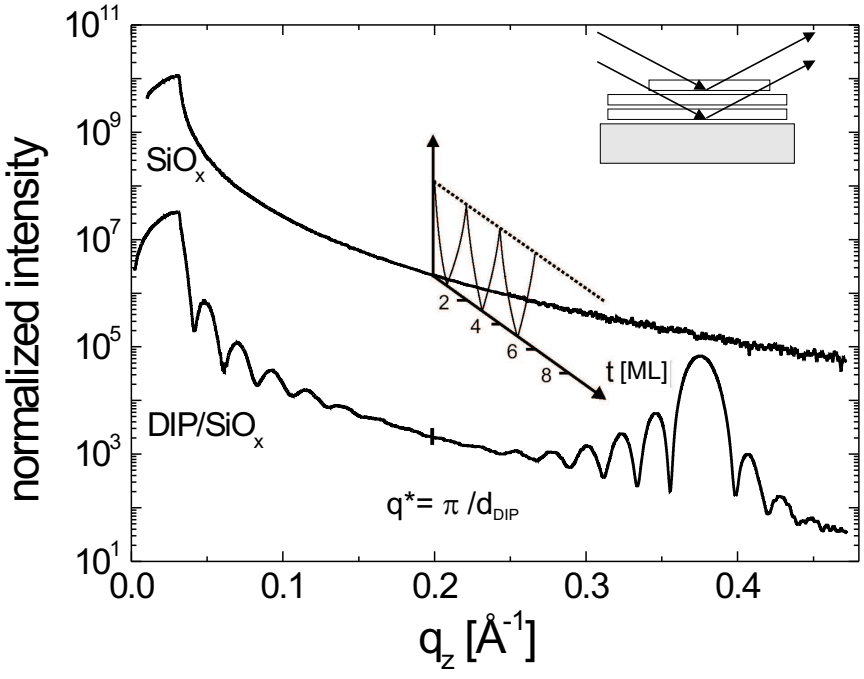

Figure 6.12: Representation of the *in-situ* real-time XRD method. At the anti-Bragg point of the DIP film ($q_z^* = \pi/d_{DIP}$), the scattering of subsequent layers interferes destructively. For layer-by-layer growth, the intensity at the anti-Bragg point oscillates as a function of the deposition time.

use of high-intensity synchrotron X-ray radiation necessary. The measurements were performed at the ESRF, ID10B.

The *in-situ* real-time growth experiments make the use of a portable UHV chamber necessary which can be mounted on standard diffractometer tables. The small chamber has been described in Sec. 5.1.3. Before starting the film deposition a constant deposition rate was adjusted and the incident and detector angles are moved such that they fulfill the 3/2-anti-Bragg condition. The measurements were started/terminated by opening/closing the Knudsen-cell shutter. The scattered intensity at the 3/2-anti-Bragg point is measured as a function of the deposition time which leads to growth oscillations. Deviations of the perfect layer-by-layer growth (*i.e.* island growth) lead to

a damping of the growth oscillations. In case that post-growth reordering effects set in after stopping the deposition, the scattered intensity was still registered for a while after closing the Knudsen-cell shutter.

6.4.2 Results

We have performed *in-situ* real-time growth experiments for DIP at different growth conditions (high substrate temperature/low deposition rate; low substrate temperature/low deposition rate; high substrate temperature/high deposition rate and low substrate temperature/high deposition rate). Figure 6.13 shows the results of these

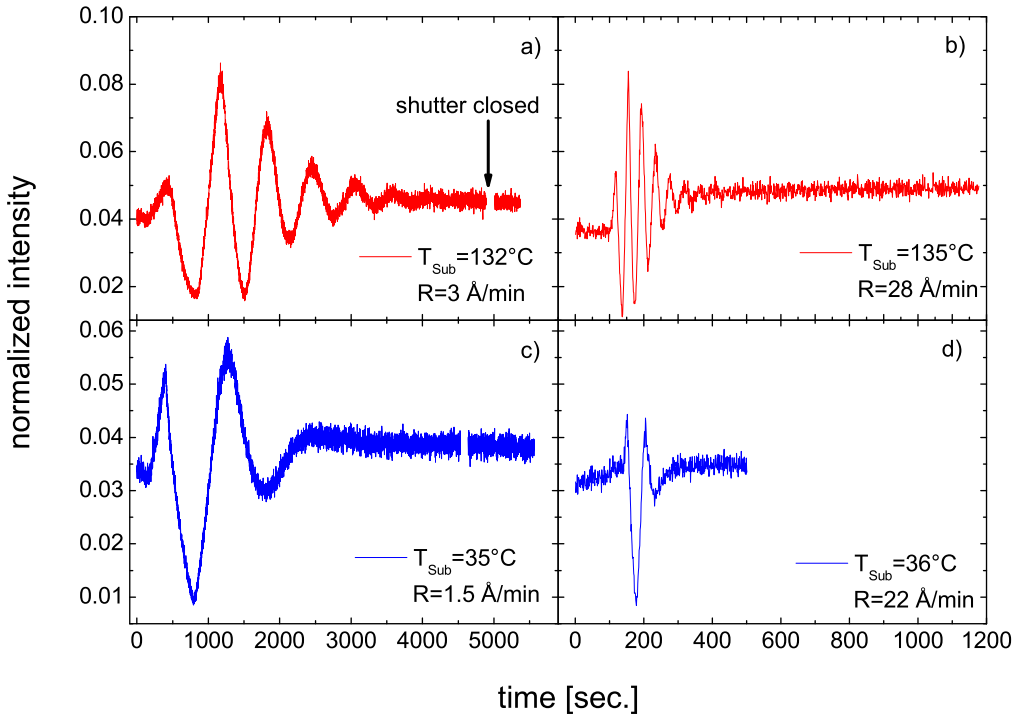

Figure 6.13: *In-situ* real-time growth measurements at the 3/2-anti-Bragg point for four DIP films prepared at different growth conditions, (a) at $T_{sub.} = 132\,°C$ and R=3 Å/min, (b) at $T_{sub.} = 135\,°C$ and $R = 28$ Å/min, (c) at $T_{sub.} = 35\,°C$ and $R = 1.5$ Å/min and (d) at $T_{sub.} = 36\,°C$ and $R = 22$ Å/min.

measurements. The real-time growth of DIP on a silicon wafer at (a) a substrate temperature of $T_{sub.} = 132\,°C$ and a deposition rate of $R = 3\,Å/min$, (b) at $T_{sub.} = 135\,°C$ and $R = 28\,Å/min$, (c) at $T_{sub.} = 35\,°C$ and $R = 1.5\,Å/min$ and (d) at $T_{sub.} = 36\,°C$ and $R = 22\,Å/min$ are displayed.

While the growth oscillations for the films prepared at low substrate temperature damped out already after a few monolayers the films prepared at high substrate temperatures show pronounced growth oscillations up to 13 monolayers. When comparing the *in-situ* real-time growth data for the different deposition parameters the effect of the substrate temperature seems to dominate the effect of the deposition rate. The damping of the growth oscillations at low substrate temperature is due to a relatively strong 3D growth. After four monolayers the growth oscillations rapidly damp out indicating that the DIP film starts to form small islands which incoherently contribute to the scattered signal. After closing the Knudsen-cell shutter the scattered signal was still registered for a while but no changes in intensity could be observed.

The specular XRR data to the corresponding real-time growth curves from Fig. 6.13 are presented in Fig. 6.14(a-d). The measurements were performed at the same substrate temperature as during deposition. The data were fitted using the Parratt formalism and the resulting parameters (film thickness, electron density and roughness) are tabulated in Tab. 6.3.

film	$T_{substr.}$ [°C]	R [Å/min]	L_{DIP} [Å]	ρ_{el} [el./Å^3]	σ [Å]	σ_{RD} [Å]
(a)	132	3.0	276	0.375	20.4	67.7
(b)	135	28.0	440	0.428	41.4	85.5
(c)	35	1.5	173	0.475	43.5	56.0
(d)	36	22.0	189	0.475	43.3	53.6

Table 6.3: Preparation conditions (substrate temperature and deposition rate) and the results of fitting the specular XRR data by the Parratt formalsim. Furthermore, the random deposition limit σ_{RD} is displayed for each film.

In Fig. 6.15 the roughness of the DIP films prepared at different substrate temperatures and deposition rates is displayed in a *log-log* plot versus the film thickness. The data are compared to the random deposition limit σ_{RD} and the data of DIP films

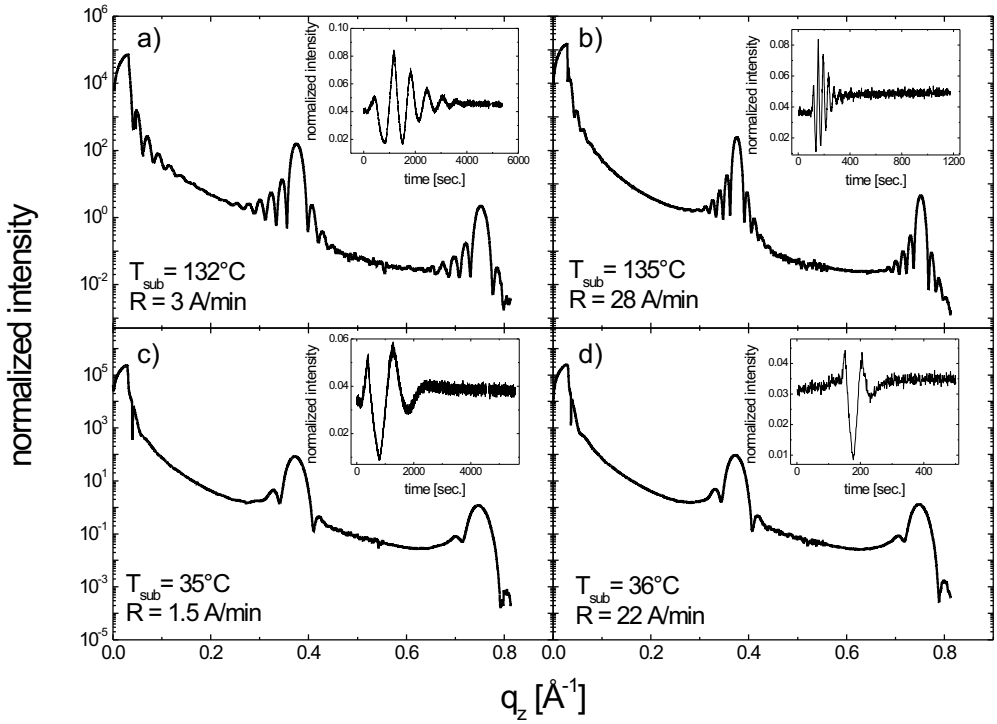

Figure 6.14: Specular X-ray reflectivity measurements of the corresponding *in-situ* real-time measurements of Fig. 6.13 (see insets). (a) and (c) were prepared at high substrate temperature and (b) and (d) at low substrate temperatures.

prepared at $T_{substr.}$=145°C and R_{DIP}=12 Å/min from [56]. Only the data point of the film prepared at $T_{substr.}$=132°C and R_{DIP}=3.0 Å/min fits well to the data with a growth exponent of β=0.748. The other data points ($T_{substr.}$=135°C, R_{DIP}=28 Å/min; $T_{substr.}$=35°C, R_{DIP}=1.5 Å/min and $T_{substr.}$=36°C, R_{DIP}=22 Å/min) have a comparatively higher roughness. The films prepared at low substrate temperatures exhibit a similar roughness behavior independently of the deposition rate while for the films prepared at high substrate temperatures a higher deposition rate has a stronger influence on the film roughness.

The high roughness of the low-substrate temperature films also explains why the Kiessig fringes are mostly damped out. However, all films show well-defined DIP Bragg

reflections with rocking widths in the range of 0.008−0.009 °.

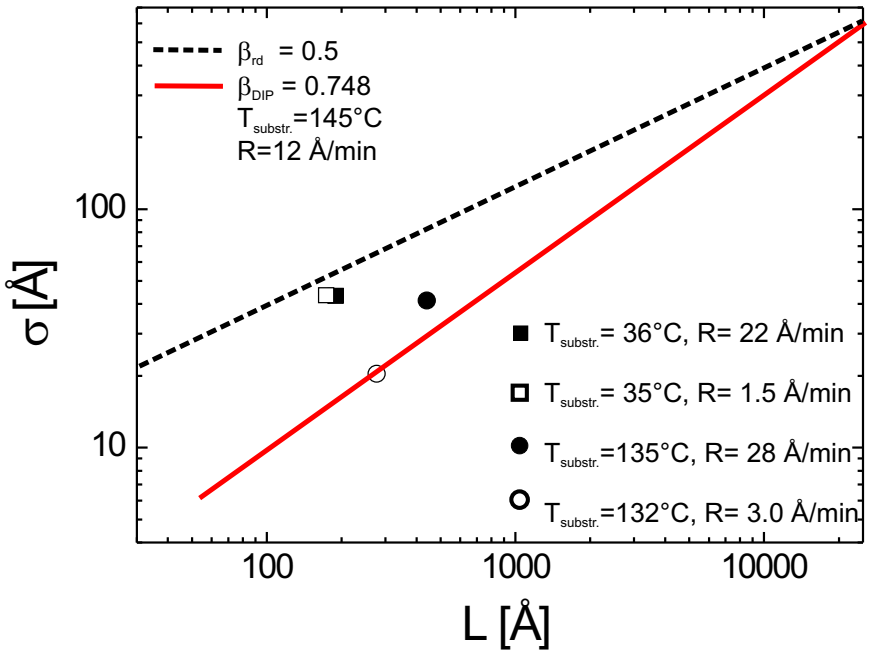

Figure 6.15: *Log-log* plot of the roughness of DIP (σ) *vs.* the film thickness (L) for samples prepared at different substrate temperatures and deposition rates. The 276 Å thick film prepared at $T_{substr.} = 132\,°C$ and with a deposition rate of 3 Å/min had a roughness of 20.4 Å. The film prepared at $T_{substr.} = 135\,°C$ and $R = 28$ Å/min had a thickness of 189 Å and a roughness of 43.4 Å. The film prepared at 35 °C (36 °C) and at a depositon rate of 1.5 Å/min (22 Å/min) had a film thickness of 173 Å (440 Å). These values are compared to the data (the linear fit) from [56] prepared at $T_{substr.} = 145\,°C$ and $R = 12$ Å/min and to the random deposition limit σ_{RD}.

From *in-situ* real-time growth experiments of DIP on silicon oxide and from the comparison with the as-prepared specular XRR data for different deposition conditions we obtained all information for an understanding of the studies of capped films. A detailed description and analysis of *in-situ* real-time data of DIP on silicon oxide (and others) can be found in [183].

6.5 Conclusions

Before studying more complex systems as the aluminum oxide/organic heterostructure we have studied the structure and morphology of thin films of F_{16}CuPc, pentacene and DIP deposited on silicon oxide. The different molecules formed films which exhibited different structural and morphological characteristics. At high substrate temperatures F_{16}CuPc forms crystalline needles, while pentacene and DIP form large flat terraces. All molecules were standing upright on silicon oxide and showed the effect of preferential dewetting. DIP forms highly crystalline films and compared to pentacene no additional phases were observed in the studied range of film thicknesses and preparation conditions. For the DIP film growth the substrate temperature and the deposition rate were varied and it turned out that the films prepared at low substrate temperatures had a different structure from those prepared at high substrate temperatures. Nevertheless, DIP forms highly crystalline films over a wide range of preparation conditions. We could also show that valuable informations can be obtained from *in-situ* real-time XRD measurements at the 3/2-anti-Bragg condition. Combining the different techniques of specular XRR, *in-situ* real-time XRD, and AFM helps to understand the complex film growth and structures of organic films.

7 Inorganic-on-organic heterostructures

In the previous chapter thin films of organic semiconductors have been studied. In the present chapter we focus on more complex inorganic/organic heterostructures which are relevant for the application in organic electronics. When inorganic materials are deposited on top of organic films penetration of the inorganic material into the organic film is a known problem [25, 26]. Therefore, the preparation of such inorganic/organic hybrid systems with well-defined interfaces and the conservation of the organic film structure is of major interest.

Gold is widely used as a contact material for OFETs. When deposited on top of the organic film (top-contact) gold may diffuse into the semiconducting film and affect its structure and electrical properties. Therefore, studies of the growth of gold on films of organic semiconductors are necessary to improve the injection of charge carriers from the gold contacts into the organic film.

Due to its extraordinary electrical, mechanical and optical properties aluminum oxide is a potential material for insulating layers and the encapsulation of organic devices. For such applications a well-defined character of the interface structure of Al_2O_3/DIP is important. It is highly desirable that the organic film structure is not affected by the impact of the sputtering process. Therefore, the structure of sputtered aluminum oxide films, its interface with the organic film and the organic film structure have to be investigated. With the collected knowledge of the structure of the Al_2O_3/DIP hybrid system, we can then focus on the thermal stability (Chapter 8) of such systems.

This chapter is organized as follows. In Sec. 7.1 the deposition of gold on DIP films is studied. Section 7.2 is devoted to the characterization of aluminum oxide films sputtered on silicon wafers. The aim is to prepare aluminum oxide films in a controlled way. Such aluminum oxide films are then sputtered on DIP films and the structure of such hybrid systems is studied in Sec. 7.3. In Sec. 7.4 the roughness evolution of aluminum oxide films deposited on silicon oxide and on DIP films is discussed.

7.1 Deposition of gold on DIP films

The optimum preparation conditions under which diffusion of gold into the organic film are minimized were investigated by Dürr *et al.* [25, 51]. Briefly, when high deposition rates and low substrate temperatures are used the penetration of gold clusters into the organic film is reduced. High deposition rates favor the formation of large clusters which at low substrate temperatures cannot diffuse into the organic substrate.

Here, the results of *in-situ* real-time X-ray diffraction measurements of the deposition of gold on top of DIP films are presented. When depositing a gold film on top of an organic film we expect the following features to change:

- the total reflection edge depending on the electron density, $\alpha_c \approx \lambda\sqrt{r_e \rho_{el}/\pi}$,
- the Kiessig interference fringes due to the additional gold layer (different electron density contrast, $\Delta\rho$),
- the interface roughness due to possible diffusion of gold into the organic film,
- the DIP Bragg peak, due to a possible destruction of the organic film structure caused by the penetration of gold into the organic film.

Two possible scenarios resulting on the deposition of gold on the organic film are sketched in Fig. 7.1. For the application in organic electronics a well-defined interface between the gold and the DIP film is desired. However, if diffusion of gold into the organic film occurs the electron density profile should change accordingly.

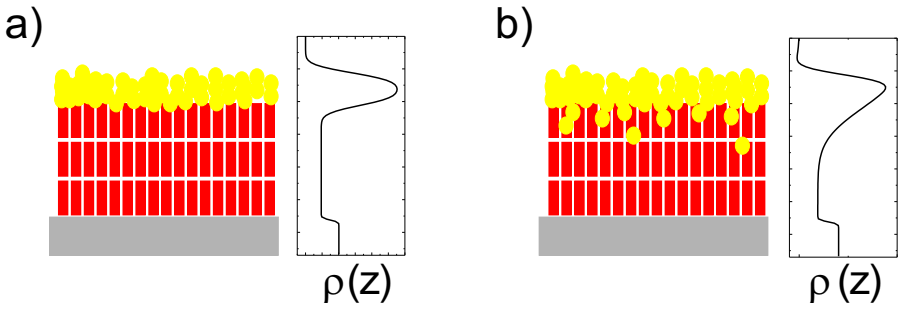

Figure 7.1: Possible scenarios for the deposition of gold on DIP films. Well-defined gold/organic interface (a) versus enhanced penetration of Au into the organic film (b) can be seen in the electron density profile, ρ(z) (here, simulation).

The measurements were performed at the beamline ID10B at the ESRF. For the deposition and *in-situ* investigations the portable UHV chamber as described in Sec. 5.1.3 was used. The chamber therefore had to be equipped with an e-beam evaporator for the evaporation of gold.

During the deposition of gold X-ray reflectivity scans including the first order DIP Bragg reflection were performed several times. Each scan lasted for ca. 14 min which means that the deposition rate had to be low enough to minimize changes in the reflectivity curve during the scans.

7.1.1 In-situ real-time investigations of gold deposition on DIP films

The gold film was deposited on top of DIP/SiO_x prepared in the same UHV chamber before. The DIP film was prepared on a Si(100) wafer with a native oxide layer at a substrate temperature of $T_{substr.,DIP} = 135.5\,°C$ and at a deposition rate of $R_{DIP} = 45.7\,Å/min$ ($P = 2.5 \times 10^{-7}$ mbar). For the preparation of the gold film the substrate was cooled down to $T_{substr.,Au} = 18\,°C$ to reduce potential diffusion of gold clusters. At a very low deposition rate of approximately $R_{Au} = 0.025\,Å/min$ the pressure during gold deposition was $P = 2 \times 10^{-8}$ mbar. Figure 7.2 shows *in-situ* real-time X-ray reflectivity measurements of the deposition of gold on DIP films (on silicon oxide).

The different curves represent different time steps of the deposition and are offset for clarity. Only small variations between the different curves could be observed. From fitting the data by the Parratt formalism the following results were obtained. Several models were tested. A fitting model which included a gold layer on top of the DIP film (Au/DIP/SiO_x/Si) resulted in unphysically low gold film thicknesses ($\ll 1$ Å) and also the electron density of the gold film was in the range of the one of DIP. Therefore, the reflectivity curves were fitted by a model containing no separate gold film (DIP*/SiO_x/Si). The results are displayed in Tab. 7.1. With increasing deposition time the thickness of the DIP film slightly increased, the electron density increased and also the roughness increased slightly. The first order DIP Bragg reflection also does not change significantly. The integrated DIP Bragg intensity (a measure for the crystallinity of the film) changes less than 1 % indicating that the crystalline structure of the DIP film was not affected by the deposition of gold. Also, the position of the Bragg peak did not change (see Fig. 7.2(b)).

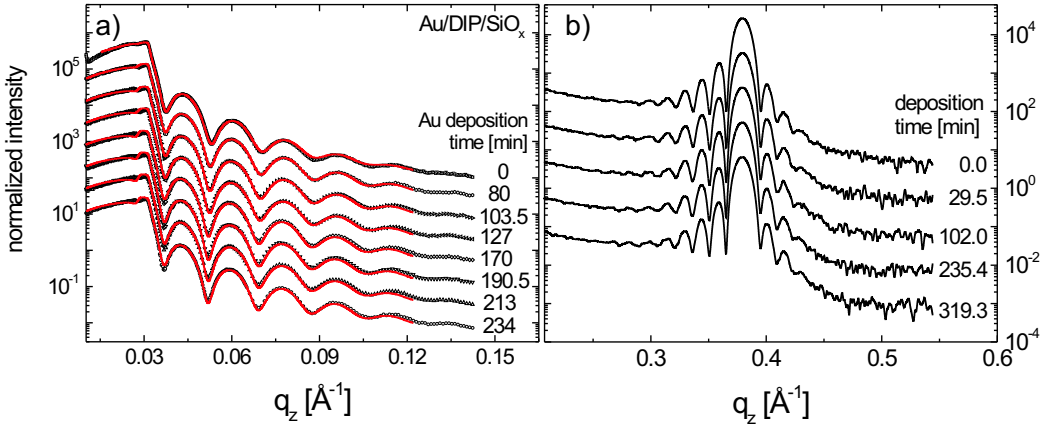

Figure 7.2: Specular X-ray reflectivity data for different time steps of the deposition of gold on DIP. Only small variations are visible upon deposition of gold in both the specular path (a) and in the first order DIP Bragg reflection (b). The substrate temperature was $T_{substr.} = 18\,°C$ and the pressure during deposition was $P = 2 \times 10^{-8}$ mbar.

7.1.2 Conclusions

The fact that a fitting model of the type Au/DIP/SiO$_x$/Si did not fit the data indicates that no gold film developed on the DIP surface. Even for a discontinuous gold film no satisfying results could be obtained. The only model which showed reasonable fits was based on the assumption that no gold film has formed on top of the DIP surface and that the gold diffused directly into the organic film increasing its electron density slightly. One of the reasons why no continuous gold film has formed on the organic film could be due to the low deposition rate and due to a substrate temperature of 18 °C which was relatively high compared to -120 °C as proposed by Dürr *et al.* [31]. As mentioned above, the depostion rate was only about 0.025 Å/min (during 338 min) so that the total amount of gold evaporated was very low. On the one hand this was due to the scanning time of 14 min which did not allow for high deposition rates and on the other hand due to technical constraints of the experimental apparatus (evaporator). Only low evaporation rates (a few Ångströms within several hours) could be achieved. Thus, the measurements lasted for several hours and only small amounts of gold were evaporated on the organic film. Therefore, the formation of large gold clusters on the

time [min]	L_{DIP} [Å]	ρ_{DIP} [el/Å^3]	σ_{DIP} [Å]	q_{Bragg} [Å^{-1}]	int. intensity
0	434.2	0.378	35.7	0.379	1
29.5	435.1	0.382	35.5	0.379	0.994
102.0	437.3	0.388	36.45	0.379	1.005
235.4	442.2	0.420	38.0	0.379	0.990
319.3	440.8	0.411	37.2	0.379	0.993

Table 7.1: Fitting results from the deposition of gold on top of DIP films. A fitting model considering a continuous gold layer on top of the DIP film was not successful.

organic surface was very unlikely and small gold clusters or atoms diffused directly into the organic film. Small amounts of gold which are well distributed over the entire thickness of the organic film do not give rise to a notable change in the scattered signal. Therefore, only minor changes could be observed. Scharnberg *et al.* [26] have investigated the diffusion of silver into films of DIP by the radio-tracer technique and they found small amounts of silver which diffused directly to the organic/silicon oxide interface. This is to some extend consistend with our picture that small amounts of gold can diffuse directly into the organic film.

7.2 Characterization of sputter-deposited aluminum oxide films

In this section aluminum oxide films deposited on silicon substrates by r.f. magnetron sputtering were studied. In Sec. 7.3 such sputtered aluminum oxide films will be deposited on top of organic films. But to understand the film structure of this complexe inorganic/organic heterostructure we first have to understand the morphology and structure of the aluminum oxide films deposited on the relatively smooth silicon oxide surface compared to the rather rough surfaces of the organic films.

Here, we studied the aluminum oxide film structure and morphology for different film thicknesses and for different sputtering parameters. The stoichiometry is investigated by means of RBS measurements where the Al/O ratio and the Ar content could be determined.

7.2.1 Surface characterization of sputtered aluminum oxide films on silicon oxide

The details of the r.f. magnetron sputtering of aluminum oxide films are described in Sec. 5.1.4. After the sputtering process the topography of the aluminum oxide films was investigated by contact mode AFM in the UHV system. The samples therefore had to be transferred in air from the dedicated sputtering chamber to the UHV system. Figure 7.3 shows a typical AFM image of a sputtered aluminum oxide film on silicon oxide with a profile scan of the sample topography. The surface roughness in this scan range of the 116 Å thick film was about 1.5 Å.

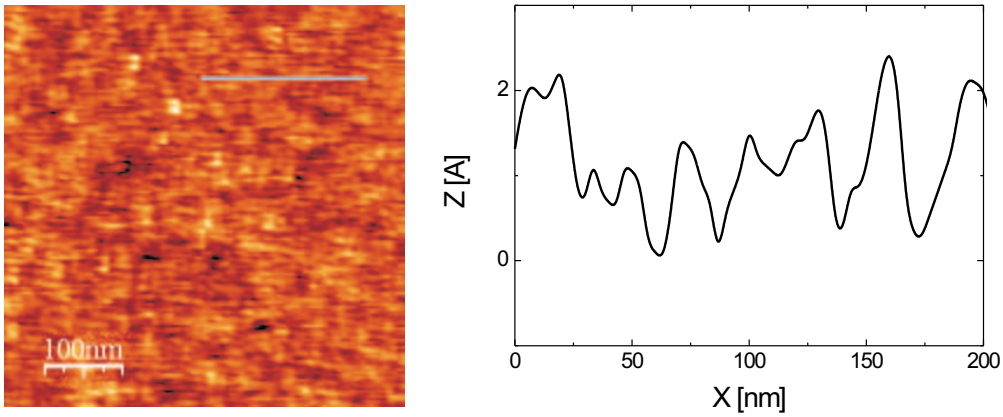

Figure 7.3: Topographical AFM image (c.m.) of an aluminum oxide film on a silicon oxide substrate.

The film surface is relatively smooth and exhibits a granular morphology with a mean distance of its grains of about 14.5 nm. The surface topography is columnar as expected from the ratio $T_S/T_M < 0.1$ which corresponds to the zone 1 on Thornton's structure model (see Sec. 4.3.3) where T_S is the substrate temperature (ca. 18 °C) and T_M is the melting point of aluminum oxide (around 2050 °C).

For the analysis of the surface-chemical composition Auger electron spectroscopy (AES) was performed [184]. Despite the problems with quantification in AES [185] the technique can in principle produce data about approximate surface composition

analyses.

If AES is applied on insulating or semiconducting crystals with small heating conductivity, one must be aware that a finely focused electron beam of several keV energy and current densities of up to 50 μA per mm^2 often will induce severe damages on the illuminated area of the surface. However, most AES studies simply use the Auger spectrum as a fingerprint of the chemical composition and several studies can also be found for aluminum oxide films [186, 187]. Figure 7.4 shows AES data of an aluminum oxide film on a silicon wafer. AES investigations of the aluminum oxide film reveal that there

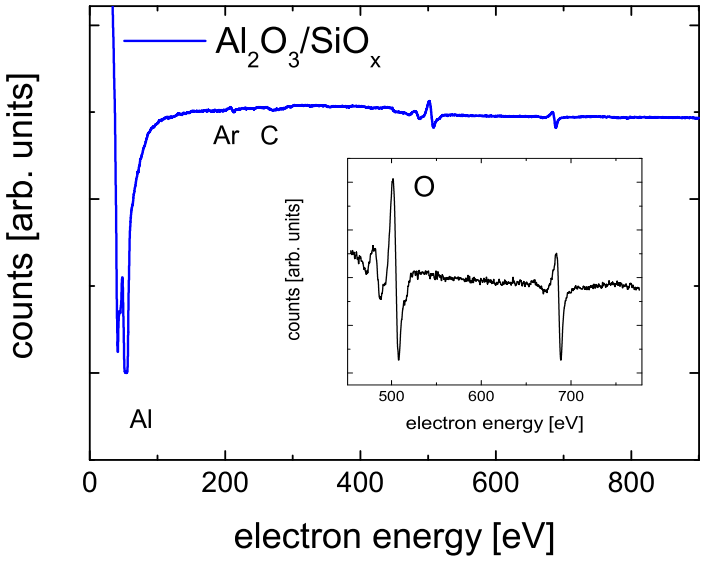

Figure 7.4: AES spectrum in the differentiated mode of an aluminum oxide film on a silicon substrate. The Auger line at 51 eV corresponds to oxidized aluminum and the line at 508 eV can be assigned to oxygen. Some weak lines at 212 eV and 271 eV correspond to argon and carbon, respectively.

is no sign of a neutral metallic Al LVV Auger peak at a kinetic energy of 68 eV. The only aluminum peak which was seen corresponds to the Al^{3+}(L)-O^{2-}VV transition at 51 eV characteristic for aluminum oxide. Furthermore, the O KLL line at 508 eV was observed and weaker lines at 212 eV and 271 eV which are due to argon and carbon, respectively. However, the escape depth of Auger electrons is only a few Ångströms and

therefore the information on the composition of the aluminum oxide layer is restricted to the oxide surface.

7.2.2 Structure of aluminum oxide films on silicon oxide

Aluminum oxide films of thicknesses ranging from ca. 116 Å to 6000 Å were prepared on silicon wafers and their structure was studied by X-ray diffraction. The experimental data of X-ray reflectivity measurements and corresponding fits by the Parratt formalism are displayed in Fig. 7.5. The X-ray reflectivity curves are offset for clarity. The true specular signal was obtained by subtracting the offspecular diffuse signal from the measured intensity.

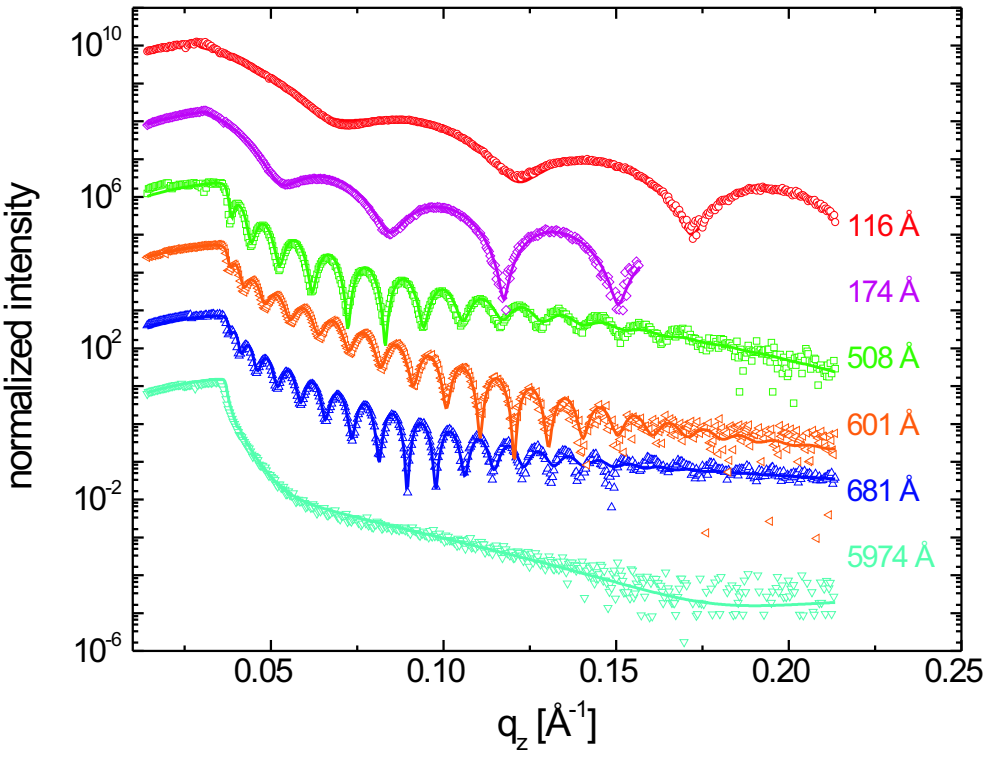

Figure 7.5: Specular X-ray reflectivities of sputtered aluminum oxide layers of different film thickness on silicon oxide substrates (starting with the thinnest layer from top).

The corresponding results from the fitting procedure are tabulated in Tab. 7.2 together with the sputtering parameters and the RBS data (see below). The argon partial pressure during sputtering was 1×10^{-2} mbar for these samples.

sample	L [Å]	ρ_{el} [el/Å^3]	σ [Å]	P [W]	T$_{sub}$ [°C]	Al:O	Ar [%]
1	508	0.942	18.6	150	18.5–18.7	2:3.32	0.37
2	681	0.984	18.9	200		2:2.55	0.63
3	1212*			150	18.7–19.4	2:2.76	0.83
4	5974	0.973	45.5	150	19.4	2:3.2	0.59
5	174	0.908	11.6	150	19.8	2:3.30	0.75
6	601	0.956	16.7	150		2:3.20	0.52
7	116	0.937	10.6	120		2:3.80	0.85

Table 7.2: Sputtering parameters and RBS results for aluminum oxide on silicon oxide samples. The deposition rate was always between 5–10 Å/min. *nominal thickness.

The specular X-ray reflectivity curves show pronounced thickness oscillations (Kiessig fringes) from which the aluminum oxide thickness can be determined. For all films, no signature for crystalline aluminum oxide could be found at higher scattering angles (*i.e.* at the position of Bragg reflections of α-Al_2O_3 the strongest of which are at $q_z = 2.46\,\text{Å}^{-1}$ and $q_z = 3.01\,\text{Å}^{-1}$).

From the specular X-ray reflectivity data the electron densities could be determined for the different aluminum oxide films. The film density strongly influences the film properties and generally, the density of metal and dielectric films increases with the film thickness and asymptotically approaches the bulk value [188]. In Fig. 7.6 the electron densities of aluminum oxide films (sputtered at 150 W) as determined from fits of the Parratt formalism to the X-ray reflectivity data are plotted as a function of film thickness.

The data points $\rho(L)$ approach a value of $\rho_0 = 0.978\,\text{el.}/\text{Å}^3$ which is about 82% of the 'bulk' electron density of crystalline Al_2O_3 ($1.193\,\text{el.}/\text{Å}^3$). Depending on the sputter conditions sputtered films may exhibit a porous structure which could explain the relatively low electron density compared to the value of crystalline aluminum oxide.

The evolution of the aluminum oxide film roughness as a function of the film thickness

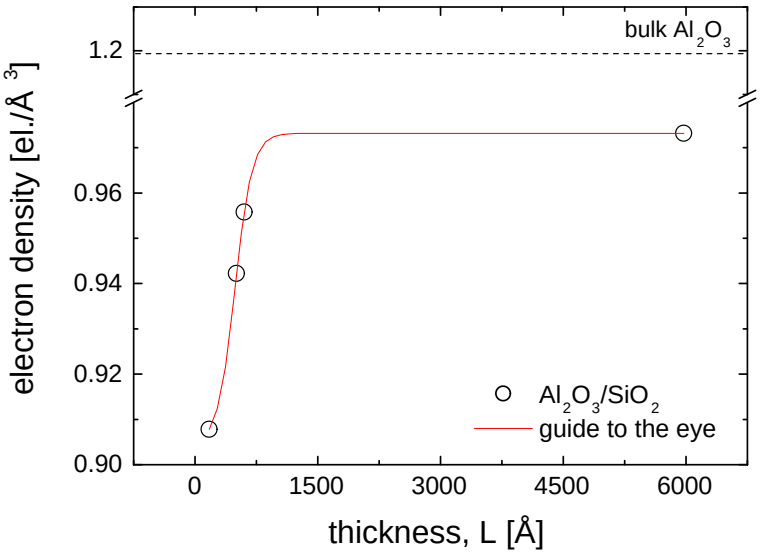

Figure 7.6: Electron density of aluminum oxide as a function of the film thickness as determined from least square fits to the specular X-ray reflectivity data of aluminum oxide films on silicon oxide. The broken line indicates the bulk density.

will be discussed in Sec. 7.4 in comparison with aluminum oxide films deposited on DIP films.

7.2.3 Chemical composition of the aluminum oxide layers

The stoichiometry of the aluminum oxide layer and incorporation of argon in the capping layer plays an important role for the intrinsic mechanical stress [189] and for the electrical breakdown [139] of the films. Cavities with Ar in the aluminum oxide film usually lead to stress in the film [189, 190] and can also influence the mechanical properties of the capping layer at elevated temperatures. Thus, the stoichiometry and the Ar content of the aluminum oxide films were determined by Rutherford backscattering spectroscopy (RBS) [191]. The measurements were carried out with He^+ ions of 1 MeV at the Dynamitron in Stuttgart. The RBS-chamber had an IBM-geometry (*i.e.*, the detector was located at a $\theta = 165\,^\circ$ scattering angle in the same plane defined by the beam and the normal to the sample) with a detector resolution of 14 keV FWHM. The

data were analyzed with the software RUMP.[1]

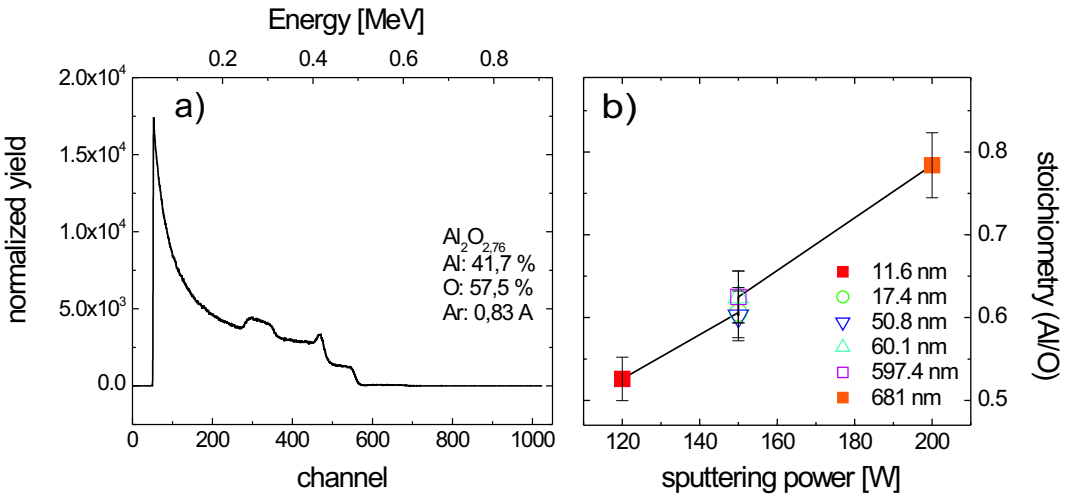

Figure 7.7: (a) Typical Rutherford backscattering spectrum of a sputter deposited aluminum oxide film on a silicon oxide substrate. (b) Stoichiometry (Al/O ratio) as a function of the sputtering power.

Figure 7.7(a) shows typical RBS data for a 120 nm thick aluminum oxide film on a silicon oxide surface. The Al/O ratio of our samples ranged between 0.625 and 0.905 and thus from oxygen rich to metal rich films and the Ar content was found between 0.59 and 4.00 % depending on the preparation conditions. The values for the other capping layers deposited on silicon wafers are tabulated in Tab. 7.2. Figure 7.7(b) shows the influence of the sputtering power on the stoichiometry of the sample. With increasing sputtering power the aluminum oxide films tended to become more rich in aluminum. A similar behavior for r.f. magnetron sputtered films was reported by Cueff *et al.* [148] and they also reported an increasing density with increasing r.f. sputtering power. Dense microstructures also have higher compressive stresses [148].

[1] Rutherford Backscattering Spectroscopy analysis package based on Gnuplot, this package provides comprehensive analysis and simulation of RBS and ERD spectra.

7.2.4 Conclusions

We have prepared aluminum oxide films on silicon oxide substrates by means of r.f. magnetron sputtering from a pure aluminum oxide target in a pure Ar atmosphere. The surface characterization of the sputtered aluminum oxide films showed a granular morphology and from AES measurements some impurities of argon and carbon could be detected. The electron density of the aluminum oxide films was around 82% of the bulk value of Al_2O_3. The Al/O ratio of the films ranged between 0.625 and 0.905 and a tendency for more metal rich films at higher sputtering powers was found.

In conclusion, we are able to prepare aluminum oxide films in a controlled way. Nevertheless, the structure and morphology of aluminum oxide films deposited on a flat silicon substrate might differ strongly from a film deposited on top of an organic film which exhibits large terraces or islands and thus a rather rough surface. The characterization of aluminum oxide films deposited on organic films will be discussed in the following.

7.3 DIP films capped by aluminum oxide layers

A capping layer obviously has to form a closed layer to function as a barrier. In the previous section aluminum oxide films were prepared on silicon oxide substrates to characterize the sputtering parameters and the film structure and morphology. However, the aim of this work was to prepare aluminum oxide films on top of organic films and to characterize their film structure. The preceeding studies help to understand the aluminum oxide film structure when deposited on a well-defined and 'hard' (silicon oxide) surface which might differ significantly from its film structure when deposited on the relatively rough and 'soft' surface of an organic film. From the deposition of metal films on top of organic films it was shown that diffusion of the metal into the organic film is a major concern in the film preparation [25, 26, 31].

In this section the structure and morphology of sputtered aluminum oxide films deposited on top of DIP films are discussed. With AFM measurements we compare the topographical changes before and after the sputtering process. A major concern of the deposition of an aluminum oxide film on top of a rather 'soft' organic film was the impact of the sputtering process on the penetration of aluminum oxide into the organic film or how much the organic film was destroyed by the impinging aluminum and oxy-

gen atoms. This was investigated by X-ray diffraction measurements performed before and after the sputtering process. Furthermore, cross-sectional TEM images supplied a real-space image of the aluminum oxide/DIP interface and thus a direct information of possible diffusion of aluminum oxide clusters into the organic film.

7.3.1 Surface morphology of aluminum oxide on DIP films

The structure and morphology of DIP films on silicon oxide has been described in Sec. 6.3. After the sputtering process the sample topography was studied in UHV with an AFM in contact mode in a different chamber. Figure 7.8 compares contact AFM images taken before and after the deposition of the aluminum oxide film on top of the DIP film.

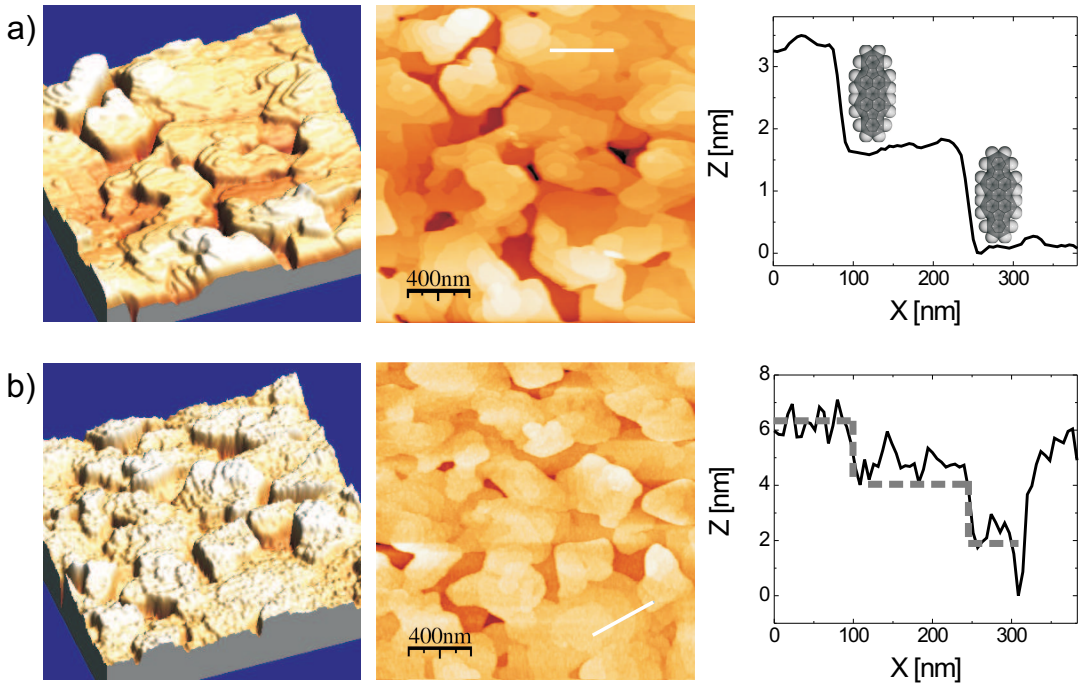

Figure 7.8: AFM (c.m.) images (3D, 2D and profile scan) of a DIP sample before (a) and after (b) deposition of the aluminum oxide layer. The aluminum oxide layer exhibits a granular morphology covering the terraced DIP structure.

The first conclusion which can be drawn is that the terraced DIP structure can still be recognized after depositing the aluminum oxide on top of the DIP film. A closer

look on the morphology of the aluminum oxide layer exhibits a granular morphology of the aluminum oxide which still reflects the main features of the underlying organic film topography (terraces), see the profile scans along the lines in Figs. 7.8(a) and (b).

A more detailed analysis of the AFM data shows that the aluminum oxide grains have an elongated shape with an anisotropic orientation (Fig. 7.9).

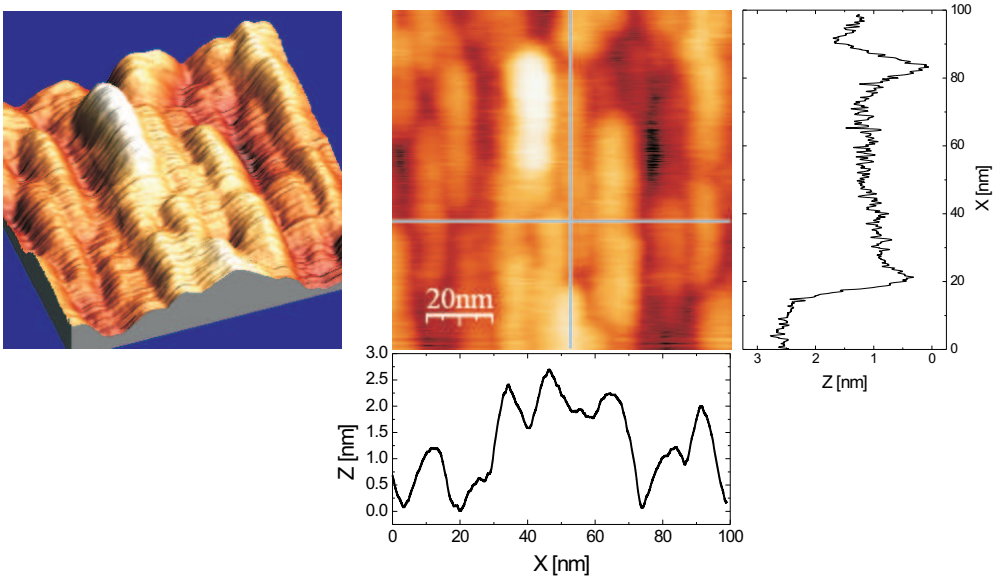

Figure 7.9: Close-up AFM (c.m.) images (3D, 2D and profile scans) of a DIP film capped with an aluminium oxide layer. The aluminum oxide film exhibits grains of elongated structure.

The length to width ratio is about 3. This lengthy shape does not seem to be induced by the scanning AFM tip since when changing the fast scan direction by 90 ° the same topography was obtained.

7.3.2 Structure of aluminum oxide on DIP films

The structure of the as-prepared DIP films capped with an aluminum oxide film was investigated by X-ray diffraction measurements. X-ray diffraction techniques are particularly powerful for destructive-free studies of the structure of buried interfaces.

Specular and offspecular X-ray scattering

In Fig. 7.10 the specular and diffuse offspecular reflectivity curves for two samples with aluminum oxide capping layers of 174 Å and 508 Å are plotted (the curves are offset for clarity). Additionally, the specular reflectivity curves of the corresponding reference samples with aluminum oxide on silicon oxide are displayed.

The specular reflectivity curves of the capped DIP films show the Kiessig fringes resulting from the interference of the X-rays reflected at the air/Al_2O_3, Al_2O_3/DIP, DIP/SiO_x and SiO_x/Si interfaces. The roughness of these interfaces leads to the damping of the oscillations.

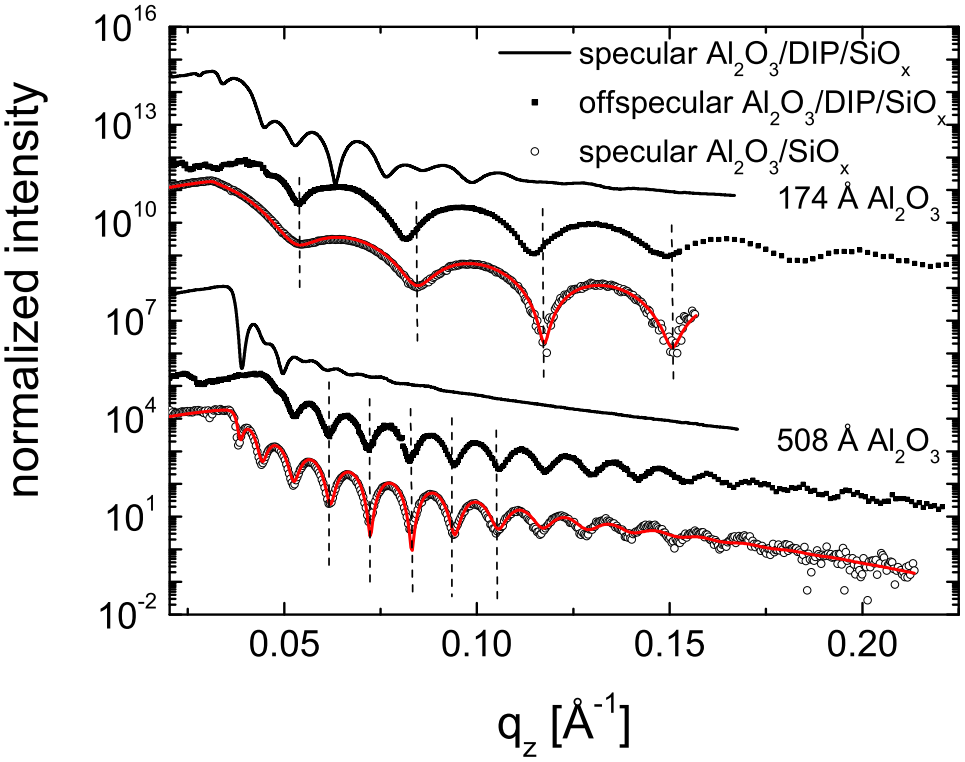

Figure 7.10: Specular and diffuse offspecular X-ray reflectivity scans of Al_2O_3/DIP films compared to specular scans of Al_2O_3/SiO_x samples. The diffuse offspecular scans allow for the determination of the Al_2O_3 film thickness.

The diffuse scattering was measured in a specular geometry with an offset angle of 0.05 °. Compared to the specular scattering signal the thickness oscillations remain much more pronounced at higher scattering angles. The specular path has different contributions from the Al_2O_3, the DIP and the substrate each with different rocking widths. Thus, in the offspecular regime the signal can still be sensitive to the aluminum oxide film which has a broader rocking width and therefore the thickness oscillations of the aluminum oxide film can be accessed directly.

When compared to the specular signal of the reference samples (Al_2O_3/SiO_x) a rather good agreement of the thickness oscillations can be observed.

Impact of the sputtering process on the organic film structure

As mentioned above a well-defined interface between the aluminum oxide and the organic film is crucial for many applications of such heterostructures. With X-ray diffraction this interface can be investigated and from the Bragg reflection of the organic film the impact of the sputtering process on the organic film structure can be clearified.

Figure 7.11(a) shows the specular X-ray reflectivity curves of DIP samples before and after the deposition of aluminum oxide for two films sputtered at different sputtering powers. The pronounced thickness oscillations (Kiessig interferences) which could be observed before and after the sputtering process indicated that the interfaces were well-defined. From the Laue oscillations around the DIP Bragg reflection (Fig. 7.11(b)) the coherent thickness can be determined. For sputtering powers of 150 and 200 W (*Leybold Univex 350* with *AJA International sputtering unit*) a small decrease in the coherent thickness corresponding to 1–2 MLs of DIP could be observed whereas for sputtering in a different machine (*Edwards Auto 306*) and with a sputtering power of only 65 W no changes could be observed.

Summarizing the fitting results, the interfacial width of Al_2O_3/DIP does not differ significantly from the bare DIP surface roughness before sputtering which implies that aluminum oxide does not diffuse remarkably into the DIP film upon sputtering.

The coherent thickness of the DIP film remains constant for a sputtering power of 65 W and decreases about 1–2 MLs for sputtering powers of 120–200 W which means that apart from the first 1–2 top most monolayers the DIP film structure remains coherently ordered.

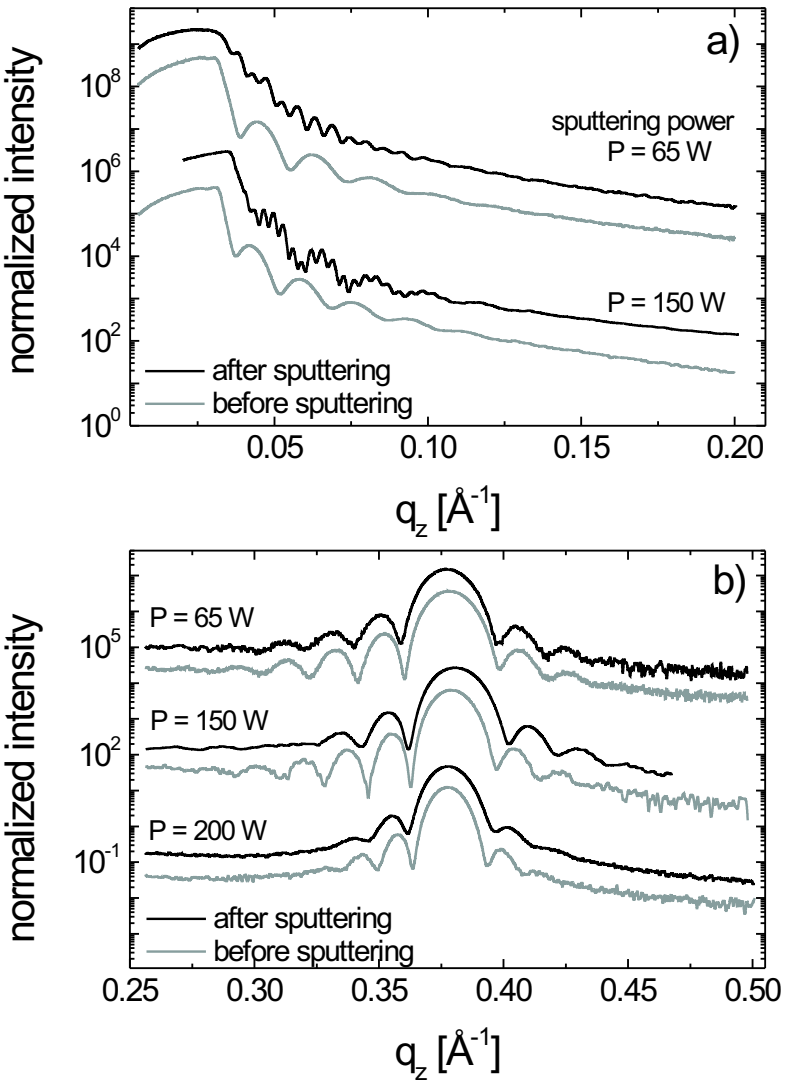

Figure 7.11: Specular X-ray reflectivity (a) and 1st order DIP Bragg reflection (b) before and after the deposition of aluminum oxide with different sputtering powers. The pronounced thickness oscillations in (a) indicate a well-defined interface between aluminum oxide and the DIP film. For a sputtering power of 65 W no changes in the Laue oscillations around the DIP Bragg reflection (b) can be observed whereas for higher sputtering powers a small decrease in the coherent thickness can be observed.

7.3.3 Aluminum oxide/DIP interface

From the X-ray diffraction data no significant increase of the roughness of the Al_2O_3/DIP interface was observed and thus only little diffusion of aluminum oxide into the DIP film would be expected. To obtain a real-space image of the aluminum oxide/DIP heterostructure cross-sectional TEM measurements were performed. A typical TEM image of a DIP film capped with an aluminum oxide layer is shown in Fig. 7.12(a).

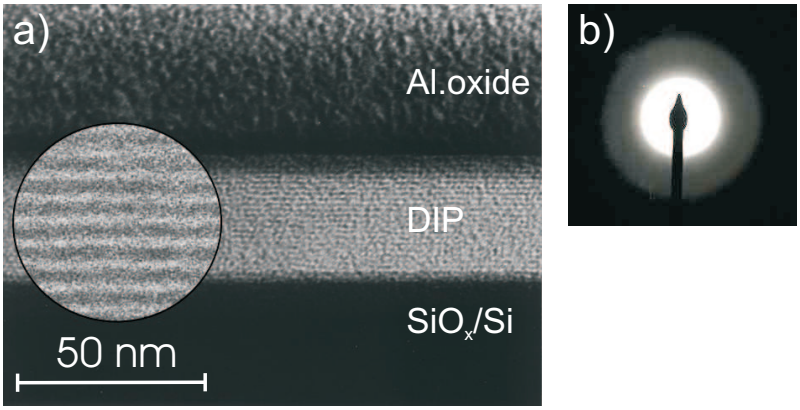

Figure 7.12: (a) Cross-sectional TEM image showing a laterally well-defined interface of the Al_2O_3/DIP heterostructure. Even individual molecular layers of DIP can be resolved. (b) The electron diffraction image shows that the Al_2O_3 film is completely amorphous.

It shows a laterally well-defined interface of the Al_2O_3/DIP heterostructure. No significant penetration of aluminum oxide into the organic film on this length scale can be observed. Within the organic film even individual molecular layers of DIP could be resolved which confirms the high crystallinity of the DIP film. The electron diffraction image (Fig. 7.12(b)) confirms the X-ray data which did not show any signature for crystalline aluminum oxide. The electron diffraction was performed on the aluminum oxide film and shows a diffuse diffraction ring which indicates that the film is completely amorphous.

A more detailed analysis of a TEM specimen is shown in Fig. 7.13 where the density profile across the different interfaces of the sample is shown. To distinct the amorphous signature from the periodic signature of the molecular planes of DIP a laterally averaged profile (within the lines indicated in Fig. 7.13) was taken.

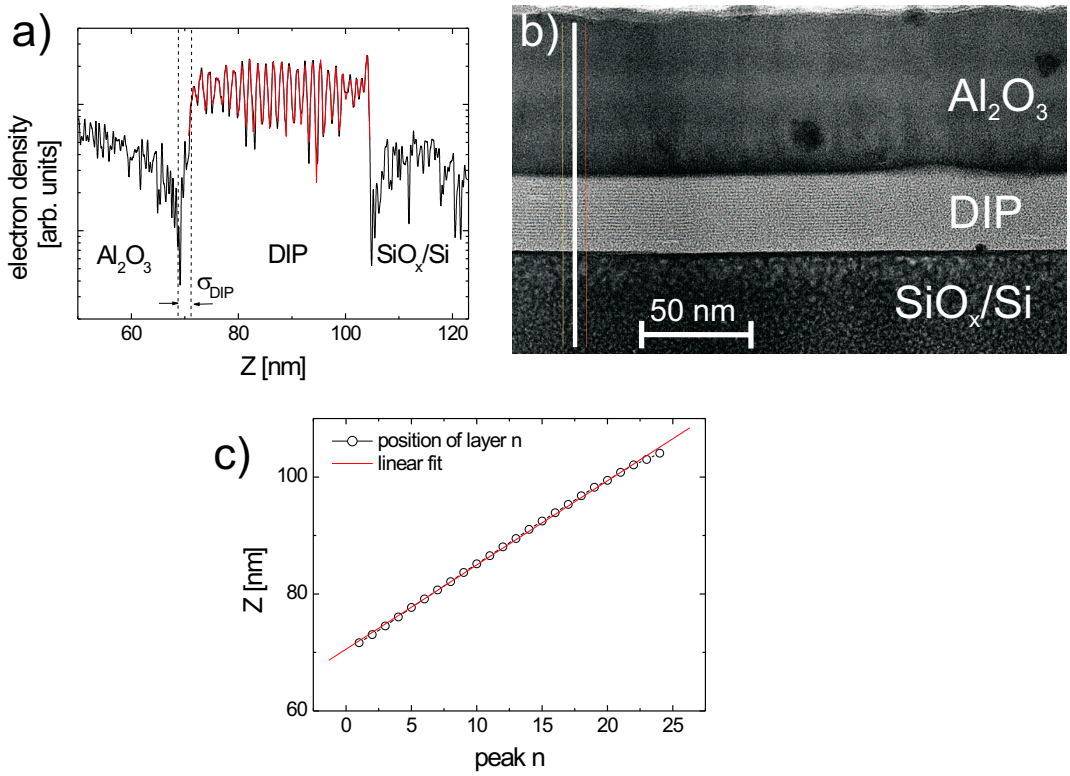

Figure 7.13: Electron density profile (a) across the TEM image of the aluminum oxide/DIP heterostructure (b). (c) The individual molecular planes of DIP are equidistant.

The periodic arrangement of the DIP lattice planes were fitted by a series of Gaussians the position of which are equidistant as shown in Fig. 7.13(c). However, a linear fit to the data results in a lattice plane distance of ca. 14.4 Å which is significantly smaller than the value obtained from X-ray diffraction and AFM data (ca. 16.5 Å). Thus, the lattice plane distance might not be determined with sufficient accuracy from the TEM images.

The interface roughnesses can also be estimated from the profile scan. For the DIP/SiO_x interface a roughness of 0.3–0.4 nm and for the Al_2O_3/DIP interface a roughness of ca. 2.6 nm could be determined which is in agreement with values determined from X-ray diffraction measurements on similar samples.

7.3.4 Conclusions

In this section, we studied the structure and morphology of as-prepared aluminum oxide films deposited on organic films.

The totally amorphous aluminum oxide films consist of small grains covering the typically terraced DIP structure. Finally, the DIP films capped with an aluminum oxide layer form a well-defined heterostructure. The DIP film is still highly crystalline and the interface with the aluminum oxide is laterally well-defined. No significant penetration of aluminum oxide into the organic film could be observed. Therefore, this system is very well suited for studies of the thermal stability.

7.4 Roughness evolution of sputtered aluminum oxide films on organic and inorganic substrates

Thin film devices have received growing importance in different fields of applications such as microelectronics, optics and coating technology. An important thin film material in different fields is aluminum oxide due to its extraordinary mechanical, electrical and optical properties. The growth process of such films presents a fundamental challenge, but has also a direct impact on device performances such as the breakthrough voltage in organic field-effect transistors [192].

Therefore, one critical parameter is the evolution of the film roughness, σ, with film thickness, L, (Fig. 7.14). In the theory of growth processes in condensed matter scaling theories for the surface morphology and dynamics of a growing film are a very successful concept [116,177,178]. In a dynamic scaling regime the root mean square (rms) surface roughness σ of a film scales with the film thickness L, [193–195]

$$\sigma = L^{\beta}, \tag{7.1}$$

where the growth exponent β depends on the mechanism of the film growth, and a constant deposition rate is assumed. In random deposition [193] (rd) there is no spatial or temporal correlation between the deposited particles (the extreme kinetic limit) and $\beta = 0.5$. For growth processes as described by the Kardar, Parisi, Zhang universality class [195], interface growth parallel to the surface plane is allowed and $\beta = 1/3$ is obtained in 1+1 dimensions. For 2+1 dimensional systems, the value for β varies for

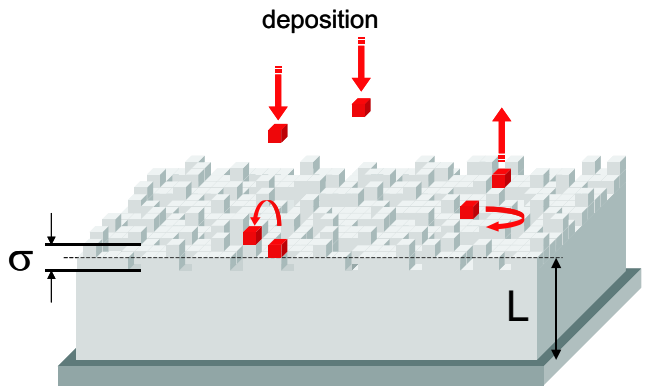

Figure 7.14: Schematic representation of film growth processes. Different processes such as the adsorption, the surface diffusion and the re-desorption of adsorbates have an influence on the evolution of the film roughness σ.

different theoretical models [193, 195–197]. Experimental studies show that depending on the deposition method and on the materials $0.2 \leq \beta \leq 1$. [56, 198–203].

In this section we compare the growth of radio frequency (r.f.) magnetron sputtered aluminum oxide films deposited on two very different surfaces, namely silicon oxide and films of the organic semiconductor diindenoperylene (DIP). Using two complementary techniques, atomic force microscopy (AFM) and X-ray diffraction (XRD), both the surface morphology and the roughness evolution was determined. The growth exponent for sputtered aluminum oxide films deposited on silicon oxide and organic substrates could be determined.

7.4.1 Surface morphology of Al_2O_3/SiO_x and Al_2O_3/DIP - AFM

After the sputtering process the surface morphology of the aluminum oxide films was investigated by contact mode AFM. Figure 7.15(a) shows a typical image of a sputtered aluminum oxide film on silicon oxide with a line scan of the sample topography. The relatively smooth film surface exhibits a granular morphology with a mean distance of its grains of about 14.5 nm (see Sec. 7.2). For thicker aluminum oxide films on silicon oxide a similar morphology was found.

Figure 7.15(b) shows an AFM image of a 681 Å thick aluminum oxide film deposited under similar sputtering conditions on top of a DIP film. The inset shows a contact mode AFM image of an uncapped DIP film with its characteristic topography with

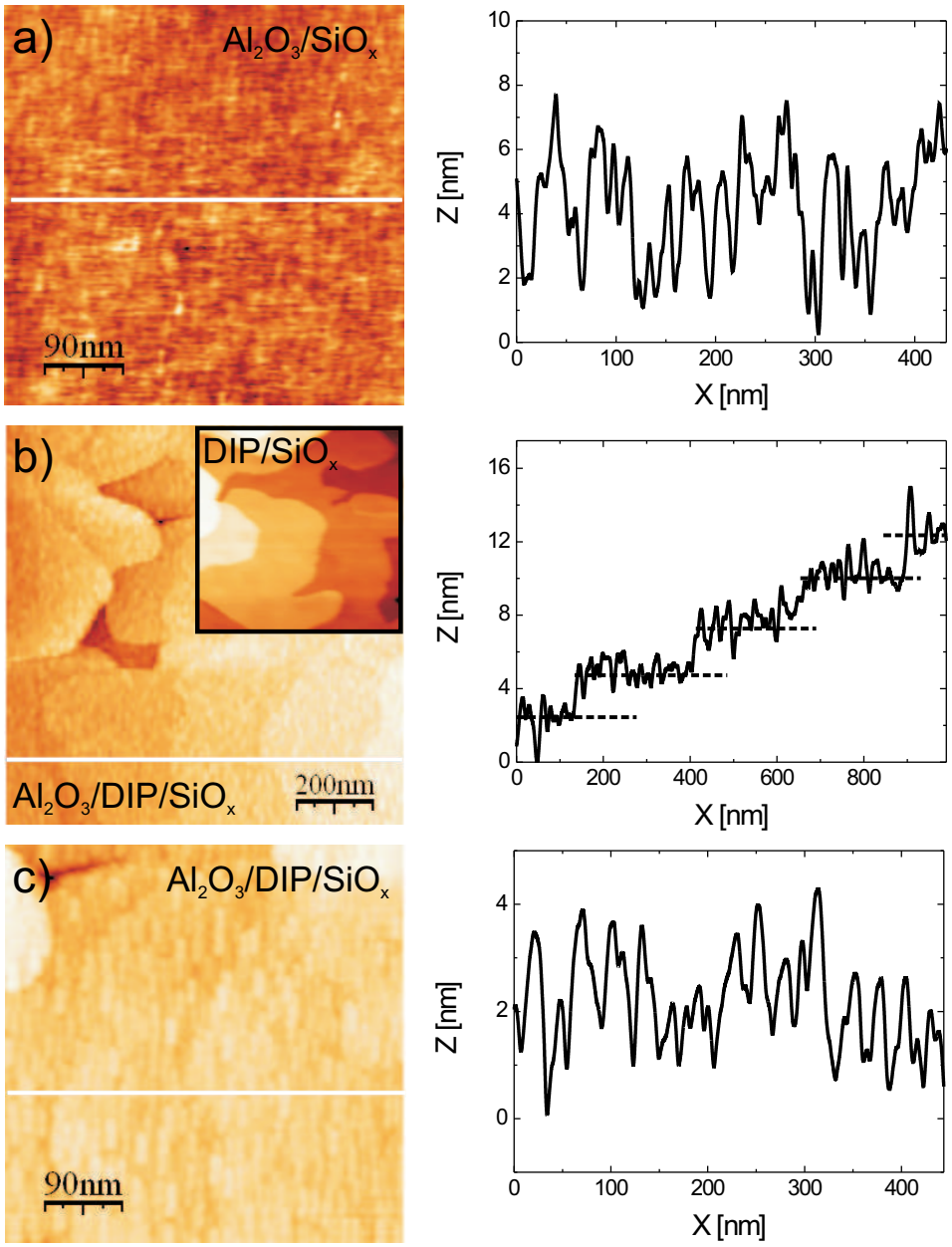

Figure 7.15: Topographical AFM image (c.m.) with line scans of an aluminum oxide film deposited on (a) silicon oxide and (b) DIP. The inset in (b) shows the typical topography of the organic film before aluminum oxide sputtering. (c) AFM image of the morphology of aluminum oxide on a single DIP terrace.

terraces of monomolecular (ca. 16.5 Å) step height [12]. The corresponding line scan reveals the surface morphology of aluminum oxide/DIP.

For the Al_2O_3/DIP system (Fig. 7.15(b)) the terraced structure of the underlying DIP film can still be recognized which implies that the Al_2O_3 surface roughness exhibits a certain degree of correlation with the DIP surface roughness. A closer look at the morphology of the aluminum oxide layer on a DIP terrace (Fig. 7.15(c)) exhibits a granular structure as could already be seen on the Al_2O_3/SiO_x system (Fig. 7.15(a)). The aluminum oxide film thus reflects some features of the underlying substrates - the relatively flat native silicon oxide and the terraced DIP - in addition to its 'inherent' graininess.

7.4.2 Roughness evolution of Al_2O_3/SiO_x and Al_2O_3/DIP - X-ray scattering

The structure of the as-prepared aluminum oxide films deposited on silicon wafers and on DIP films was investigated by X-ray scattering, as discussed in Sec. 7.2 and Sec. 7.3, respectively. Aluminum oxide films of thicknesses ranging from ca. 116 Å to 6000 Å were prepared on both substrates and their out-of-plane structure was studied by X-ray reflectivity.

The experimental data of X-ray reflectivity measurements and fits using the Parratt formalism [165] are displayed in Fig. 7.16(a) for Al_2O_3/SiO_x and in Fig. 7.16(b) for Al_2O_3/DIP. The X-ray reflectivity curves are offset for clarity. The specular signal was obtained by subtracting the off-specular diffuse signal from the measured intensity.

The specular X-ray reflectivity curves show pronounced thickness oscillations (Kiessig fringes) indicating well-defined interfaces (in terms of interface roughness). From the fitting of the X-ray data the film thickness, the electron density and the film-substrate roughness as well as the film surface roughness could be determined [165](see below).

7.4.3 Analysis and Discussion

Aluminum oxide on SiO_x

In Fig. 7.17 the roughness evolution of sputtered aluminum oxide films deposited on silicon oxide is displayed in a $log - log$ plot as a function of the film thickness (filled circles). The slope of a linear fit to the data corresponds to a growth exponent of $\beta = 0.37 \pm 0.03$.

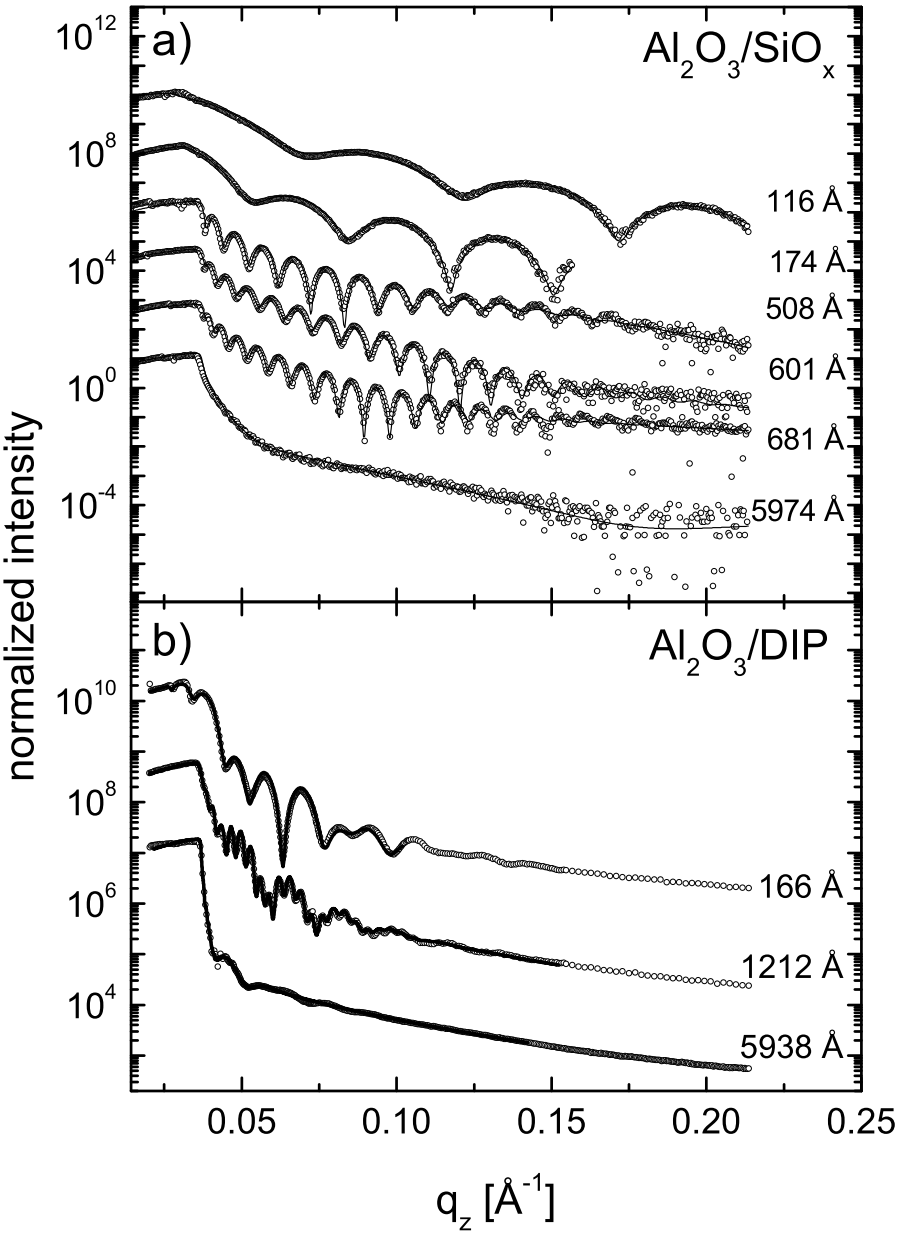

Figure 7.16: X-ray reflectivities of sputtered aluminum oxide layers of different thickness on silicon oxide substrates (a) and on DIP films (b).

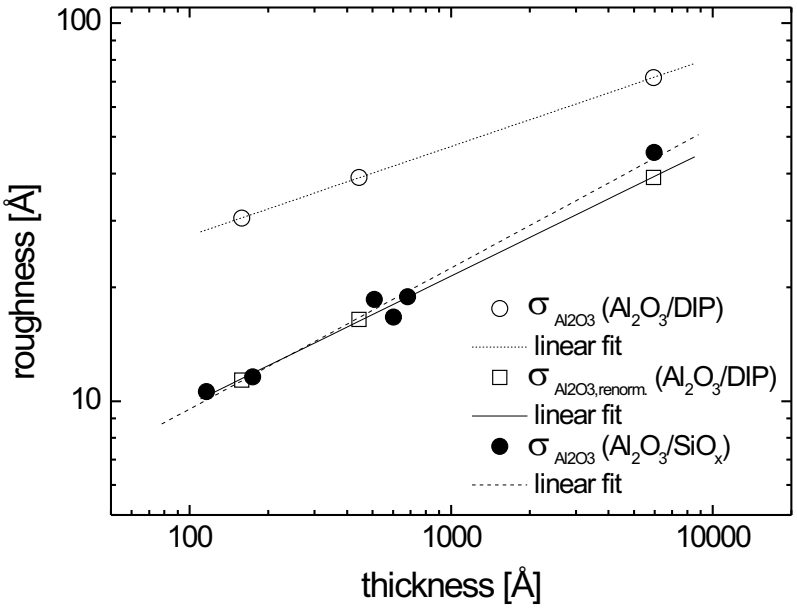

Figure 7.17: Roughness $\sigma_{Al_2O_3}$ for Al_2O_3/DIP (open circles) and renormalized roughness $\sigma_{Al_2O_3,renorm.}$ for Al_2O_3/DIP (filled circles) compared to the roughness $\sigma_{Al_2O_3}$ of the Al_2O_3/SiO_x system (open squares). The scaling behavior of aluminum oxide layers deposited on DIP and on SiO_x are in good agreement.

Experimental studies of the growth exponent β yield different results. For thermal evaporation of Fe [198, 199] and Ag [200] a scaling exponent of $\beta \approx 0.25$ was obtained while for sputter-deposited Au films $\beta = 0.40$ (at 300 K) and $\beta = 0.42$ (at 200 K) [201] and for sputtered Mo films $\beta = 0.42$ was obtained [202].

The various β-values indicate that for different materials and deposition techniques different surface relaxation processes are dominating and the corresponding theoretical models have to be modified accordingly.

Aluminum oxide on DIP/SiO_x

The roughness of aluminum oxide films of different thickness deposited on top of DIP films (of similar thickness of ca. 350 Å) is also plotted in Fig. 7.17 (open circles) and,

at first glance, a growth exponent of $\beta = 0.25 \pm 0.02$ would be extracted. However, considering the large roughness of the substrate (the DIP film) of ca. 25 Å this would be misleading.

For many systems prepared by different deposition methods the imperfection of a given layer is transferred fully or partly to the subsequent layers [204]. Following the approach of Holý, Pietsch and Baumbach [161] in which the effect of vertical correlations between the interfaces has been included, the roughness of the Al_2O_3 film has to be 'renormalized' by the rms roughness of the underlying DIP film, according to the relation

$$\sigma_{Alox,renorm.} = \sqrt{\sigma_{Alox}^2 - \sigma_{DIP}^2} \tag{7.2}$$

In Fig. 7.17 the aluminum oxide roughness renormalized by the DIP roughness is shown, and a scaling exponent of $\beta = 0.34 \pm 0.03$ is extracted. This value is remarkably similar to the scaling exponent determined for the Al_2O_3/SiO_x system. With the similar morphology of aluminum oxide on silicon oxide substrates (Fig. 7.15(a)) and on a single terrace of DIP (Fig. 7.15(c)), it appears that the growth and structure of the aluminum oxide films is similar on both kinds of substrates.

We should point out here that at least in the initial stage $\sigma_{DIP} \gg \sigma_{Alox,renorm.}$, *i.e.* that the 'starting roughness' provided by DIP is the dominating contribution to the aluminum oxide roughness. Therefore, since the DIP has a pronounced and well-developed terrace structure, it is clear that on top of a given terrace we find that the aluminum oxide film has a small local roughness ($\sigma_{Alox,renorm.}$) as obtained by the renormalization whereas the 'global', *i.e.* overall roughness of aluminum oxide has the 'terrace-to-terrace' contribution from the DIP roughness as an 'offset'. Therefore, at least for not too thick films, the renormalization procedure appears to be a sensible approach.

We note that after the aluminum oxide sputtering process no significant decomposition of the crystalline structure of the DIP substrate (except for the topmost one or two monolayers) was observed. [15]

The remarkable observation is the similarity in β despite the very different chemical nature of the two substrates. We emphasize that this β value arises under the present specific sputtering conditions employed in this study, but is not expected to be universal. We rather expect it to change with sputtering power, geometry, argon gas pressure and other experimental parameters.

7.4.4 Conclusions

We have studied the structure and morphology of aluminum oxide films deposited on silicon oxide and organic films of DIP. From the analysis of the X-ray reflectivity measurements we found a growth exponent of $\beta = 0.37 \pm 0.03$ for aluminum oxide films on silicon oxide [13].

The growth exponent β was also determined for sputter deposited aluminum oxide films on DIP films. The simple renormalization approach of Eq. 7.2 works remarkably well. After re-normalizing $\sigma_{Al_2O_3}$ in the Al_2O_3/DIP system a similar β-exponent of 0.34 as for the Al_2O_3/SiO_x system ($\beta = 0.37$) was obtained [13]. The similar growth exponents β and the AFM images of the Al_2O_3/SiO_x and Al_2O_3/DIP systems suggest that the growth and structure of aluminum oxide on these very different substrates exhibits similarities.

7.5 Summary

In this chapter we could show that diffusion of gold into an organic film can be a significant problem for inorganic/organic heterostructures if the preparation conditions are not optimized. In contrast to gold, for sputtered aluminum oxide films deposited on top of DIP films no significant diffusion was observed under the preparation conditions used.

After a detailed investigation of the aluminum oxide film structure resulting from deposition on silicon oxide under different preparation conditions we were able to prepare aluminum oxide films in a controlled way. From studies of the aluminum oxide film roughness we could determine a growth exponent of $\beta = 0.37$ for aluminum oxide deposited on silicon oxide and of $\beta = 0.34$ for aluminum oxide deposited on DIP films. These values allow for the estimation of the aluminum oxide film roughness as a function of the film thickness on both substrates. Astonishingly, the growth exponents β and the AFM images of the Al_2O_3/SiO_x and Al_2O_3/DIP systems are similar which suggest that the growth and structure of aluminum oxide on these very different substrates exhibits similarities.

The DIP films capped with an aluminum oxide layer form a well-defined heterostructure. The DIP film is still highly crystalline and the interface with the aluminum oxide is laterally well-defined. No significant penetration of aluminum oxide into the organic

film could be observed. Therefore, this system is very well suited for studies of the thermal stability.

8 Thermal stability of Aluminum oxide/DIP heterostructures

In Chapter 2 the motivation for the encapsulation of organic devices has been stressed and we have shown in the previous chapter that aluminum oxide is a good candidate for the use as a capping layer. The good gas barrier properties of aluminum oxide have already been proven [143, 148].

The structure and film morphology of organic films and of aluminum oxide films deposited on silicon wafers has been characterized in the previous chapters and it turned out that the Al_2O_3/DIP/SiO_x sandwich structure exhibits well-defined interfaces and especially the in-plane and out-of-plane structure of the DIP films were not affected significantly by the sputtering process.

For the application in organic electronics the thermal stability of such organic-inorganic heterostructures is crucial to guarantee the long-term performance under working conditions. Therefore, the thermal stability of organic films capped with an aluminum oxide capping layer is studied in this section.

The following questions are to be addressed:

- How stable is the Al_2O_3/DIP system in terms of diffusion at the initially well-defined interfaces and in terms of the DIP film structure?

- For the Au/DIP system DIP started to desorb above T = 155 °C in a laterally inhomogeneous process and an enhanced diffusion of Au into the organic film was observed [25,57]. Given that aluminum oxide is much less mobile at these temperatures, is it possible to stabilize the Al_2O_3/DIP structure beyond the desorption temperature of the uncapped DIP films (T > 190 °C)?

- What is the microscopic mechanism leading to the eventual breakdown of the inorganic/organic heterostructure?

To address these questions the following techniques were applied. The desorption of DIP molecules for capped and uncapped films was investigated by thermal desorption spectroscopy (TDS). The morphology of the aluminum oxide surface was studied with AFM after heating to elevated temperatures and cooling down the samples for the measurements. The structure and the interfaces of the heterostructures were studied *in-situ* by means of X-ray diffraction measurements as well as the crystallinity of the organic film. With TEM a real-space image of the samples after heat treatment was obtained. Optical microscopy was used to study the surface of the samples after annealing.

8.1 Thermal desorption of uncapped and capped DIP films

The overall thermal stability of DIP films with and without aluminum oxide capping layer was investigated with thermal desorption spectroscopy (TDS) measurements. TDS allows for the determination of bonding energies of adsorbed molecules on a substrate and for the desorption kinetics. Herefore, the adsorbed layer is heated in a controlled manner and the desorption products are detected with a mass spectrometer tuned to the respective e/m ratio and thus the number of desorbed molecules can be determined as a function of temperature.

We studied the influence of different heating rates and different capping layer thicknesses on the thermal stability of the system. The TDS measurements were done by S. Meyer and J. Pflaum at the University of Stuttgart.

8.1.1 Experimental details

The TDS measurements were performed in a dedicated UHV chamber equipped with a quadrupol mass spectrometer from Balzers. The whole temperature programed desorption process is controlled by a PC which registers the desorption rate and controles the temperature ramp. A thermoelement couple was attached close to the substrate and the whole setup was calibrated beforehand. The desorbed molecules are registered in the mass spectrometer. Herefore, an electron beam ionizes the molecules which then are separated by their masses in the quadrupol mass filter. For DIP films the mass spectrometer is tuned to the mass of the single and double ionized DIP molecule (400 amu and 200 amu, respectively). The background signal was registered at 300 amu.

For the TDS measurements the sample preparation was modified to prevent desorption from the edges where the encapsulation might not be guaranteed. A perfect encapsulation of the DIP film could be achieved by using a hole mask during the organic film preparation (see Fig. 8.1(a)) and then the aluminum oxide was sputtered on the whole sample as is indicated in Fig. 8.1(b).

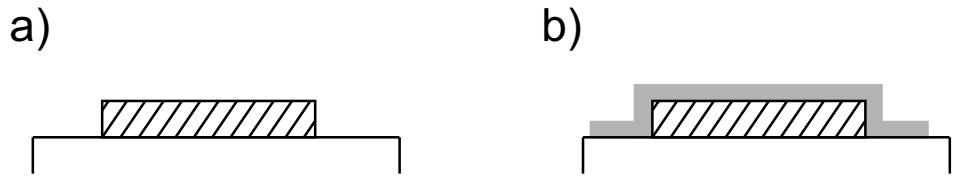

Figure 8.1: Preparation of TDS samples to avoid desorption of DIP from the edges. Herefore, the DIP film was deposited through a shadow mask only in the middle of the substrate (a) and the aluminum oxide was sputtered on the whole substrate (b).

8.1.2 Results

Figure 8.2 shows TDS data for an uncapped DIP film and two capped DIP films ramped with different heating rates of 10 °C/min and 30 °C/min, respectively. The two capped DIP films were similar with respect to the DIP and the aluminum oxide film thickness and the sputtering parameters were comparable, thus, the aluminum oxide films also had comparable morphology and stoichiometry.

The uncapped DIP film has a well-defined desorption peak around 190 °C which originates from DIP 'bulk' desorption[1] while the desorption peaks for the capped DIP films are shifted to higher temperatures and have different features. The uncapped film shows a sharp TDS peak while the films capped with an aluminum oxide layer have an extended desorption spectrum with multiple features as an evidence for the different desorption process. A decrease of the heating rate from 30 °C/min to 10 °C/min shifts the center of mass of the desorption spectrum from 293 °C to 328 °C.

We also performed TDS measurements for capped DIP films (of comparable thickness) with aluminum oxide layers of different thickness heated at the same heating rate of 5 °C/min (see Fig. 8.3). For these measurements we used samples which were not

[1] The order m of the desorption process can be estimated from fitting rate equations to the desorption curve. From the shape of the TDS data the order of the desorption process should be rather small (0–2/3).

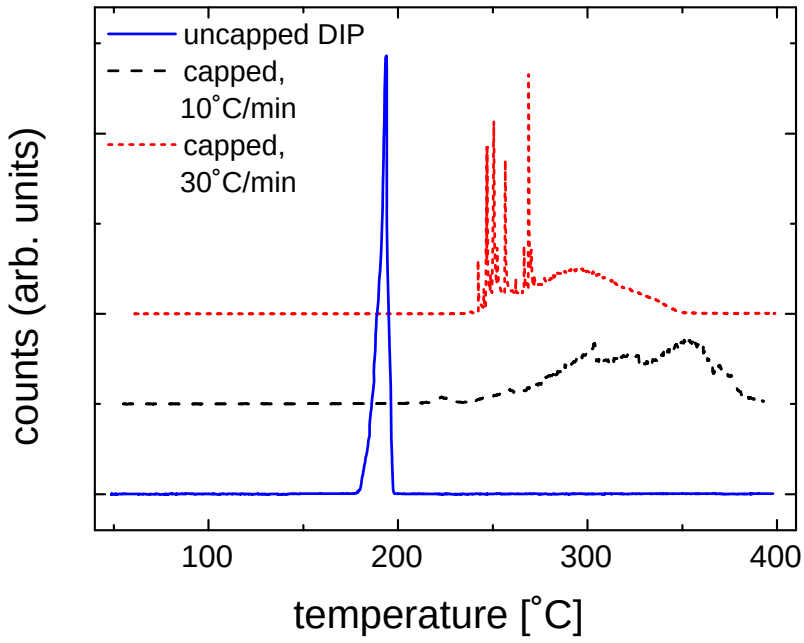

Figure 8.2: Thermal desorption spectra of an uncapped and capped DIP films. The well defined desorption peak of the uncapped DIP film at 190 °C has to be compared to the desorption spectra of the capped films. Besides a shift to higher desorption temperatures of the capped films (depending on the heating rate) the desorption process differs essentially from that of the uncapped film [TDS measurements were performed in collaboration with S. Meyer].

prepared with a hole mask as described above (Fig. 8.1(b)). The DIP films covered the whole substrate and the aluminum oxide film was deposited on top. The results of these measurements are again compared to the uncapped DIP film.

The DIP film with the thinnest Al_2O_3 capping layer (185 Å) has its desorption peak around 290 °C. For the other samples no dominating effect of the capping layer thickness can be observed but all the desorption peaks are clearly shifted to higher temperatures and are centered in a temperature range from 330–336 °C. Furthermore, there is a certain temperature window starting from 200 °C (the temperature where the whole uncapped DIP film has desorbed) in which no desorption of DIP could be measured for the capped films indicating that the encapsulation layer works very effectively. This temper-

ature window Δ T_i has its smallest value for the thinnest capping layer ($\Delta T_1 = 35\,°C$) and for the other capping layers $\Delta T_2 = 67\,°C$, $\Delta T_3 = 87\,°C$, $\Delta T_4 = 76\,°C$. Beyond this temperature window desorption of the organic film through the capping layer starts.

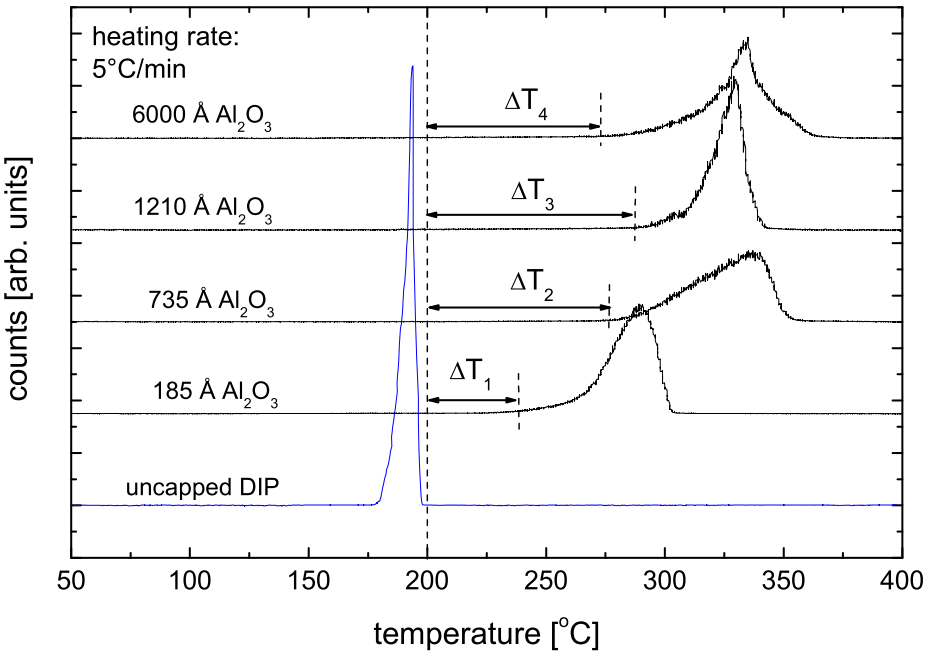

Figure 8.3: TDS data of an uncapped DIP film and DIP films capped with Al_2O_3 films of different thicknesses. The spectra were normalized and are shifted for clarity. The heating rate of the capped DIP films was 5 °C/min. The spectra of the capped DIP films are shifted to higher temperatures [TDS measurements were performed in collaboration with S. Meyer].

8.1.3 Discussion

From the TDS measurements an increase of the desorption temperature of more than 150 K could be observed for the DIP films capped with an Al_2O_3 layer compared to the uncapped DIP films. The capping layer also seems to be very effective for a certain temperature range where no desorption could be observed. This temperature range was larger for thicker capping layers and for smaller heating rates. Lower heating rates shift

the center of mass of the TDS spectrum to higher temperatures.

It seems that even thin Al_2O_3 films of 185 Å thickness already prevent the desorption of DIP molecules very effectively. However, from a certain capping layer thickness on no further increase in the thermal stability of the DIP film was observed which could be due to an insufficient capping at the edges.

Compared to the rather sharp desorption spectrum of uncapped DIP films which can be attributed to the 'bulk' desorption capped DIP films have a more extended desorption spectrum with different features such as small spikes. We consider these sharp peaks in the spectra of capped films to come from individual desorption channels such as small cracks. These cracks or defects give rise to a limited local desorption of the underlying organic film but does not lead to the desorption of the entire film. So far, we may speculate that these cracks or defects are thermally induced since no desorption was detected in a temperature range ΔT_i (i=1, ..., 4) above the desorption temperature of uncapped DIP films.

From the previous chapter we have seen that the oxide capping layer apparently is relatively near to the concept of a 'closed' layer and does not penetrate strongly upon deposition. The aluminum oxide layer kinetically hinders the organic molecules from desorption. However, the TDS spectra indicate that from a certain temperature on DIP molecules desorb and that at a certain temperature depending on the heating rate and the oxide layer thickness the whole organic film has been desorbed.

The TDS measurements allowed us to obtain information on the overall thermal stability of the capped DIP films without taking into account eventual structural changes of the organic film, of the aluminum oxide layer or of the Al_2O_3/DIP interface. However, for the application in organic field-effect transistors where the charge carrier mobility is very strongly related to the structural order of the organic film further investigations have to be carried out to shed more light on the microscopic breakdown mechanism of capped organic films at elevated temperatures.

8.2 Thermal stability of uncapped DIP films

8.2.1 Specular reflectivity of uncapped DIP films

From TDS measurements we know that the desorption temperature of DIP films on silicon oxide substrates lies around 190 °C. We have performed *in-situ* XRD measure-

ments to study the desorption of the organic film as a function of temperature. The experimental details of such measurements are described in Sec. 5.2. Figure 8.4 shows the specular X-ray refelctivity curves of the DIP sample (sample 1, see Tab. 8.4) for temperatures ranging from RT to 200 °C.

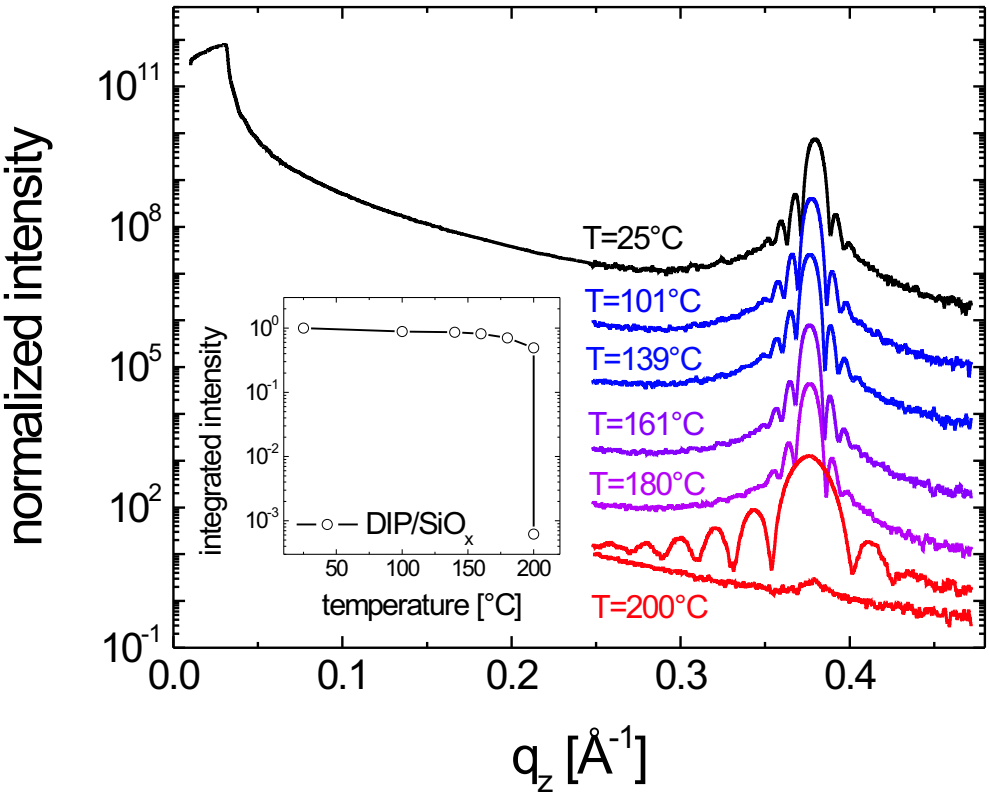

Figure 8.4: Specular X-ray reflectivities of uncapped DIP films for different temperatures. The DIP Bragg reflection remains nearly unchanged up to T = 200 °C where it disappears quickly (lower curve). The inset shows the attributed integrated Bragg intensity as a function of temperature.

The DIP Bragg reflection virtually does not change up to 180 °C. The Laue oscillations around the DIP Bragg peak correspond to a coherent film thickness of ca. 740 Å. At T = 200 °C the Bragg peak has changed significantly. Its intensity has decreased

drastically and also the Laue oscillations are much broader corresponding to a coherent thickness of ca. 280 Å, thus only around 37 % of the initial coherent thickness are left. After ca. 14 min at the same temperature the DIP Bragg peak has nearly disappeared and no Laue oscillations could be recognized anymore. The inset of Fig. 8.4 shows the integrated DIP Bragg intensity (being a measure for the crystallinity of the DIP film) for the different temperature steps. It confirms the TDS data with a desorption temperature of ca. 190–200 °C. Figure 8.5 shows the rocking scans on the DIP Bragg

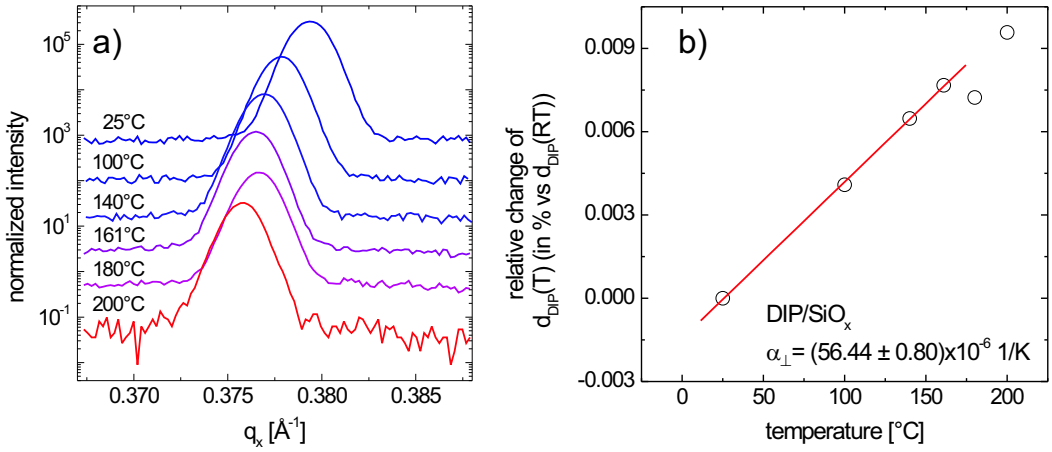

Figure 8.5: (a) Rocking scans of DIP films on silicon oxide for temperatures up to T = 200 °C. (b) Relative deviation of the DIP lattice parameter, d_{DIP}, from the RT-value. The slope of the linear fit corresponds to the out-of-plane thermal expansion coefficient, $\alpha_\perp$.

reflection for the different temperature steps (a) and the relative deviation of the DIP lattice parameter, d_{DIP}, from the RT value (b). The slope of the linear fit to these data points corresponds to the thermal expansion coefficient, $\alpha_\perp$, of DIP in the out-of-plane direction. For this specific sample a value of $(56.44 \pm 0.80) \times 10^{-6}$ 1/K was determined which is slightly lower than the values determined by Dürr *et al.* who measured values of 71.3 and 80.3×10^{-6} 1/K [57]. This small deviation can be due to slightly different preparation conditions and different film thicknesses. Furthermore, the rocking widths of the curves displayed in Fig. 8.5(a) decreased from 0.0082 ° at RT to 0.0074 ° at 200 °C.

8.2.2 Conclusions

To summarize, the crystallinity of the DIP films (expressed by the integrated DIP Bragg intensity) deposited on silicon oxide substrates starts to decrease around 160 °C and drops significantly at 200 °C. This decrease of the crystallinity can be attributed to the desorption of the DIP film. The decreasing periodicity of the Laue oscillations around the DIP Bragg reflection (and thus the decrease of the coherent thickness) can be explained by a layer-by-layer desorption of the organic film (laterally homogeneous desorption). Even at 200 °C where the DIP film desorbs the Bragg reflection with its Laue oscillations can still be recognized indicating that the DIP film remains highly ordered even at its desorption temperature. The rocking curves also indicate that the mosaicity of the organic film can still decrease at higher temperatures. This annealing effect might have a positive influence on the charge carrier mobility of devices. The thermal expansion coefficient of the organic film is around 50-80 $\times 10^{-6}$ 1/K in the out-of-plane direction and is thus an order of magnitude larger as typical values for aluminum oxide films.

8.3 Thermal stability of capped DIP films - Specular reflectivity

To obtain structural information of the layer system Al_2O_3/DIP *during* the heating process we performed *in-situ* X-ray diffraction experiments. The sample (sample 2, see Tab. 8.4) was heated up in steps from 25 °C to 500 °C and after thermal equilibration (on a timescale of a few minutes) X-ray reflectivity scans were taken at each intermediate temperature. Since the film was kept at elevated temperatures for several hours the corresponding averaged 'heating rate' of ~ 0.49 °C/min is of course much lower than in the TDS experiments.

From X-ray reflectivity measurements we determined the electron density profile, ρ(z), and from the out-of-plane DIP Bragg peaks we determined the lattice parameter of the organic film structure and the coherent thickness was determined from its Laue oscillations.

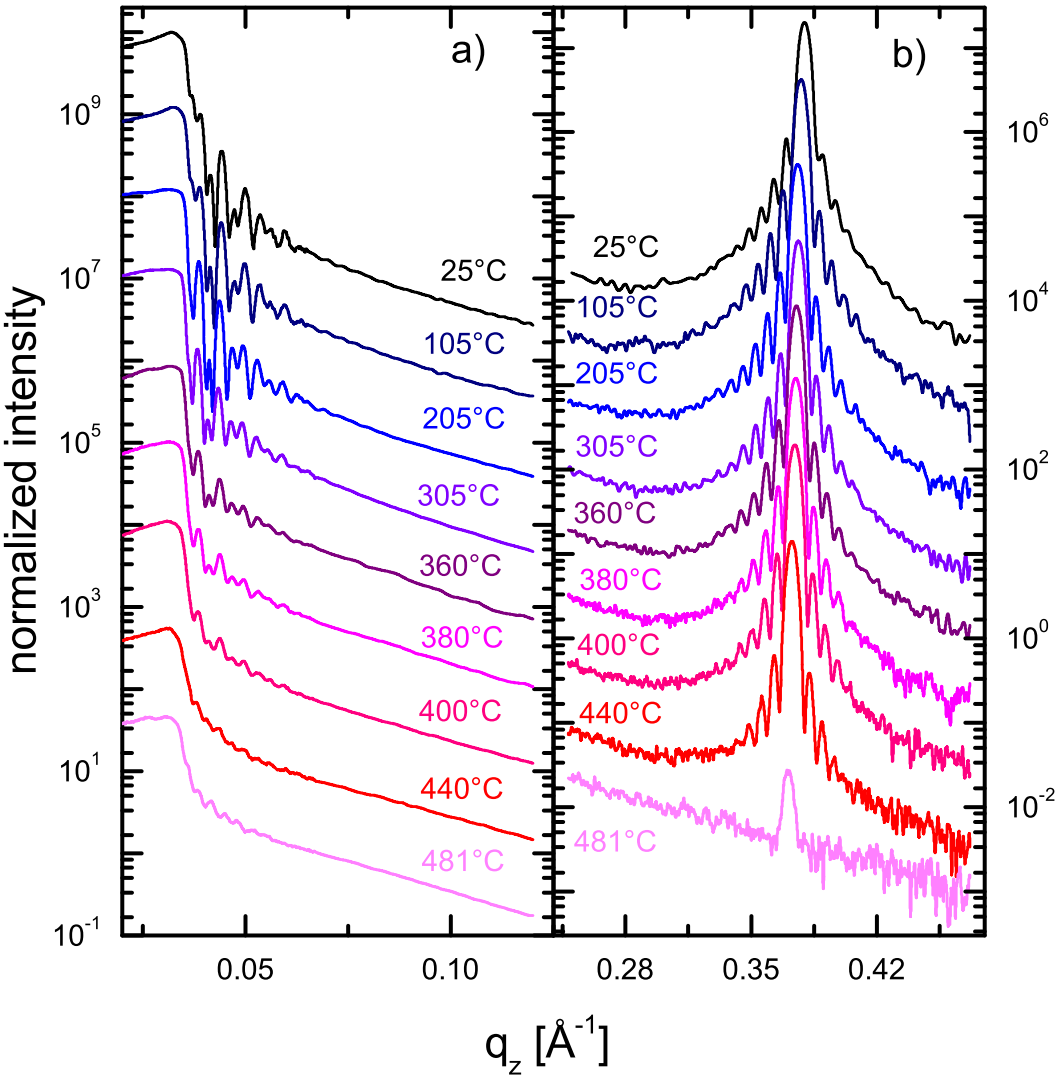

Figure 8.6: (a) Specular X-ray reflectivity of a capped DIP film for different temperatures with the first order DIP Bragg reflection (b) for T = 25 °C to 410 °C.

T [°C]	L_{Alox} [Å]	ρ_{Alox} [el/Å^3]	σ_{Alox} [Å]	L_{DIP} [Å]	ρ_{DIP} [el/Å^3]	σ_{DIP} [Å]
25	606.8	0.889	54.3	1002.1	0.521	43.6
100	600.3	0.891	57.9	1004.4	0.504	43.4
205	584.3	0.872	61.1	1030.3	0.485	47.3
305	592.5	0.860	67.2	1021.6	0.466	54.4
330	605.7	0.859	67.1	1021.4	0.458	55.8
380	625.3	0.877	64.6	1090.0	0.316	62.4

Table 8.1: Results of least-square fitting by the Parratt formalism. Here only the parameters for the aluminum oxide layer and for the DIP layer are displayed.

As can be seen from Fig. 8.6(a), Kiessig interference fringes are clearly visible up to 380 °C, but are gradually damped out for still higher temperatures. Importantly, the Bragg reflection at $q_z \approx 0.38\,\text{Å}^{-1}$ (Fig. 8.6(b)) remains virtually unchanged up to 440 °C, showing that the DIP crystal structure stays intact. Until up to 460 °C, the Laue oscillations around the DIP Bragg peak show no significant changes implying that the organic film does not only remain crystalline, but also coherently ordered [14].

From least-square fitting of the reflectivity curves by the Parratt formalism we receive informations on the temperature dependent variation of the electron density, the thickness and the roughness of the different materials. Table 8.1 shows the collected results. Only the parameters for the aluminum oxide and for the DIP layer are displayed here.

While the electron density of the Al_2O_3 layer remained essentially constant the electron density of the DIP film decreased with increasing temperature. This decrease of the electron density of DIP is slightly higher than expected from the linear thermal expansion ($\alpha_\perp = 56\text{-}80\times10^{-6}$ 1/K) as determined from uncapped DIP films. However, the thermal behavior of the lattice parameters is non-linear at temperatures exceeding the desorption temperature of uncapped DIP films and other effects contribute, as will be shown below. The roughnesses of both the capping layer and the DIP film increased with temperature.

In order to shed more light on the degradation process and the 'kinetics' of the breakdown at high temperatures, we performed further *in-situ* X-ray diffraction experiments for samples which had an aluminum oxide capping layer with a higher metallic content

T [°C]	L_{Alox} [Å]	ρ_{Alox} [el/Å^3]	σ_{Alox} [Å]	L_{DIP} [Å]	ρ_{DIP} [el/Å^3]	σ_{DIP} [Å]
25	662.0	0.811	25.5	479.1	0.318	26.0
230	664.7	0.853	28.7	485.9	0.341	27.1
270	680.4	0.864	23.6	482.5	0.280	21.0

Table 8.2: Results of least-square fitting of the XRR data of a DIP film capped by a non-stoichiometric oxide layer by the Parratt formalism. Here only the parameters for the aluminum oxide layer and for the DIP layer are displayed.

(dependence on the stoichiometry), for samples which were ramped up with a higher averaged heating rate (dependence on the heating rate) and for samples with different capping layer thicknesses.

8.3.1 Dependence on the stoichiometry

The same experiment as before was conducted for a DIP film which accidentally had a more metal-rich aluminum oxide layer (sample 3, see Tab. 8.4). The exact numbers for the stoichiometry of this sample are not known but from comparison with the properties of other sputtered samples it was concluded that this sample had a higher metallic content. Usually, the brownish color of the sputtered aluminum oxide layer is already a hint for a higher metallic content (stoichiometric aluminum oxide layers are totally transparent).

The averaged heating rate of $\sim 0.33\,^{\circ}$C/min was approximately the same as for the previous sample (sample 2). The specular reflectivity and the DIP Bragg reflection for the different heating steps are displayed in Fig. 8.7(a,b). The parameters obtained for fitting the reflectivity curves by the Parratt formalism are summarized in Tab. 8.2. Apparently, the surface of the Al_2O_3 layer and its interface with the DIP film remained well-defined up to 270 °C. But at 368 °C the DIP Bragg reflection already disappeared which is more than 100 K below the breakdown temperature of the 'stoichiometric' sample 2. The capping layer with the higher metallic content seems to be less stable.

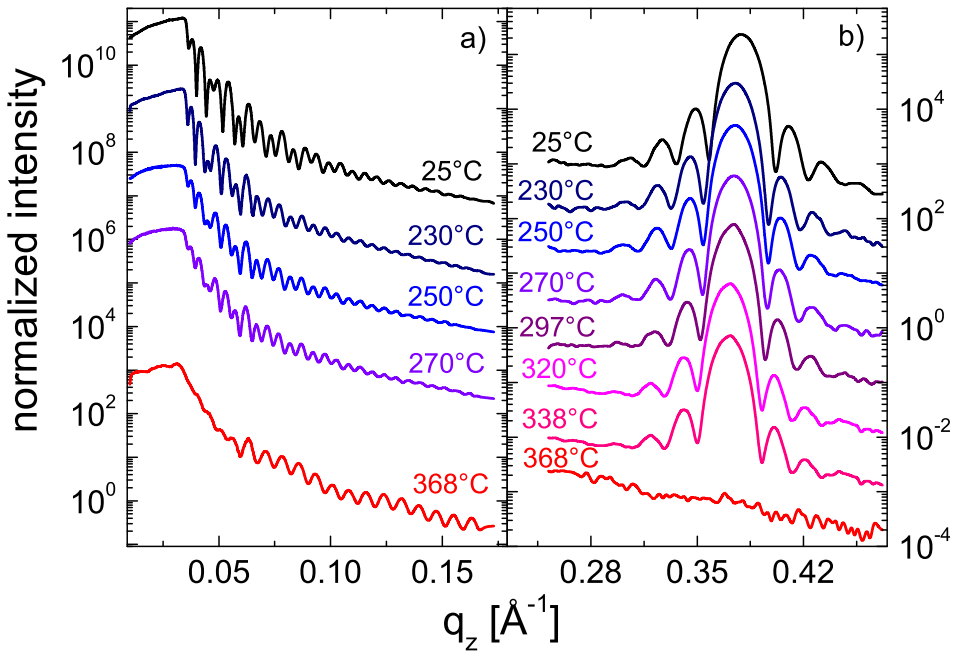

Figure 8.7: Specular X-ray reflectivity (a) and first order DIP Bragg reflection (b) of a DIP film capped with a metal-rich aluminum oxide layer at different temperatures.

8.3.2 Dependence on the heating rate

From the TDS measurements it turned out that the heating rate has an influence on the thermal stability of the capped organic films. Compared to the TDS measurements the heating rates of the *in-situ* XRD measurements were much smaller and therefore also the breakdown temperature was shifted to much higher temperatures. Here, we compare XRD measurements of a sample (sample 4, see Tab. 8.4) with comparable sample specifications to sample 2 but with a heating rate of ca. 2.66 °C/min (a factor of 6 larger). The results of these measurements are shown in Fig. 8.8(a,b). Again, no substantial changes in the reflectivity curves could be observed up to temperatures far above the desorption temperature of uncapped films. Although the 'high heating rate' sample was ramped much faster than the metal-rich sample the structural breakdown happened at much higher temperatures but below temperatures of more stoichiometric

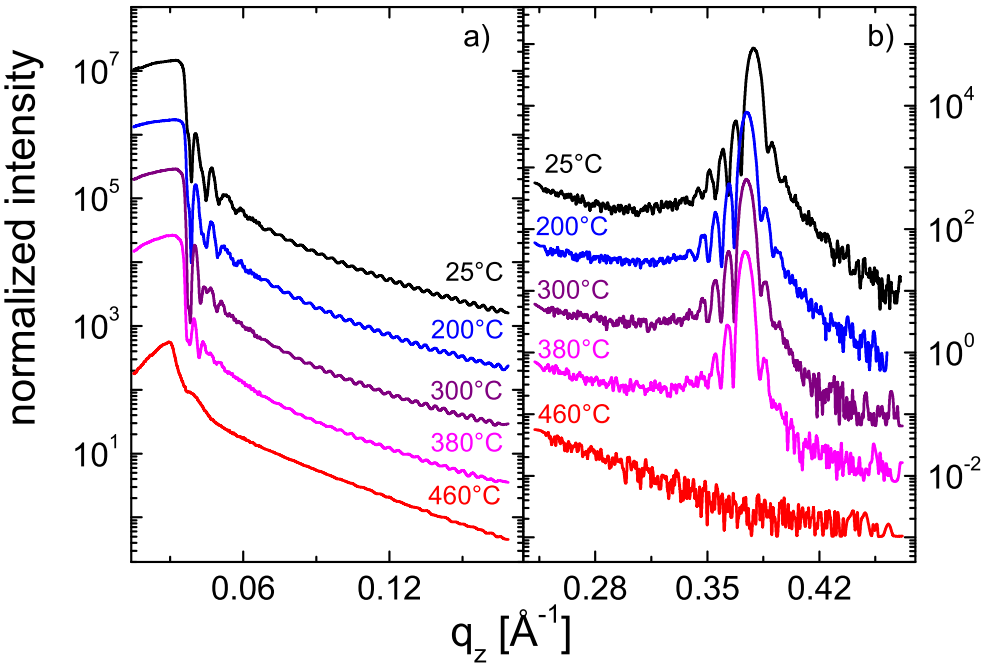

Figure 8.8: Specular X-ray reflectivity (a) and first order DIP Bragg reflection (b) of a DIP film capped with an aluminum oxide layer at different temperatures. The sample was ramped with a higher heating rate.

samples ramped at low heating rates.

8.3.3 Dependence on the capping layer thickness

Figure 8.9 shows the specular reflectivity and the Bragg peak at different heating steps (the mean heating rate was about 0.75 °C/min) for a DIP film capped with a 1212 Å thick aluminum oxide layer (sample 7, see Tab. 8.4).

The Kiessig fringes in panel (a) show the different contributions from the DIP film (360 Å) with its low frequency oscillations modulated by the contributions from the aluminum oxide film (1212 Å) high frequency oscillations. They change only slightly with increasing temperature indicating that the interfaces do not change significantly upon heating. At around 410 °C the thickness oscillations become less pronounced due

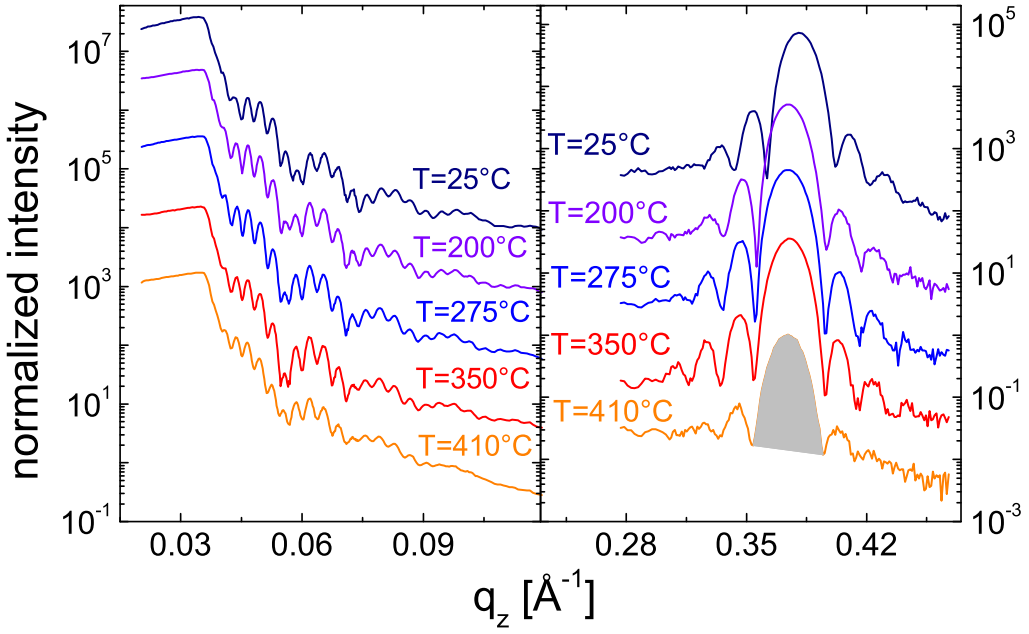

Figure 8.9: Specular X-ray reflectivity (a) and first order DIP Bragg reflection (b) of a capped DIP film for different temperature steps from T = 25 °C to 410 °C. Thickness of the aluminum oxide capping layer: 1212 Å.

to increasing roughness. In panel (b) the first order Bragg reflection of DIP is displayed for the different temperature steps. Apart from the thermal expansion which shifts the peak to smaller q_z values no substantial changes can be observed. The Laue oscillations reveal a coherent thickness of ca. 326 Å which is constant with temperature and which is about two monolayers less than the total DIP film thickness of ca. 360 Å.

From least-square fitting of the reflectivity curves by the Parratt formalism, information about the temperature dependence of the electron density profile was obtained. Table 8.3 summarises the results for the aluminum oxide and for the DIP layer. For this specific sample the electron density of aluminum oxide remained nearly constant upon heating while the electron density for the DIP film decreased up to 410 °C. Again, the decrease of the DIP electron density can not only be contributed to the thermal expansion of the film.

T [°C]	L_{Alox} [Å]	ρ_{Alox} [el/Å^3]	σ_{Alox} [Å]	L_{DIP} [Å]	ρ_{DIP} [el/Å^3]	σ_{DIP} [Å]
25	1212.4	0.943	33.4	359.4	0.396	27.8
200	1210.9	0.957	34.6	359.6	0.320	30.5
275	1210.0	0.963	34.8	362.1	0.306	30.8
350	1208.8	0.962	36.8	359.7	0.271	32.2
410	1204.9	0.959	38.0	363.6	0.276	36.9

Table 8.3: Results of least-square fitting by the Parratt formalism. Here, only the electron density, the thicknesses and the roughness of the aluminum oxide and DIP films are displayed.

As a comparison to the sample 7 the influence of a rather thin (sample 5, Fig. 8.10(a,b)) and a much thicker aluminum oxide capping layer (sample 6, Fig. 8.11) on the thermal stability of DIP are investigated. The exact sample specifications are tabulated in Tab. 8.4.

Apparently, both capping layers stabilize the organic film very effectively. For the sample with the thinner capping layer a similar behavior of the thickness oscillations was observed as for the other samples. For the very thick capping layers the interference fringes disappear due to finite instrumental resolution (of $\Delta 2\theta = 0.014\,^\circ$) and due to interface roughness. But again the DIP Bragg reflection remained unchanged for both samples up to their breakdown temperature at 410 °C and 500 °C for sample 5 and 6, respectively.

At the breakdown temperature the Bragg peaks for all capped DIP films decreased rapidly with time until no crystalline DIP was left (see Sec. 8.7.1).

8.3.4 Summary

Several samples with different film thicknesses, different stoichiometry of the aluminum oxide layer and different heating rates were measured and for all samples a strong enhancement of the thermal stability of the DIP film could be obtained. For all samples the thermal behavior of the interfaces and the crystalline structure of DIP were similar. However, the temperature for which the DIP Bragg reflection disappeared differed from sample to sample depending on the sample parameters such as the thickness and the stoichiometry of the capping layer and on the heating rate. Importantly, the coherent

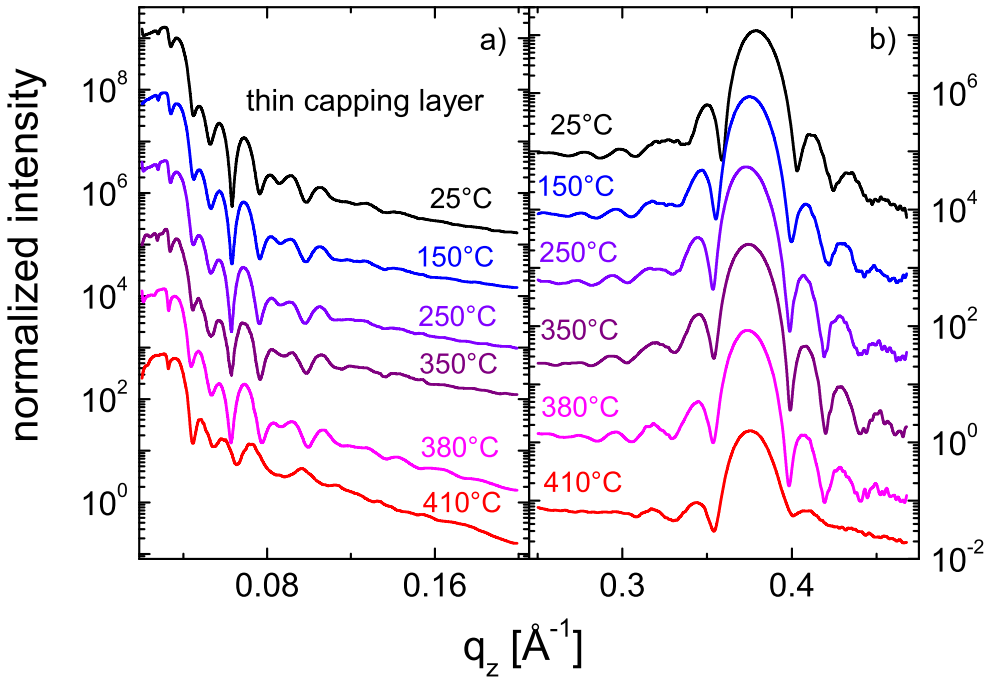

Figure 8.10: Specular X-ray reflectivity (a) and first order DIP Bragg reflection (b) of a capped DIP film for different temperature steps from T = 25 °C to 410 °C. Thickness of the aluminum oxide capping layer: 166 Å.

thickness of the DIP films remained constant even at the breakdown temperature of each sample. The dependence on the parameters will be addressed below (see Tab. 8.4 and Sec. 8.5).

From the observations of the temperature dependent reflectivity curves including the DIP Bragg reflection we may conclude that the overall heterostructure remained essentially unchanged during heating. Aluminum oxide did not penetrate significantly into the DIP film and the crystalline structure of the organic film was not affected up to a certain, rather high temperature which was specific for each sample (see Sec. 8.5).

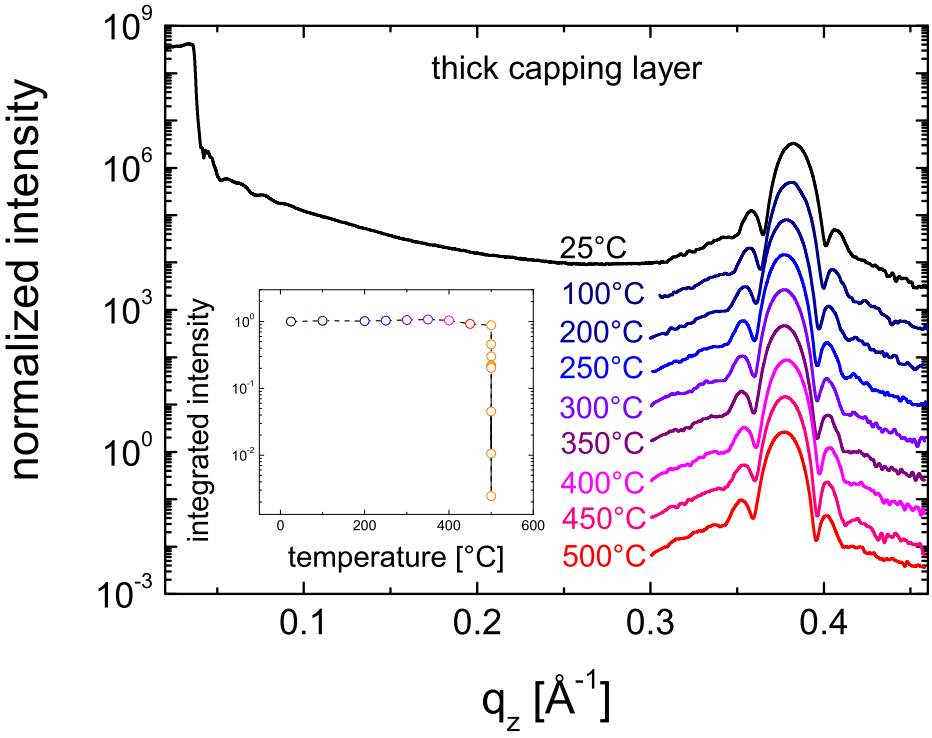

Figure 8.11: Specular X-ray reflectivity with first order DIP Bragg reflection of a capped DIP film for different temperature steps from T = 25 °C to 500 °C. Thickness of the aluminum oxide capping layer: 5938 Å. The inset shows the integrated DIP Bragg intensity as a function of temperature.

8.4 Thermal behavior of the disorder - Offspecular scattering

The specular reflectivity is sensitive to the average density profile along the surface normal. But X-ray scattering experiments also allow for the determination of the statistical properties of surfaces or interfaces, *i.e.*, the lateral length of surface morphologies and the correlations between buried interfaces as described in Sec. 5.3.

Generally, two types of diffuse scattering data are collected to extract morphological information through height-height correlations at one interface (transversal scans in Fig. 8.12(a)) and between interfaces in a multilayer (longitudinal offset scans in

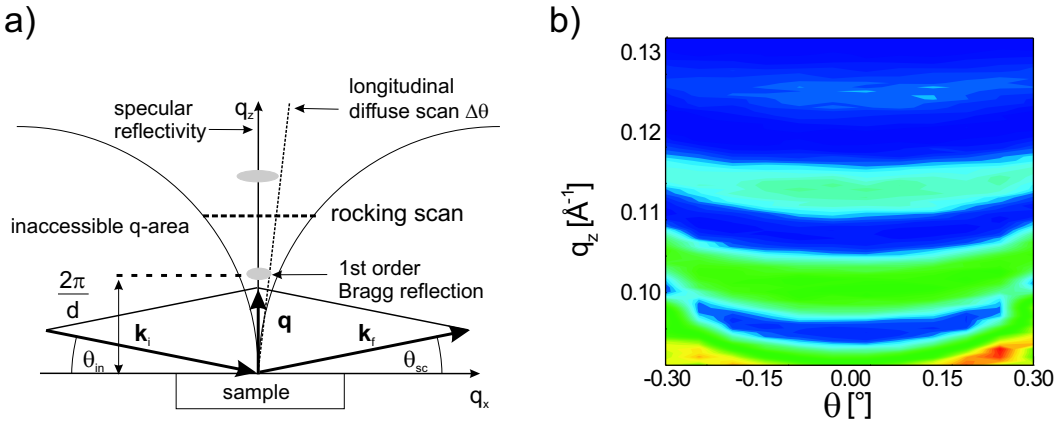

Figure 8.12: (a) Scans in reciprocal space with representation of the inaccessible areas. (b) Longitudinal offset scans for different offset angles $\Delta\theta$.

Fig. 8.12(a)). In Fig. 8.12(b) longitudinal scans at different offset angles (from -0.3 °– 0.3 °, in steps of 0.05 °) for a DIP film (368 Å) capped with a 533 Å thick aluminum oxide layer are displayed. Oscillations corresponding to the aluminum oxide layer are clearly visible.

Figure 8.13 shows longitudinal offset-scans for (a) the sample with the metal-rich capping layer (sample 3), for (b) sample 2 (with an averaged heating rate of 0.49 °C/min), for (c,d) samples with different capping layer thicknesses (samples 7 and 5, respectively; for sample specifications see also Tab. 8.4), each taken at an offset angle of $\Delta\theta = 0.05$ ° for different temperature steps. These longitudinal diffuse scans allow for the determination of the aluminum oxide layer thickness independently from the specular X-ray reflectivity data as was already shown in Sec. 7.3.2.

Generally, the offspecular scans do not change significantly up to a temperature specific for each sample. The temperature from which on changes in the Yoneda wing and the oscillations can be observed depends on the breakdown temperature of each sample. For the metal-rich sample with the lowest breakdown temperature (at 360 °C) significant changes thus can be observed from T = 230 °C on, while these changes appear for the 'high heating-rate' sample only around T = 300 °C (160 °C below its breakdown temperature).

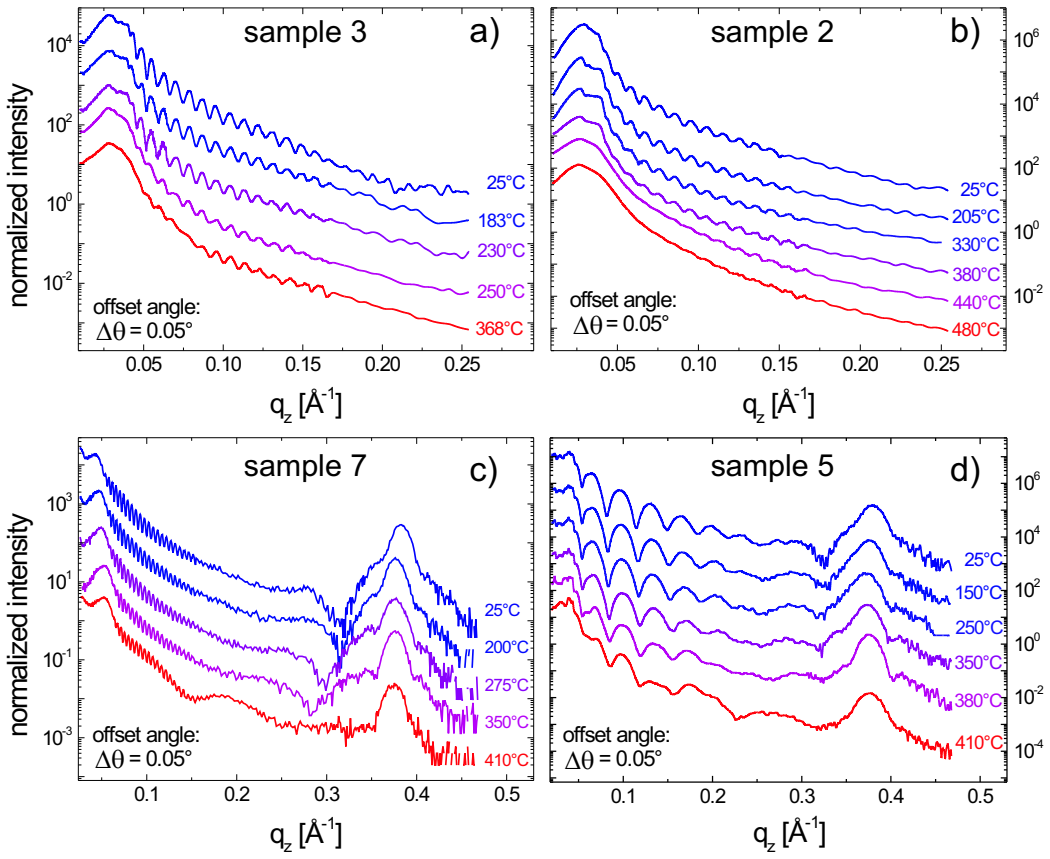

Figure 8.13: Longitudinal offset scans of DIP films capped with an aluminum oxide layer for samples 3,2,7 and 5 (a,b,c and d, respectively).

For the offspecular scans in Figs. 8.13(c,d) a contribution from the DIP Bragg reflection can be observed indicating that due to resolution effects a small contribution of the specular DIP signal is still present in the data. However, in contrast to the metal-rich and the 'high heating-rate' samples an additional disordered layer of increasing thickness can be observed for the samples in Fig. 8.13(c,d). In (c) the additional periodicity at T = 410 °C corresponds to a thickness of around 50 Å which cannot come from the much thinner native SiO_x layer nor from the crystalline DIP film. This additional periodicity can also be observed in (d) due to the modulation of the oscillations.

So far we can only speculate on the origin of this additional disordered layer. It

may come from a thin layer which forms at the Al_2O_3/DIP interface due to enhanced penetration of Al_2O_3 into the DIP film thus leading to the destruction of the structural order of the topmost organic layers. It might also originate from chemical reactions between the Al_2O_3 and the DIP or from a thin DIP film wetting the aluminum oxide layer on top.

8.5 Thermal behavior of the DIP crystallinity - Bragg intensities

In addition to the position of the DIP Bragg reflection, which gives the out-of-plane lattice parameter, also the integrated DIP Bragg intensity, which gives the degree of order in the film, was evaluated. Its temperature dependence gives the thermal disordering of the DIP film. It was calculated by multiplying the area under the background-corrected Bragg peak with the rocking width. The integrated Bragg intensity was used to compare the influence of different experimental conditions and material properties (capping layer thickness, stoichiometry and heating rate) on the stability of the organic film. The specifications of the samples are given in Tab. 8.4.

sample	L_{Alox} [Å]	L_{DIP} [Å]	Al:O	Ar [%]	R [°C/min]	T_{bd} [°C]
1	-	773	-	-	0.89	190
2	607	1002	$(0.66)^{**}$	(-)**	0.49	480
3	662	479	$(>0.66)^{**}$	(-)**	0.33	360
4	618	773	$(0.66)^{**}$	(-)**	2.66	460
5	166	334	0.606	0.75	0.56	410
6	5938	402	0.63	0.59	0.58	500
7	1212	360	0.733	0.40	0.75	410
8	520	450	0.602	0.37	0.37	410
9*	135	385	-	-	-	160

Table 8.4: Dependence of the breakdown temperature T_{bd} on the capping layer thickness (L_{Alox}), stoichiometry (Al:O ratio) and argon content, on the DIP film thickness (L_{DIP}), and the averaged heating rate. (*) Gold capping layer from [25]; (**) values not known/estimated.

Figure 8.14 shows the integrated Bragg intensity of capped DIP films. In the fol-

lowing by the term 'breakdown temperature' we will assign the temperature at which the integrated intensity starts to drop significantly ($\sim 10\,\%$). This allows to compare the thermal stability of samples with different film thicknesses, stoichiometries, etc., quantitatively.

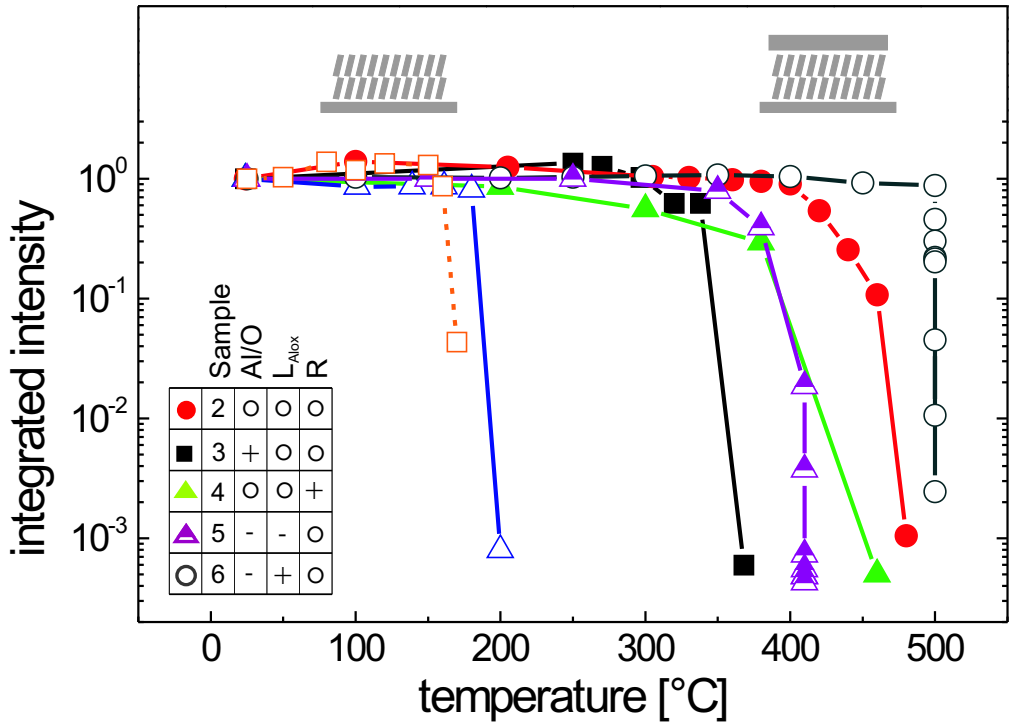

Figure 8.14: Comparison of the integrated DIP Bragg intensity of different samples. Sample 1 (open triangle) had no capping layer, samples 2-6 had an aluminum oxide capping layer but different sample specifications or heating rates (see Tab. 8.4). Sample 9 (open square) had a gold film instead of an aluminum oxide layer on top of DIP [25].

The integrated Bragg intensities of the capped DIP films have to be compared to the crystallinity of the uncapped DIP film (sample 1, see also Sec. 8.2) and a strong enhancement of the thermal stability of capped films can be found. Compared to the integrated intensity of sample 2 (which will be taken as a reference in the following) we

conclude that in accordance with TDS data higher heating rates shift the breakdown temperature to smaller values (sample 4). Furthermore, thick capping layers (sample 6) are more effective than thin capping layers (sample 5) and the metal-rich oxide layers (sample 3) show the tendency to break down at lower temperatures.[2]

The metal-rich capping layer was heated with the lowest averaged heating rate of all capped DIP films measured (0.33 °C/min) and compared to sample 2 it also had a thicker capping layer, all in all two factors which would favor higher breakdown temperatures. Nevertheless, the integrated intensity of this sample breaks down at much lower temperatures which can only be attributed to the higher metallic content of the capping layer of this sample. Metal-rich aluminum oxide layers seem to be less effective as capping layers. The limited stability of metal-rich capping layers could be seen in a series with purely metallic 'capping' layers (sample 9) which penetrate into the organic film at elevated tempeatures and destroy the structural order of the organic film.

The DIP Bragg peak also does not change significantly before a certain temperature is reached. Furthermore the organic film seems to undergo a certain post ordering since the Laue oscillations seem to be more pronounced at higher temperatures and the rocking width measured on the DIP Bragg reflection still decreases slightly (by about 16.8 % from 0.167 to 0.139) when going to higher temperatures, see Fig. 8.15.

8.5.1 Summary and conclusions

We found a strong enhancement of the thermal stability of crystalline DIP films induced by aluminum oxide capping layers. The crystallinity as expressed by the integrated DIP Bragg intensity is diminished at temperatures far above the desorption temperature of uncapped DIP films. The thermal stabilization was found to depend on parameters such as the averaged heating rate, the capping layer thickness and its stoichiometry.

Furthermore, we also found an anneling effect for DIP films at temperatures far above their uncapped desorption temperature. For temperatures below the desorption temperature it was recently shown that thermal annealing of organic films can heal out grain boundaries, increase the structural order and reduce the mosaicity which can improve the electrical properties of organic devices [11, 205, 206].

[2] Note, for sample 2, 3 and 4 the stoichiometries were not determined but from comparison with RBS measurments on different samples sputtered under comparable conditions a qualitative estimate is possible. Especially for sample 3 a higher metallic content can be concluded.

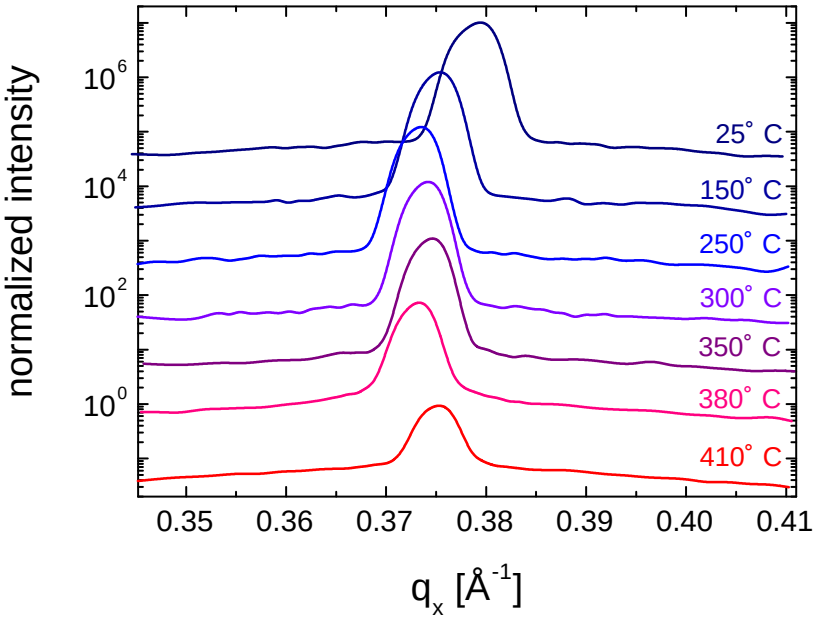

Figure 8.15: Transverse (rocking) scans on DIP Bragg reflection for different temperatures.

8.6 Thermal behavior of DIP lattice parameters

From temperature dependent measurements in the specular condition the position of the DIP Bragg peak allows to determine the out-of-plane lattice parameter as a function of temperature and thus the thermal expansion in the out-of-plane direction can be obtained. The same is possible for the in-plane lattice parameters. Since the DIP domains on silicon oxide have an isotropic orientation in-plane the latteral structure of the DIP unit cell can be determined from radial scans.

Figure 8.16 shows radial scans on a capped DIP film for different temperature steps. The measurements were performed for a sample with 334 Å DIP capped with a 166 Å thick aluminum oxide layer.

The capping layers allow for measuring the thermal expansion coefficients for temperatures far above the desorption temperature of DIP [15]. For DIP on silicon oxide three in-plane Bragg reflections could be observed at $q_{||} = 1.155\,\text{Å}^{-1}$, at $q_{||} = 1.469\,\text{Å}^{-1}$

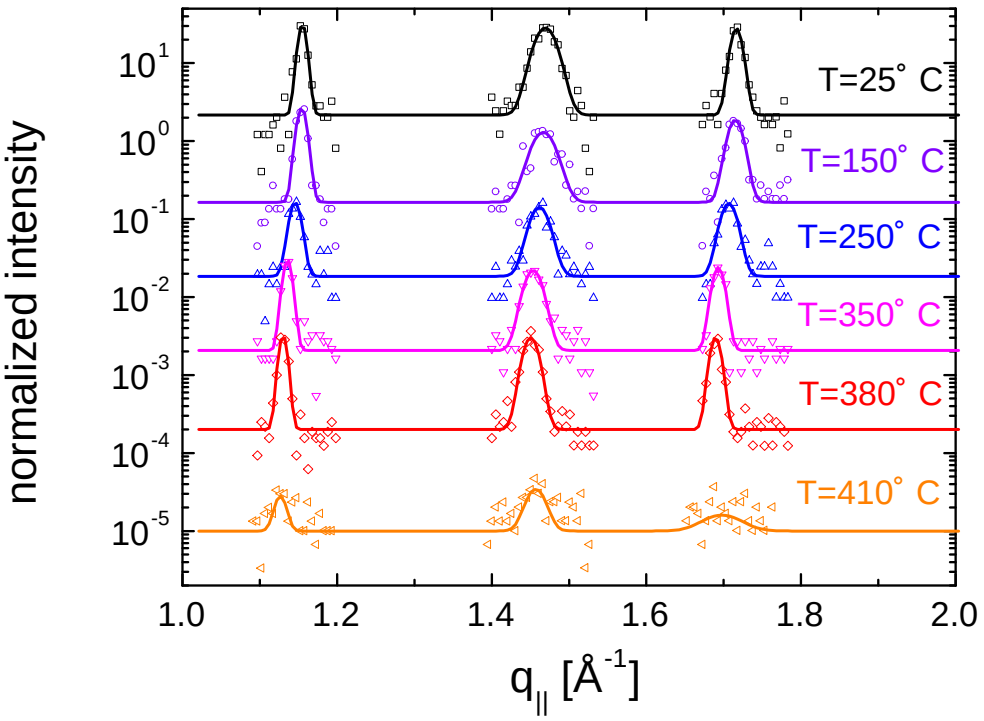

Figure 8.16: Radial scans of capped DIP films on silicon oxide for different temperature steps showing three in-plane Bragg peaks of DIP.

and at $q_{||} = 1.717$ Å^{-1}.[3] According to the unit cell proposed in Ref. [25] these correspond to the (11), (20) and (21) reflections, respectively.

At room temperature the following parameters for the capped DIP film could be obtained: $a = 8.55$ Å, $b = 7.05$ Å, $c = 16.57$ Å, and $\gamma = 89.7\,^\circ$ and the unit cell volume is $V = 998$ Å^3. The relative change of the lattice parameters and the unit cell volume of a capped DIP film on silicon oxide as a function of temperature is displayed in Fig. 8.17 (γ remained constant within $0.3\,^\circ$). As a comparison, the temperature dependence of the lattice parameter c^* of an uncapped DIP film and the relative linear thermal expansion of aluminum oxide is plotted.

[3] The intensity was relatively weak. The peak at $q_{||} = 1.469$ is rather broad compared to the two other peaks and also compared to the lateral size of the DIP islands as determined from AFM images.

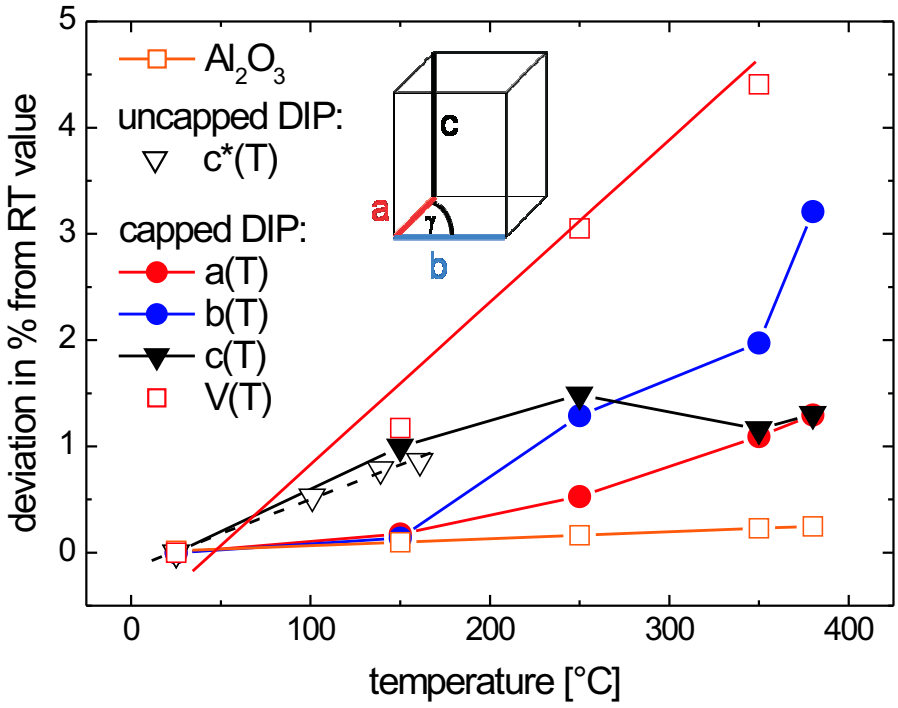

Figure 8.17: Relative change of the lattice parameters and the unit cell volume of a capped DIP film on silicon oxide as a function of temperature. The RT values are $a = 8.55$ Å, $b = 7.05$ Å, $c = 16.57$ Å, and $V = 998$ Å^3. As a comparison, the temperature dependence of the lattice parameter c^* of an uncapped DIP film and the relative linear thermal expansion of aluminum oxide are plotted.

The in-plane lattice parameters a and b do not show a linear behavior [15]. From 25 °C up to 150 °C the thermal expansion of a and b is comparable to the thermal expansion of sputtered aluminum oxide films, for which values of $\alpha = 6.5 \times 10^{-6}\,\mathrm{K}^{-1}$ are reported [36]. Above 150 °C, the DIP lattice parameters a and b show a much stronger increase than aluminum oxide and if approximated to a linear behavior, the thermal expansion coefficient of a and b is around $\alpha_a = 48.8 \times 10^{-6}\,\mathrm{K}^{-1}$ and $\alpha_b = 118.2 \times 10^{-6}\,\mathrm{K}^{-1}$, respectively. The approximated thermal expansion up to T = 250 °C of the out-of-plane lattice parameter c is around $\alpha_c = 66.6 \times 10^{-6}\,\mathrm{K}^{-1}$ (comparable to the thermal expansion c^* of the uncapped DIP). Although the individual lattice parameters show a non-linear ther-

mal behavior the unit cell volume, V, shows a rather linear behavior and a thermal expansion of $\alpha_V = 153 \times 10^{-6}\,\mathrm{K}^{-1}$ can be approximated. For anisotropic materials the thermal expansion of the unit cell volume can be expressed as $V(T) = V_0(1 + \alpha_V T)$, with $\alpha_V = \alpha_a + \alpha_b + \alpha_c$.

Regarding the effect of thermal expansion, compressive and tensile stresses on the position of a Bragg reflection (shift to lower, higher and lower q values, respectively) the thermal behavior of the DIP lattice parameters a, b and c can be understood in terms of thermal expansion and the formation and relaxation of thermally induced stresses in the organic film and at the interface to the aluminum oxide layer.

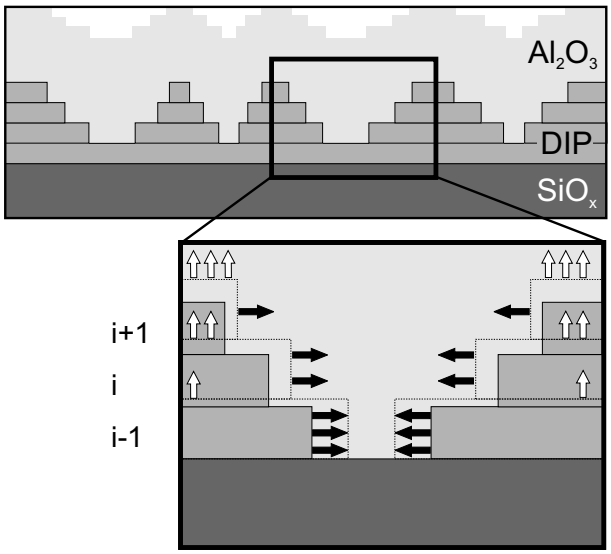

Figure 8.18: Schematic representation of the aluminum oxide/DIP interface. The typical pyramidal structure of DIP films leads to lateral and vertical stresses at the Al_2O_3/DIP interface.

Furthermore, the typical pyramidal structure of DIP films leads to lateral stresses acting on the aluminum oxide which gradually decrease from layer i to layer $i+1$ and it leads to vertical stresses acting on the aluminum oxide which gradually increase from layer i to layer $i+1$, as illustrated in Fig. 8.18. Inhomogeneities in the aluminum oxide layer such as regions with a higher content of trapped Ar or regions with a different stoichiometry may also enhance or relax the thermal stresses in the aluminum oxide film. The large mismatch in the thermal expansion of organic and aluminum oxide films by one order of magnitude enhances the thermally induced stresses. The pile up of elastic stress thus leads to fracture of the capping layer.

8.7 Time-dependent effects at elevated temperatures

For a given sample the thermal stability of the capped DIP film might not only depend on the temperature but also on time. To evaluate time-dependent effects we studied the evolution of the DIP Bragg reflection as a function of time for different temperatures and for different capping layer thicknesses. The first part of this section will be devoted to shortterm effects at the breakdown temperature of the specific samples and in the second part the longterm effects are studied.

8.7.1 Shortterm stability

As demonstrated in the preceeding sections the breakdown temperature depends on specific parameters such as the capping layer thickness, its stoichiometry, and the heating rate.

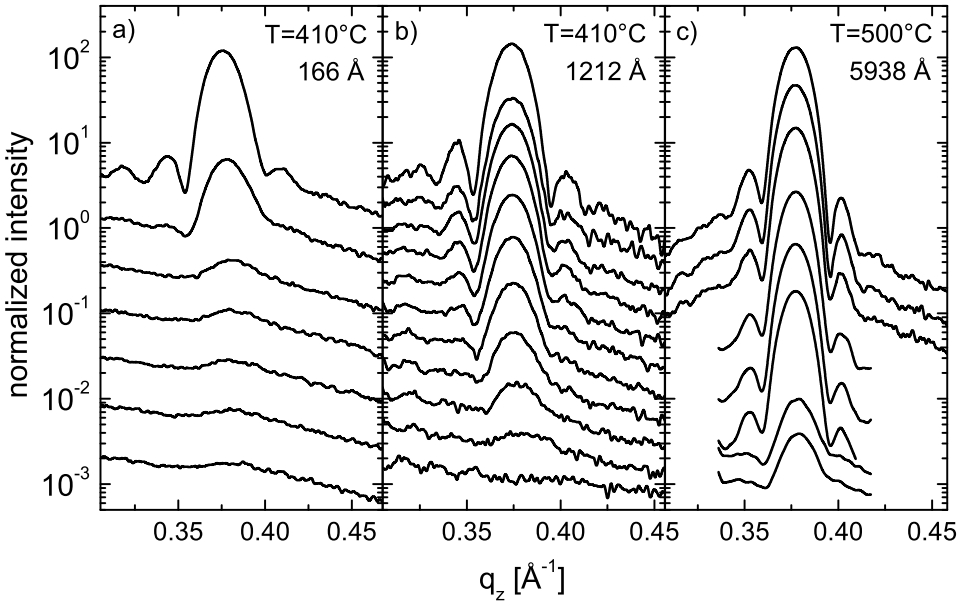

Figure 8.19: First order DIP Bragg reflection for samples at their breakdown temperature. (a) DIP film capped by 166 Å thick Al_2O_3 layer at T = 410 °C, (b) DIP film capped by a 1212 Å thick Al_2O_3 layer and (c) DIP film capped by a 5938 Å thick Al_2O_3 layer at T = 500 °C.

We succeeded to measure the time dependence of the integrated Bragg intensities of the DIP films at their specific breakdown temperatures. For different DIP films capped with Al_2O_3 layers of 166 Å, 1212 Å, and 5938 Å thickness the DIP Bragg peak was scanned as a function of time at constant temperature (see Fig. 8.19(a,b,c)). The measurements for the DIP films with the (a) 166 Å and (b) 1212 Å thick capping layer were performed at T = 410 °C while for the DIP film with a (c) 5938 Å thick oxide layer the measurements were carried out at T = 500 °C as a function of time. The data are offset for better visibility. At their breakdown temperature the Bragg intensity decreased rapidly as a function of time presumably due to desorption.

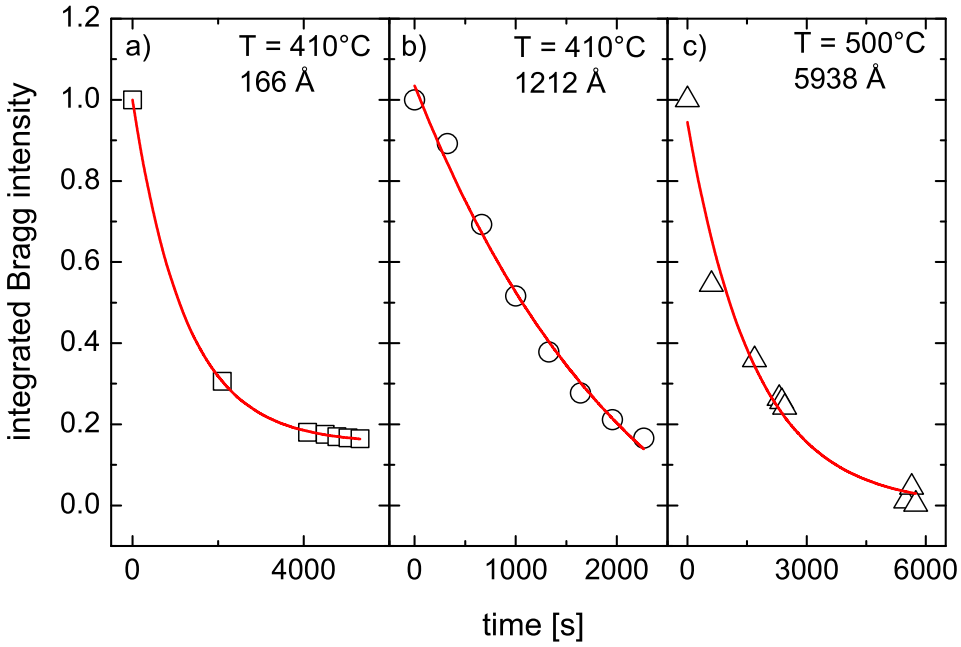

Figure 8.20: Evolution of the integrated DIP Bragg intensities as a function of time at constant temperatures.(a) DIP film capped by 166 Å thick Al_2O_3 layer at T = 410 °C, (b) DIP film capped by a 1212 Å thick Al_2O_3 layer and (c) DIP film capped by a 5938 Å thick Al_2O_3 layer at T = 500 °C.

Besides the decrease in intensity of the DIP Bragg peak the coherent thickness of the Laue oscillations remains constant until the latter disappear. The position of the DIP

Bragg reflection also remains unchanged indicating that no structural changes occur during this process. The integrated DIP Bragg intensities are displayed as a function of time in Fig. 8.20 for the respective samples. The data could be fitted to an exponential, $I(t) = I_0 + C\exp(-t/\tau_i)$, where τ_i is the time constant of the respective sample (a),(b) or (c). For the DIP film with a 166 Å thick capping layer the time constant is $\tau_a = 1224\,\mathrm{s}$, for the 1212 Å thick capping $\tau_b = 2195\,\mathrm{s}$ and for the thickest aluminum oxide capping layer the time constant is $\tau_c = 1668\,\mathrm{s}$.

8.7.2 Longterm stability

Time-dependence of the DIP crystallinity at T=300 °C

In the following the longterm effects of intermediate temperatures (T = 300 °C) on the Al_2O_3/DIP film structure is studied. The first order DIP Bragg reflection together with rocking curves were recorded for several times over a period of more than 300 hours, see Fig. 8.21(a,b).

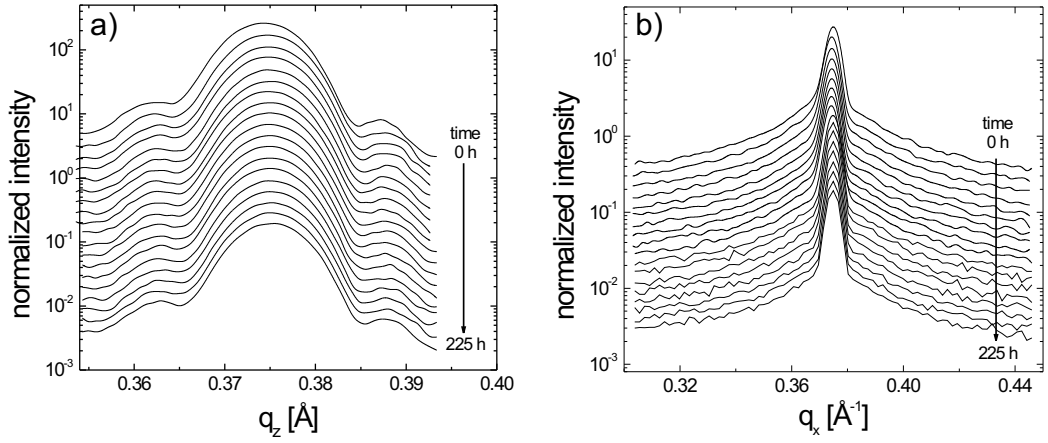

Figure 8.21: Evolution of the DIP Bragg reflection (a) and the rocking curves on it (b) at constant T=300 °C.

Both the DIP Bragg reflection and the corresponding rocking curves virtually do not change with time. For a more detailed analysis the evolution of the integrated DIP Bragg intensity with time was analyzed. The coherent thickness (Fig. 8.22(a))

remained constant over the whole period (∼760 Å) and the rocking width on the DIP Bragg reflection remained essentially constant (ca. 0.03 °) with time (b).

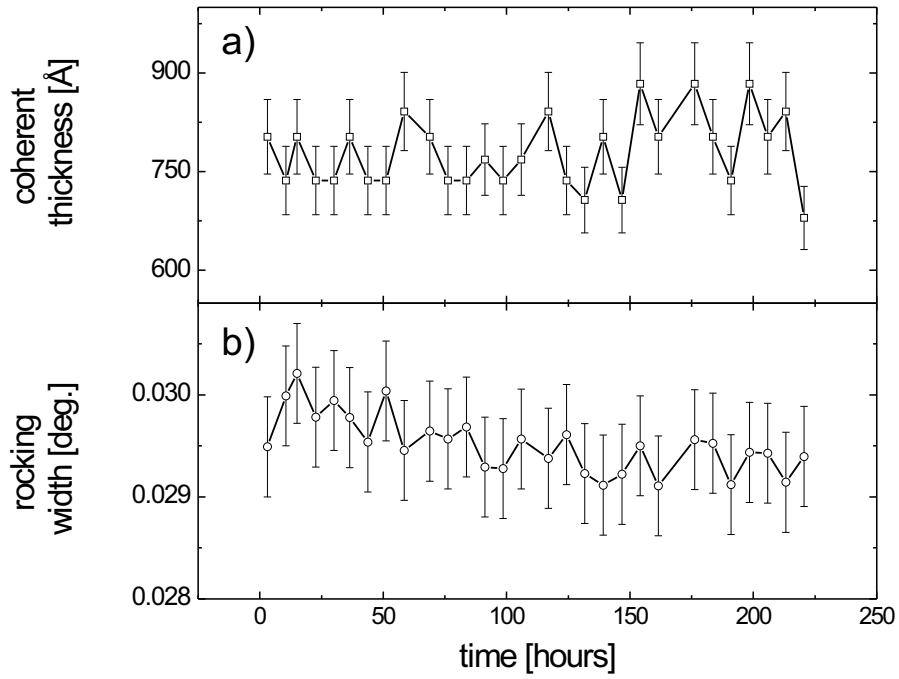

Figure 8.22: Evolution of the coherent thickness (a) and the rocking width (b) of the first order DIP Bragg reflection with time at constant T=300 °C.

The time dependence of the crystallinity of the DIP film is displayed in Fig. 8.23. The results clearly show that the integrated intensity decreases with time while the coherent thickness of the organic film remained unchanged over the whole period. The integrated Bragg intensity has dropped to 50 % of its initial value after ∼100 hours at 300 °C. This suggests that the desorption of the DIP film above 190 °C is kinetically limited by the aluminum oxide capping layer but can nevertheless take place through already existing and/or thermally activated defects in the capping layer. Since the coherent thickness remains constant the observed decrease of the integrated intensity at a certain temperature with time is related to desorption of the organic film from areas located near the defects in the capping layer, as for example microcracks or holes.

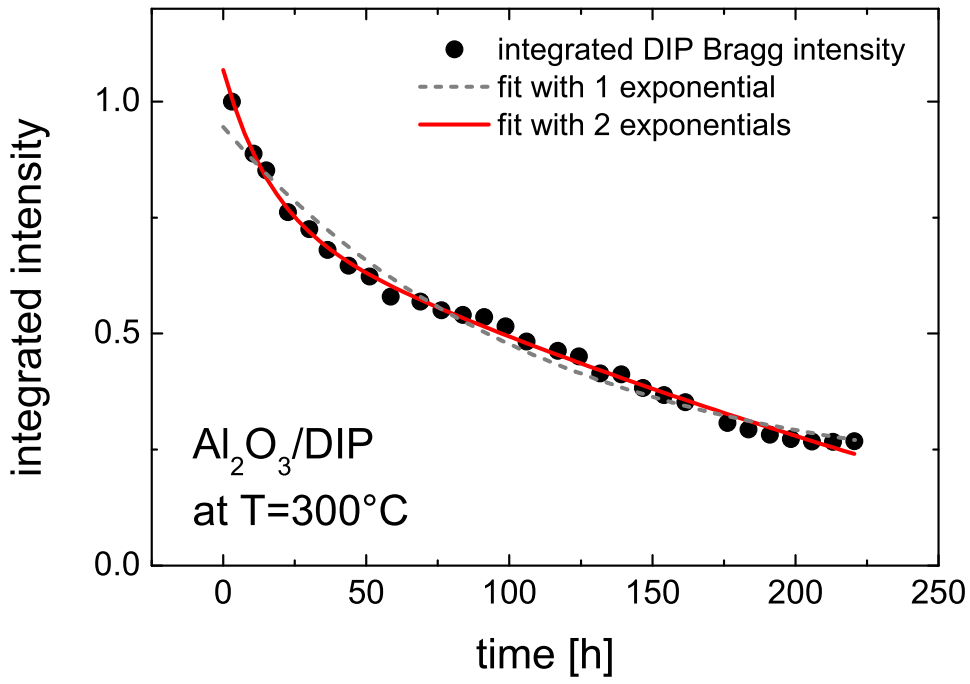

Figure 8.23: Time dependence of the integrated DIP Bragg intensity of a DIP film capped with an Al_2O_3 layer kept at $T = 300\,°C$. The integrated intensity decreases with time and the data points can be fitted at best by two exponentials, one dominating in the shortterm and one exponential dominating the longterm behavior. After ca. 100 h the integrated DIP Bragg intensity has decreased to ca. 50 % of the starting value.

In contrast to the shortterm effects at the breakdown temperature of the capped DIP film, the integrated Bragg intensity at intermediate temperatures cannot be fitted sufficiently well with only one exponential but with two exponentials of the form

$$I(t) = I_0 + C_1 \cdot e^{-\frac{t}{\tau_1}} + C_2 \cdot e^{-\frac{t}{\tau_2}}, \tag{8.1}$$

a rather good result is obtained. Here, I_0 is a constant and $C_1 = 1.47 \pm 0.78$, $\tau_1 = 517.0 \pm 376.8\,s$ are the constants of a longterm contribution and $C_2 = 0.32 \pm 0.03$, $\tau_2 = 16.4 \pm 3.2\,s$ are the constants for a shortterm contribution.

The photograph in Fig. 8.24(a) shows the sample after 400 h at 300 °C. Since for these X-ray diffraction measurements the DIP film was not prepared with a shadowing mask this might have led to desorption from the edges of the sample. We attribute the

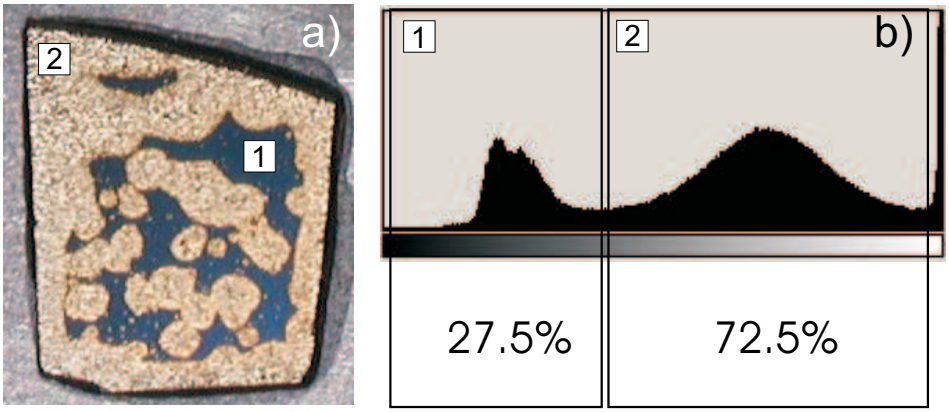

Figure 8.24: (a) Photograph of the sample from Fig. 8.23 kept at T=300 °C for 400 h. The sample exhibits a rough surface with a pattern of bright and dark regions. The luminescence distribution in (b) shows that the dark parts make 27.5 % of the sample surface.

bright parts of the sample to those where DIP has already desorbed. Obviously, a non negligible contribution comes from desorption at the edges. But also desorption from the middle of the sample could be observed. The circular shape of these areas might come from the desorption of the molecules through defects in the capping layer and successive diffusion of remaining molecules to these defects resulting in this characteristic circular shape. The histogram of the color distribution of the sample (Fig. 8.24(b)) suggests that the brighter parts, and therefore the parts where DIP has already desorbed, cover 72.5 % of the sample surface. This means that 27.5 % of the DIP film are still on the sample which is consistent with the longterm measurements where only about 20 % of the initial integrated intensity was left after 250 h.

With an optical microscope we took a closer look on the sample surface to study these patterns. In Fig. 8.25 the typical circular shape of these patterns could be observed in more detail ((b) and (d) are a close-up of (a) and (c), respectively). The red spot in Fig. 8.25(c,d) might come from DIP which desorbed through this defect in the capping layer and after cooling down the sample after 400 h at 300 °C some of the DIP molecules condensed at this spot.

These facts support the idea of two processes governing the desorption mechanism

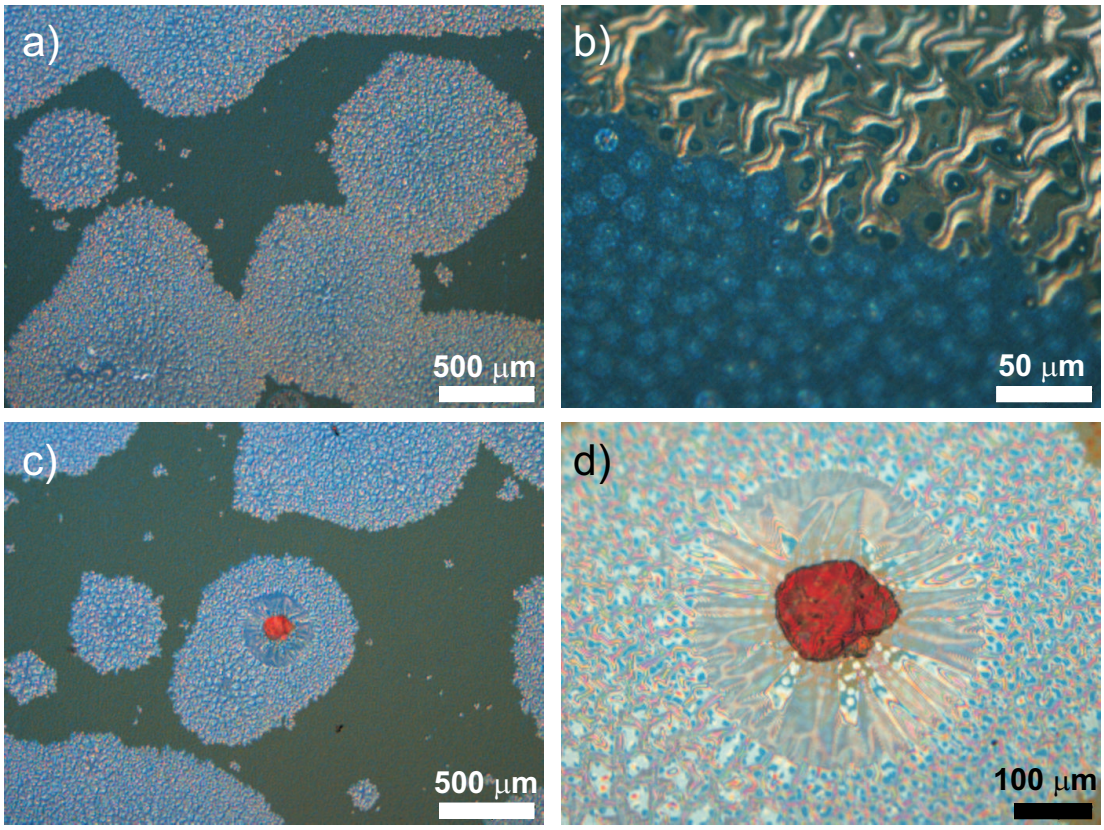

Figure 8.25: Optical micrographs of the sample from Fig. 8.23. Picture (a) and (c) show the circular shape of the patterns. In (c) a red spot can be observed. (b) and (d) are zooms into (a) and (b), respectively

as was indicated by the shortterm and longterm contributions for the integrated Bragg intensity. In a continuous process DIP molecules desorb through defects in the capping layer (shortterm contribution) and DIP molecules from around these defects diffuse to this spot to desorb from there which gives rise to the longterm contribution and the typical circular shape of the sample surface after many hours.

Formation of defects in the Al_2O_3 capping layer

However, the origin of the defects in the aluminum oxide capping layer is not yet clear. But as the bright and darker areas on the sample from Fig. 8.24 were visible even without optical magnification we performed a similar heating experiment in the UHV system where a sample with capped DIP film was mounted on the heater of the manipulator

and the sample was heated up to 300 °C. Then a camera was taking pictures through a glas window in the UHV sytsem.

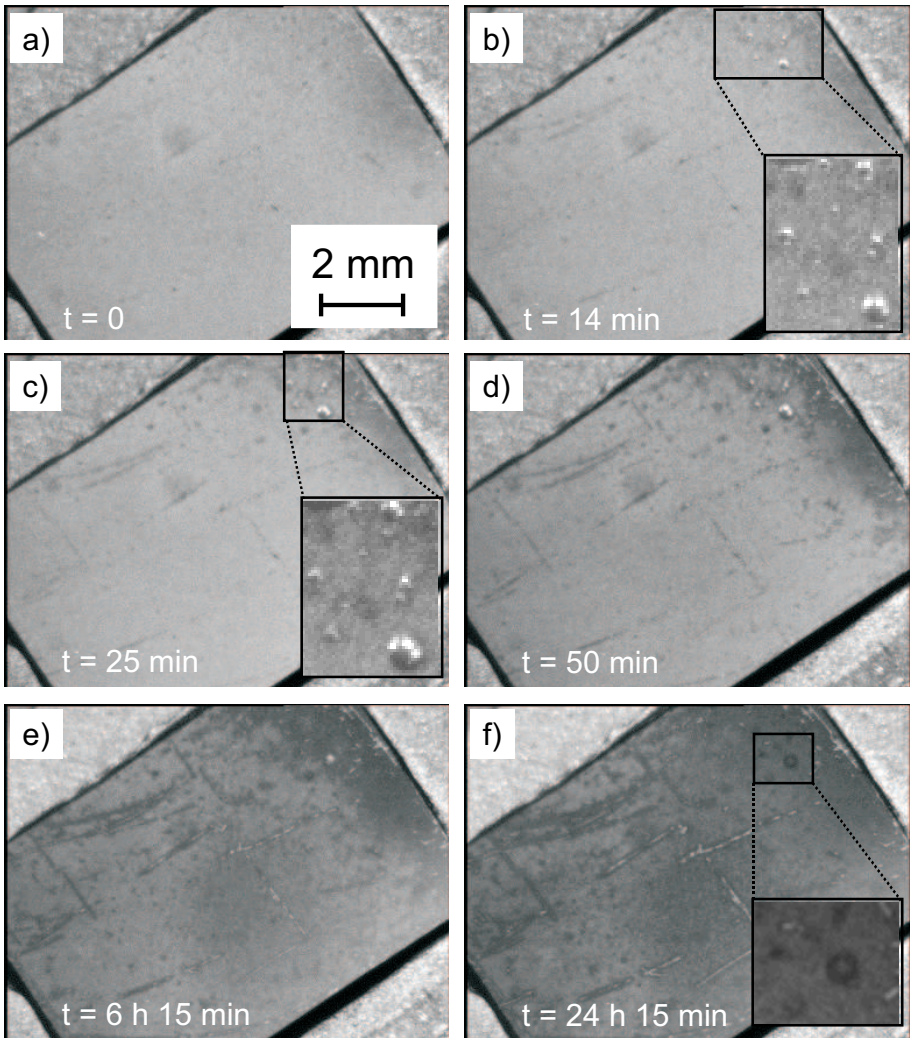

Figure 8.26: Series of photographs of a capped DIP film taken within 24 h at 300 °C. (a) Photograph when reaching 300 °C, (b) small 'bubbles' form (see inset) which evolve (c,d) and finally collapse (e,f). Furthermore, cracks form and evolve during heating.

The formation of these defects could be observed on a time scale of ca. 24 hours. The photographs in Fig. 8.26(a-f) show the sample at T = 300 °C and t = 0 (a) and the formation of 'bubbles' (b-d) which increase in size and collapse at some point. Parallel to the evolution of these 'bubbles' streaks on the sample become more distinct and

broader during this period.

After the heating process we investigated the sample surface by optical microscopy. Figure 8.27(a) shows one of the streaks from Fig. 8.26 which can be identified as cracks of ca. 20 μm in width and several 100 μm in length. Figure 8.27(b) shows some of the 'bubbles' in the capping layer some of which again have a red spot in the center which might come from the red color of the DIP molecules.

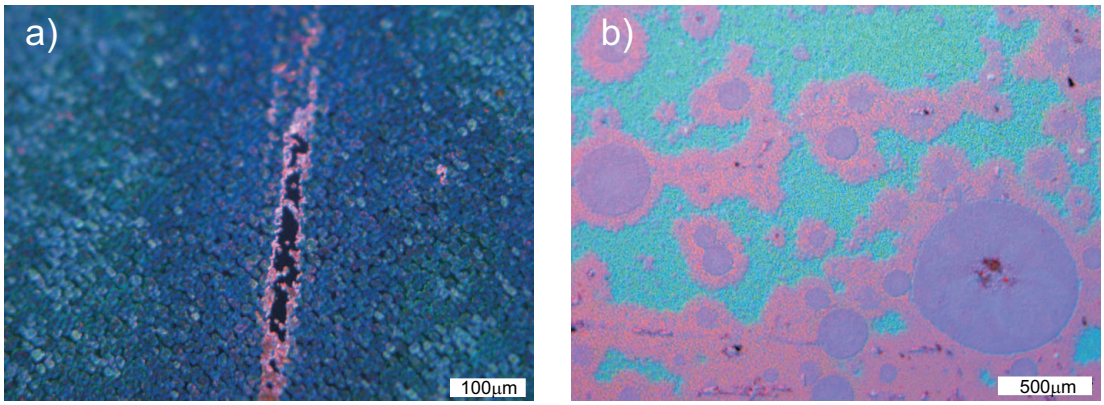

Figure 8.27: Optical micrographs of a crack (a) and of collapsed 'bubbles' (b) in the aluminum oxide capping layer after heating the sample at 300 °C for 24 h.

The origin of the voids in the capping layer is not yet clear. Possibly, local areas of higher metallic content might act as thermal weak spots in the capping layer. At higher temperatures the metal in such local areas would be more mobile and the capping layer might break through at its weakest spot. Parallel to the formation of these cavities the formation of cracks has also been observed which seems to have a different origin as for example the strong mismatch in the thermal expansion of the aluminum oxide and the DIP film as was shown in the previous section.

8.7.3 Surface and interface characterization of capped DIP films after thermal cycling

DIP films capped with an aluminum oxide layer were characterized before and during thermal cycling. Here, the surface and interfaces of the samples after the heating process are characterized by optical microscopy, AFM and TEM techniques. Figure 8.28 shows optical micrographs of four samples after the *in-situ* XRD studies. The surfaces exhibit relatively large features with different shapes.

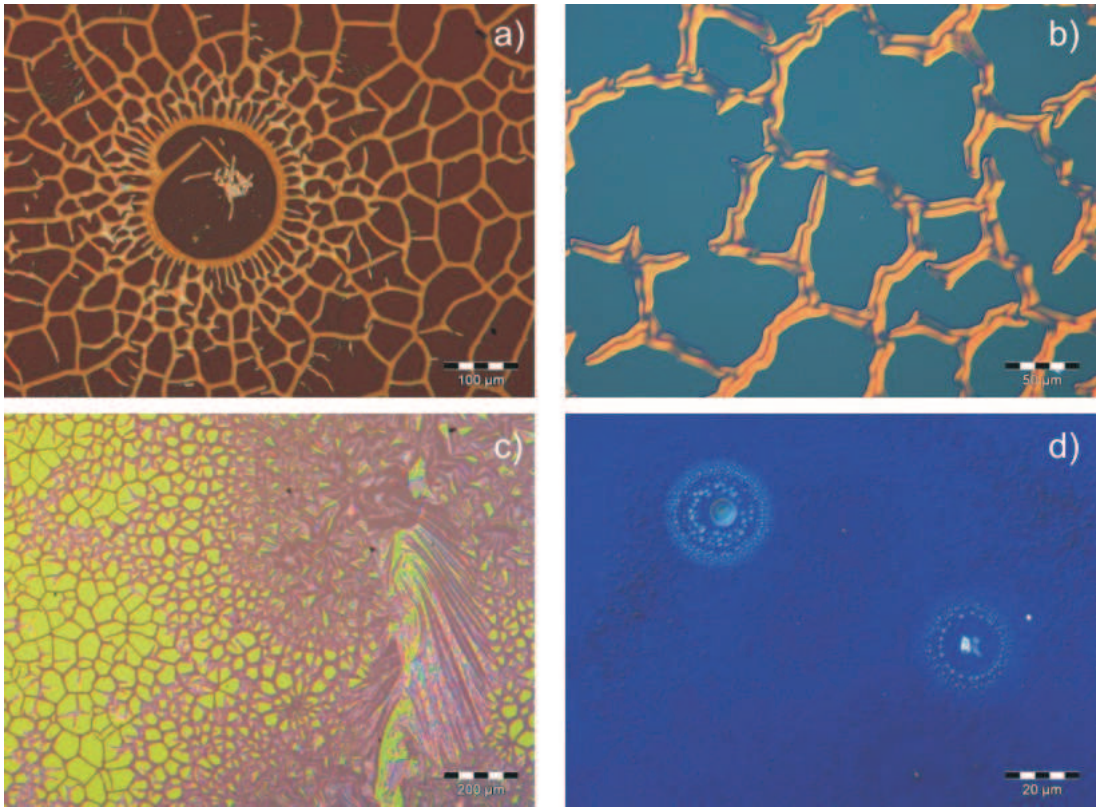

Figure 8.28: Optical micrographs of four capped DIP films taken after the heating process.

Generally, networks of extrusions as in Fig. 8.28(a-c) but also circular shaped structures as already seen in Figs. 8.25 and 8.27 are frequently found.

Morphology of annealed samples

The surface structures of the samples from Fig. 8.28 were too large to be analyzed with the AFM in the UHV system (the piezoelectric compounds accessible did not allow to go beyond scan areas of $5 \times 5\,\mu$m). Therefore, the AFM measurements were performed on an AFM system situated in air which was equipped with an optical microscope to place the AFM tip on a specific position on the sample. This allowed us to scan over the different features on the samples. The AFM was working in the tapping mode and scan ranges up to $15\,\mu$m were possible.

In Fig. 8.29 the numbered spots in the optical micrograph (a) indicate the scan regions where the AFM measurements (b,c) below were performed. Two areas were

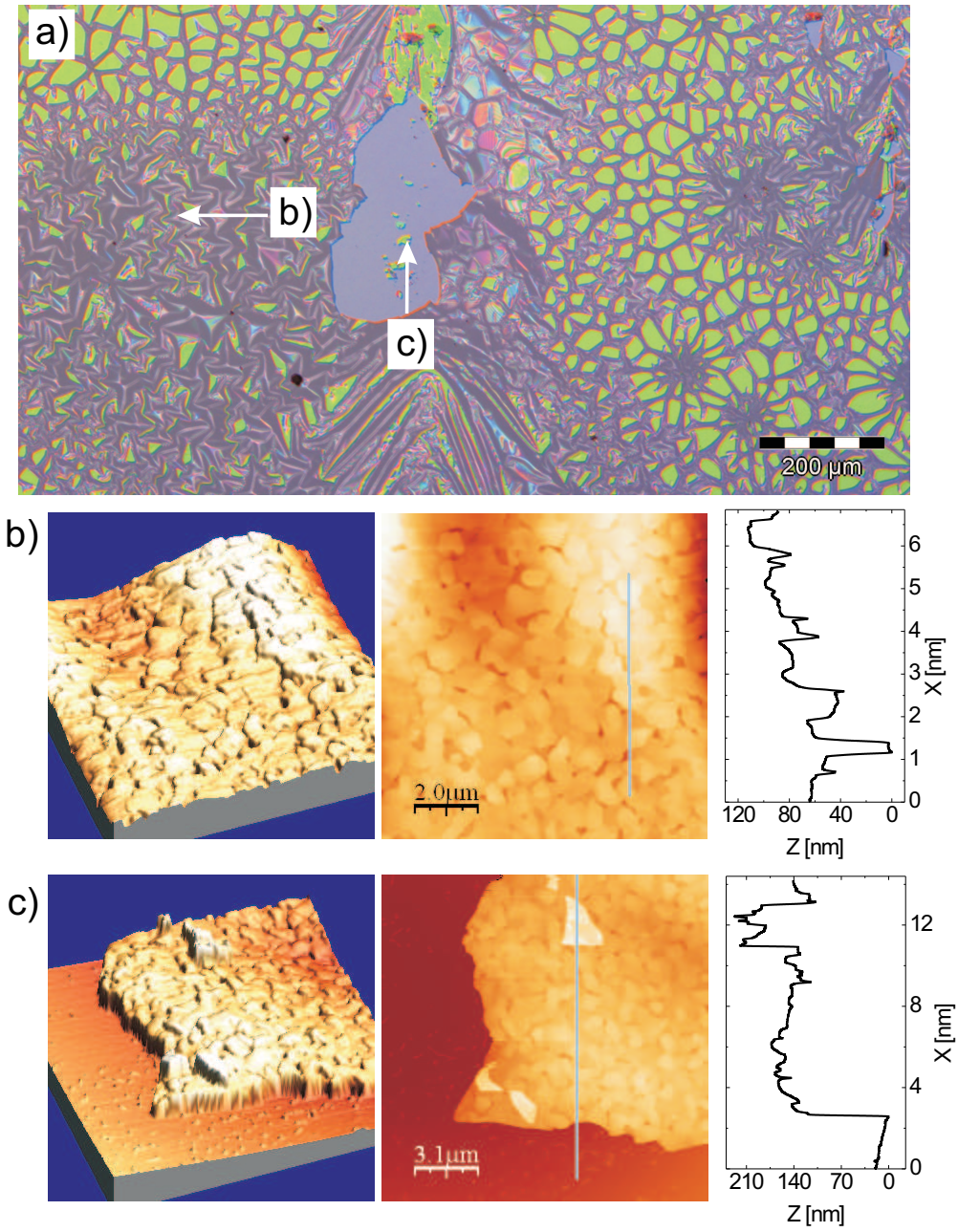

Figure 8.29: Optical micrograph (a) and AFM images (b,c) of heated samples. The AFM pictures were taken at representative spots indicated by the arrows in the optical micrograph.

selected which were representative. Scan area (b) was situated in a region which looked optically very rough and scan area (c) was situated in a region which seemed to show the bare silicon oxide substrate.

Indeed, the topographic image of scan area (b) in Fig. 8.29 reveals very large height differences. Furthermore, the whole scan area shows the same morphological characteristics as before heating (compare to Fig. 7.8(b)) and other scans (not shown here) show that except for a few spots the whole sample is still covered by an aluminum oxide film. To confirm this, the adhesion force of the AFM was increased and several scans were performed on the same spot. Usually, for weakly bound organic molecules the tip of the contact mode AFM then scratches the surface which can be seen in the AFM image lateron but no evidence for such a behavior was found.

The scan region (c) in Fig. 8.29 shows a spot on the sample where the aluminum oxide layer was missing and the bare silicon oxide substrate can be seen. The AFM image shows a region on the sample where both the silicon oxide and the aluminum oxide on DIP can be seen. The profile scan along the line in Fig. 8.29 (c) shows the transition from silicon oxide to aluminum oxide on DIP. The increase in height of about 150 nm corresponds to the total film thickness of ca. 50 nm aluminum oxide on 100 nm DIP. When the line crosses the brighter area in Fig. 8.29 (c) the height increases again for about 50 nm suggesting that this brighter area is a part of the aluminum oxide layer which has blown off and dropped on this spot. The DIP underneath has desorbed.

8.7.4 Thermal behavior of the inorganic/organic interface

We have seen that the surface of the Al_2O_3/DIP samples has undergone severe changes upon heating. And it was concluded that the defects in the capping layer give rise to the desorption of the underlying DIP film.

The question then arises if this scenario can be observed with cross-sectional TEM. Therefore, a sample which was heated up to 410 °C within the *in-situ* XRD experiments was used. This sample showed the characteristic features as shown in Fig. 8.28(b) but only on one half of the sample while the other half of the sample seemed to be unchanged compared to the surface before heating. Figure 8.30 shows a cross-sectional TEM image of an Al_2O_3/DIP specimen which was heated up to 410 °C.

The upper part of the specimen originates from a region of the sample with the typical structures from Fig. 8.28(b) and for the lower part of the specimen a region of

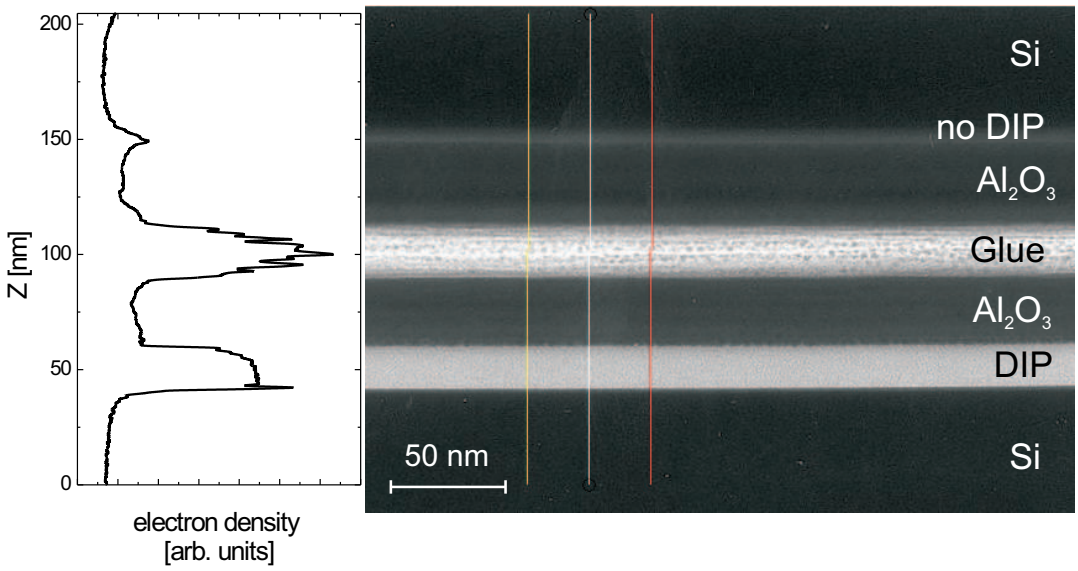

Figure 8.30: Cross-sectional TEM image of an Al_2O_3/DIP specimen which was heated up to 410 °C. The upper part of the specimen originates from a region of the sample with the typical structures from Fig. 8.28(b) and for the lower part of the specimen a region of the sample was used which did not show any of these features.

the sample was used which did not show any of these features.

The image clearly shows that on the upper half of the specimen (corresponding to the part of the sample with defects in the capping layer) only small remnants of DIP are left between the aluminum oxide and the silicon substrate while on the lower part of the sample (the part without visible defects) the DIP film is still there. Furthermore, the interface between Al_2O_3 and DIP is still laterally well-defined over a large length scale and no significant penetration of Al_2O_3 into the DIP film can be observed.

In none of the TEM images of this sample the DIP film showed the periodic structure coming from the molecular planes of DIP. This could be due to the fact that the DIP film has turned amorphous in some part of the sample while in other parts it has desorbed through defects.

8.8 Discussion

We presented a detailed study of the strong enhancement of the thermal stability of organic thin films of DIP encapsulated by sputtered aluminum oxide layers [14]. Since the multilayer structure obviously depends strongly on the preparation conditions, the enhancement of the thermal stability will also vary accordingly. The influence of different parameters (capping layer thickness, stoichiometry and heating rate) on the thermal stability of capped DIP films and their eventual breakdown were investigated [15]. It turned out that thick and stoichiometric capping layers and low heating rates are promoting the thermal stability of the capped films. Under optimized encapsulation conditions the organic films could be stabilized up to temperatures more than 200 °C above the 'bulk' desorption temperature of uncapped films at ∼190 °C. Moreover, the capped organic films retain their crystalline order at these elevated temperatures, where they would normally (i.e. uncapped) be in the vapor phase. The laterally well-defined interface between the Al_2O_3 and the DIP film even at elevated temperatures suggests that the overall Al_2O_3/DIP/SiO_x heterostructure remained essentially unchanged during heating.

While an ideal capping layer is of course expected to suppress evaporation of the organic layer underneath, the remarkable finding is that, given the inevitable defects of real samples, the capping not only enhances the stability, but does so effectively.

8.8.1 Crystalline DIP beyond the bulk desorption temperature

The aluminum oxide capping layer surprisingly does not only prevent the desorption of the organic film but it also enhances the thermal stability of the crystalline structure of DIP at temperatures where it normally would be in a vapor phase. We note, that for DIP no liquid phase is found for uncapped films. However, the enhancement of the thermal stability of capped DIP films at first glance ressembles the melting point enhancement (by about 15 °C) of self-assembled monolayers (SAMs) capped by a PTCDA (perylenetetracarboxylic dianhydride) film as reported by Schreiber *et al.* [40]. They excluded a pressure-induced melting point enhancement as described by the Clausius-Clapeyron equation since the PTCDA capping layer cannot exert a significant pressure on the SAM. One explanation for the mechanism of the melting of the capped SAM system would be a reduction of the tilt angle of the molecules which would lead to an

increased volume (reduced film density) during the phase transformations. For the system Al_2O_3/DIP the situation is different since vertical and horizontal stresses induced by the different thermal expansion of the two materials act at their interface and the structural breakdown of the capped organic film is below the melting point of DIP.

For the capped DIP films no changes in the lattice distance (except for the thermal expansion) could be observed which means that the DIP film remains densely packed during the whole heating process and thus the phase transformation is kinetically hindered.

8.8.2 Description of the breakdown process

The oxide capping layer apparently is relatively near to the concept of a 'closed' layer and does not diffuse strongly upon deposition. It kinetically hinders the organic molecules from desorption. Nevertheless, the oxide-capped DIP films also ultimately break down. The detailed scenario of this process has been investigated to understand the microscopic mechanism of the breakdown.

From the evaluation of long term effects of heating, it turned out that the integrated intensity of a sample kept at an intermediate temperature of 300 °C decreases with time – but still exhibits $\geq 50\,\%$ of its initial value after ~ 130 h – whereas the coherent thickness of the organic film remains unchanged over the entire period.

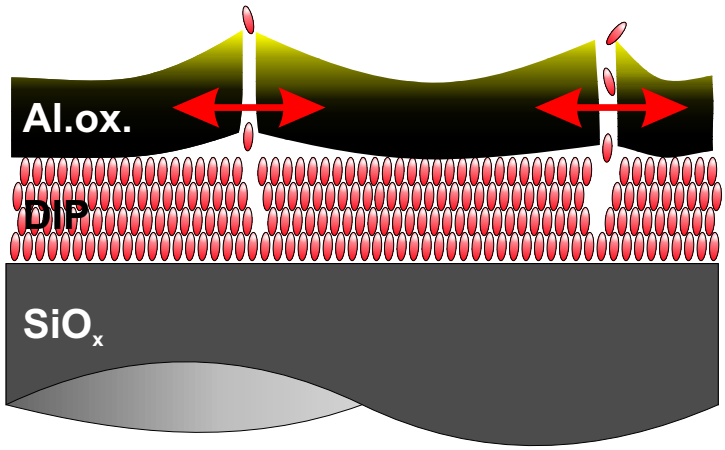

Figure 8.31: Sketch of the degradation scenario illustrating the experimental results.

This suggests that the observed degradation process of the capped DIP film is kineti-

cally limited by desorption from defects within the capping layer. However, a shortterm and a longterm contribution to the decay of the integrated intensity could be discerned indicating that the desorption mechanism is governed by two processes (Fig. 8.31).

Since the coherent thickness stays constant, the decrease of the integrated intensity at a certain temperature with time is related to desorption of the organic film from areas near to the defects in the capping layer, *e.g.* microcracks or holes. This is consistent with the findings from TDS measurements where we considered the sharp peaks in the spectra of capped films to come from individual desorption channels such as small cracks or defects which give rise to a limited local desorption of the underlying organic film.

In a second step even molecules from well-capped domains diffuse to these defects as a function of temperature and time. This is the longterm effect of a laterally inhomogeneous desorption process.

8.8.3 Crack and defect formation and their dependence on the sample parameters

A thermal barrier film of course requires a good thermal stability at high temperatures including a stable crystal structure, correct stoichiometry, low impurity levels (*e.g.* argon), and a dense microstructure [137]. For working temperatures not exceeding 400–500 °C (as was the case in our experiments) amorphous aluminum oxide films are expected to be stable enough against phase transformations since they are even stable at higher temperatures [207, 208] which we also could not find in our experiements indicating that possible phase transformations as a source for the defects in the capping layer can be excluded.

So far, we may speculate that these cracks or defects are thermally induced since no significant desorption was detected with TDS in a temperature range of $\Delta T \geq 50\,\mathrm{K}$ (depending on the heating rate and the capping layer thickness) above the desorption temperature of uncapped DIP films.

The formation of defects or cracks in a film depends strongly on the total stress in a film which is the sum of the external applied stresses (such as thermal stress) and the internal or residual stresses. Even without any external loading virtually all types of thin films are expected to contain some amount of residual stress decisively influencing

their mechanical behavior.

Materials possess an intrinsic collection of structural flaws such as voids, porosity, interconnected voids or porosity, voided or grooved grain boundaries, local regions of deadhesion, etc. Under either external or residual internal stressing, each flaw will locally concentrate stress and the surrounding material will tend to deform. If the stresses are sufficiently large, they can ultimately destroy the coating by crack propagation if tensile, and by wrinkling or buckling if compressive [118].

Generally, the residual stresses in thin films result from the film growth procedure with specific *intrinsic* (growth) and *extrinsic* (thermal) stress contributions, respectively. It is supposed that the intrinsic stresses are predetermined by the deposition technique, while extrinsic stresses originate from the mismatch of thermal expansion coefficients between substrate and thin film. The thermal stress in a film-substrate compound is given by,

$$\sigma = \frac{E_f}{1-\nu_f}(\Delta\alpha\Delta T), \tag{8.2}$$

where E_f, ν_f are the Young modulus and Poisson's ratio and $\Delta\alpha$ is the difference in the thermal expansion coefficient between film and substrate.

Films and coatings desposited by sputtering at low substrate temperature are often found in state of compressive stress which is caused by the atomic bombardment of the film by energetic species in a process called 'atom peening' [145–147] which causes atoms to be incorporated in the growing film with a density higher than would be obtained otherwise since with sufficient energy atoms may be forced into spaces too small to accomodate them under thermal equilibrium conditions [190]. Recently, molecular dynamics simulations of sputtered thin films have been shown to support a mechanism in which the tight packing of film atoms around injected gas atoms leads to a high compressive stress [152].

Temperature effects in thin films

At elevated temperatures the intrinsic stresses may strongly change due to enhanced defect annealing, processes of recrystallization or even grain growth if the temperature is high enough. The growth stresses thus fall rapidly with temperature and also the diffusion of impurities into and out of the film is accelerated which can give rise to substantial stress changes. A lower content of entrapped argon in sputtered aluminum

oxide films was found for higher substrate temperatures and this effect was explained by the decrease in sticking probability of inert sputter gas with increasing temperature [137].

A measure of the fracture susceptibility of a film is given by the thermal shock parameter S_T which can be derived from the heat transfer, $Q = -\kappa(\Delta T/\Delta x)$, and the thermal stress, (Eq. 8.2) [118]. The heat flux Q is given by the product of the thermal conductivity κ and the temperature difference accross the film thickness Δx. Elimination of ΔT yields

$$S_T^{-1} = \frac{\sigma}{Q\Delta x} = \frac{E\Delta\alpha}{(1-\nu)\kappa}. \tag{8.3}$$

Therefore, for a given thermal flux through a coating of thickness Δx, the stress develops is inversely proportional to the thermal shock parameter. Ceramic oxides have the lowest S_T values and are thus most prone to fracture by thermal shock.

At elevated temperatures films frequently display a number of time-dependent deformation processes characterized by the thermally activated motion of atoms and defects. Such stress and strain relaxation effects may also occur simultaneously. Film strains can be relaxed by several possible strain relaxation mechanisms. The rate of relaxation for each mechanism is generally strongly dependent on the film stress and temperature, and the operative or dominant mechanism is the one that relaxes strain the fastest [118].

Stoichiometry of the capping layer

The increase of the thermal stability (by up to 300 °C) in our experiments must be compared with, *e.g.*, metal capping layers which diffuse at low temperatures and tend to compromise the organic layer already upon deposition. The amorphous aluminum oxide is less prone to diffusion than gold, so that even at elevated temperatures the capping layer presumably does not 'move' much, in contrast to gold, which has a significant mobility at the temperatures relevant to this study.

For accidentally non-stoichiometric aluminum oxide layers, specifically those with higher metal content, the DIP film structure broke down at temperatures in between 190 °C and 500 °C. We take this as an indication of the metal atoms with their higher mobility being responsible for the weaker stabilization effect at elevated temperatures.

Generally, less stoichiometric films should contain higher densities of defects. For measurements of the electrical breakdown fields of sputtered aluminum oxide films it

was found that films with Al/O ratios < 0.59 have breakdown fields far exceeding those with less oxygen rich composition [139]. The explanation for this behavior was that until there is a sufficient excess of oxygen in the film, there is a sufficient number of aluminum rich defects present to act as 'randomly distributed weak spots' [209]. Due to their higher mobility at elevated temperatures these aluminum rich defects might also act as 'weak spots' with respect to the thermal stability of aluminum oxide capping layers.

Capping layer thickness

Thicker aluminum oxide capping layers were more effective in producing a higher thermal stability (at least up to thicknesses of 6000 Å) which could be caused by a better suppression of defects or a better relaxation of stresses compared to thin capping layers. On the other hand, according to Weibull, the probability of incorporating a fatal defect in a sample which may lead to cracks in the film increases for thicker films. Of course, a certain capping layer thickness is required to guarantee a closed barrier. From our measurements it turned out that aluminum oxide capping layers with a thickness of 166 Å are already very effective. However, compared to thicknesses of typical coatings (from some to tens and even hundreds of microns) our capping layers were rather thin.

8.8.4 Microscopic breakdown mechanism

The interpretation of the experimental results yielded a laterally inhomogeneous desorption process by defects in the capping layer as illustrated in Fig. 8.31. The DIP lattice parameters showed a complex non-linear thermal behavior which could be interpreted in terms of thermal expansion and relaxation effects. Especillay, the small thermal expansion of the in-plane lattice parameters up to 150 °C (in the order of the thermal expansion of aluminum oxide) and its strong increase beyond this temperature might be a hint for the formation of cracks in the capping layer due to the thermal stresses acting between the DIP film and the aluminum oxide capping layer. Once a network of cracks has formed in the capping layer, the organic film might expand more freely.

Furthermore, the origin of the observed bubbles in the capping layer might come from entrapped argon or sublimed DIP which could desorb due to voids at the

Al_2O_3/DIP interface. Parfitt *et al.* [189] concluded from their measurements that it is unlikely that gas-filled bubbles are the primary source of stress since their measured stresses and their dependence on gas content were inconsistent with model predictions. However, these measurements were not conducted at elevated temperatures were inert gases and other impurities might be very mobile.

It is not easy to identify a simple microscopic mechanism driving the eventual breakdown. Nevertheless, certain scenarios can be discussed. One possible mechanism of the breakdown scenario which we could derive from our results is related to the large mismatch in the thermal expansion at the Al_2O_3/DIP interface. The optical micrograph in Fig. 8.32(a) shows a sample for which the DIP was deposited with a shadow mask and afterwards aluminum oxide was deposited without mask. Note, that the cracks were only located on the Al_2O_3/DIP/SiO_x and not on the Al_2O_3/SiO_x.

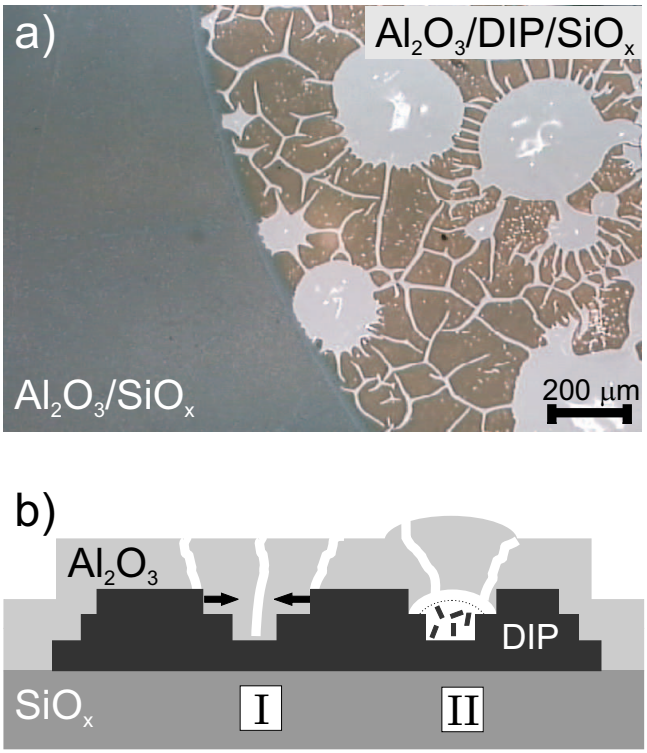

Figure 8.32: (a) Optical micrograph showing an extended network of cracks in the aluminum oxide capping layer which is limited to the region where the organic film was located underneath. (b) Possible breakdown mechanisms I and II.

The terrace structure of DIP films leads to lateral stress acting on the aluminum oxide which increases with the DIP layer number (starting from the first monolayer) since the size of the terraces decreases and it leads to vertical stress acting on the aluminum oxide which increase with the DIP layer number. The large mismatch between the thermal expansion of the aluminum oxide and the DIP films and possible relaxations of stresses finally lead to a strain-induced crack formation in the aluminum oxide layer when the temperature is increased. These thermally induced defects allow the desorption of DIP molecules located under these defects. And in a second step even molecules from well-capped areas diffuse to the defects to desorb from there. This scenario (I) would assume a failure of the aluminum oxide capping layer due to the thermomechanical mismatch between the different materials. Nevertheless, a second sceanrio (II) could also be drawn which is based on a secondary failure of the capping layer. During the aluminum oxide sputtering some voids may have formed between the aluminum oxide and the DIP film which allow a local desorption of DIP when heated above the desorption temperature. The partial pressure in this cavities might increase and expand the 'bubbles' which increases stress in the aluminum oxide layer and possible crack formation and desorption, accordingly.

8.8.5 Conclusions

The evidence for the enhanced thermal stability is of great practical importance, not only for the specific system of DIP studied here, but for organic electronics in general. It offers a route for the stabilization of compounds with vapor pressures so far considered too high for utilization in organic-based devices [17], thus extending the range of applications and working conditions, including harsher environments and elevated operation temperatures, up to the thermal degradation of the molecules. The electrical characterization of capped semiconductors was recently investigated for the more prominent molecule of pentacene [16]. It turned out that organic FETs with a pentacene film could be operated up to 150 °C (60 K above the desorption temperature of uncapped pentacene films) and that the limiting factor for the device performance was not given by the thermal stability of the capped pentacene films but by the diffusion of the gold contacts.

9 Summary

The aim of this thesis was to study interfaces of the organic semiconductor diindenoperylene (DIP) with metals and insulators, and to study the potential of sputtered aluminum oxide layers as encapsulation material for organic devices such as organic light emitting diodes (OLEDs) or organic field-effect transistors (OFETs).

The preparation and structural characterization of aluminum oxide layers deposited on top of DIP films and the thermal stability of these heterostructures was in the focus of this work.

For the application in OFETs the structural order is essential for good performances. Therefore, the growth, structure and morphology of different organic films was studied by means of X-ray diffraction (XRD) and atomic force microscopy (AFM). *In-situ* real-time growth experiments of DIP on silicon oxide have shown to provide valuable informations on the growth process of organic films.

Before depositing aluminum oxide on top of such organic films which have a relatively rough surface, the sputtering parameters had to be optimized to minimize the impact of the sputtering process on the DIP film structure. Furthermore, the oxide layers were deposited first on silicon oxide to study the growth, structure and morphology of these films. As a comparison to the deposition of aluminum oxide layers on DIP the real-time growth of thin gold films on top of DIP was studied.

9.1 Organic semiconductor films on silicon oxide

The structure of DIP films was studied in detail in recent works [11,57]. Here, we studied the influence of low substrate temperatures on the structure of DIP films and compared it to the properties of DIP films prepared under optimized conditions. From *in-situ* real-time X-ray diffraction measurements at the 3/2-anti-Bragg condition the influence of different preparation conditions (*i.e.*, different deposition rates and substrate tem-

peratures) on the film growth was studied. The growth oscillations resulting from the alternating destructive and constructive interferences between X-rays scattered from different layers of the growing film could be used to evaluate the growth mode of the organic films. Only minor differences where observed between the films prepared at the same substrate temperature but at different deposition rates. Films deposited at high substrate temperatures (ca. 132 °C) revealed seven or more oscillations corresponding to more then 13 monolayers of DIP while for the low-substrate samples (ca. 35 °C) the growth-oscillations were damped out after 5 monolayers which indicated incoherent growth of the organic film (islands). This observation is in agreement with the high film roughness produced by the island growth at low substrate temperatures as observed from as-prepared samples deposited at T = -90 °C and -160 °C and from the specular X-ray reflectivity curves taken at the samples after film growth.

The quantitative analysis of these and other *in-situ* real-time growth data require extensive modelling and can be found in the forthcoming thesis of S. Kowarik [183].

9.2 Comparison between aluminum oxide films deposited on silicon oxide and on DIP films

Aluminum oxide films were prepared by r.f. magnetron sputtering in a pure argon atmosphere to prevent oxidation of the organic film. To learn something about the growth and structure of these aluminum oxide films they were sputtered first on silicon wafers. Films of different thicknesses were analyzed by AFM and X-ray diffraction. The films exhibited a granular morphology of low roughness. The film roughness as a function of the film thickness could be used to calculate the growth exponent for aluminum oxide and $\beta = 0.37$ was obtained. Furthermore, the electron density was found to be around 80 % of the bulk material value.

The use of aluminum oxide films as a capping layer for the application in organic devices requires that the aluminum oxide does not diffuse strongly into the organic film when deposited on top. Furthermore, the crystalline structure of the underlying organic film has to be preserved. Herefore, the preparation of aluminum oxide layers on top of DIP films had to be optimized. These hybrid-structures were investigated with X-ray diffraction, AFM, and cross-sectional transmission electron microscopy (TEM). The data showed that aluminum oxide forms a laterally well-defined interface with the

DIP film and only little diffusion into the organic film was observed. Furthermore, even individual monolayers of DIP could be resolved by the TEM measurements confirming the high structural quality of these samples. The aluminum oxide layers were completely amorphous.

For the deposition of sputtered aluminum oxide films on silicon oxide and on DIP films a comparitive study of the roughness evolution with the film thickness according to $\sigma = L^{\beta}$ was performed. For aluminum oxide films sputtered on silicon oxide a growth exponent of $\beta = 0.37$ was obtained. The alumium oxide films deposited on thin DIP films exhibited a comparable growth exponent of $\beta = 0.34$. The similar growth exponents β and the AFM images of the Al_2O_3/SiO_x and Al_2O_3/DIP systems suggest that the growth and structure of aluminum oxide on these very different substrates exhibits similarities [13].

As a comparison to the deposition of aluminum oxide on DIP films the *in-situ* real-time growth of gold on DIP was studied by X-ray diffraction. Therefore, specular as-well as off-specular and transverse scattering data were recorded during deposition. On first glance, the data do not show a significant difference which could be due to the low deposition rate (0.025 Å/min) achieved with the e-beam evaporator in the portable UHV chamber. Due to the small temperature window between evaporation and melting of the gold rods, no high deposition rates could be obtained as would have been required to minimize diffusion of gold into the organic film. Nevertheless, small differences could be observed and the best fitting model considered only a DIP film with slightly increasing electron density. No gold layer has formed on top of the DIP and we believe that gold has diffused into the organic film where it is distributed homogeneously over the entire DIP film thickness.

9.3 Thermal stability of capped DIP films

The well-defined character of the aluminum oxide/DIP samples encouraged us to study the thermal stability of these systems. Surprisingly, the thermal stability of the DIP films could be strongly enhanced by more than 200 °C (compared to the desorption temperature of uncapped DIP films) [14]. This strongly enhanced thermal stability is due to the aluminum oxide layer serving as an almost perfect 'lid' for the DIP.

Nevertheless, the film structure breaks down at temperatures specific for each sample and the crucial question arose what was limiting the aluminum oxide perfection and which effects finally led to the eventual breakdown. We therefore performed a detailed study of the parameters which influence the thermal stability of organic films of DIP capped by an aluminum oxide layer [15].

From TDS and X-ray diffraction measurements it turned out that the stability can be further enhanced by using thicker aluminum oxide layers. The heating rate also plays a role for relaxation processes which compete with the thermally induced stress at the aluminum oxide/DIP interface. Since the thermomechanical properties of the aluminum oxide layers change with its composition the stoichiometry of the capping layer plays a major role in the breakdown scenario. From our results we conclude that thicker capping layers and low heating rates are more favorable for the high-temperature stability and metal-rich capping layers tend to break down at lower temperatures compared to stoichiometric (Al_2O_3) capping layers.

For the eventual breakdown of the capped film structure we presented a possible scenario based on the failure of the aluminum oxide capping layer due to thermally induced crack formation and subsequent desorption of the organic molecules.

We believe that the use of aluminum oxide layers as an encapsulation material has significant potential for the application in organic devices. Capping layers do not only prevent molecules from the organic layer to desorb at elevated temperatures but they also promise to prevent ambient gases from penetration into the organic semiconductor film. This is not only valid for the specific molecule of DIP but was also shown to work for more popular molecules such as pentacene [16]. One might therefore also think about using organic semiconductor molecules which have desorption temperatures so far considered too low for practical application [17]. Besides the practical use of a capping layer we point out that a capping layer allows to study material properties beyond the desorption temperature of the specific molecule and thus to study the behavior under conditions otherwise inaccessible.

A Properties of aluminum oxide

A.1 The different phases of aluminum oxide

Several metastable polymorphic forms of aluminum oxide are known [207] and the formation of these phases depends upon the processing techniques and conditions. These include the thermodynamically stable α-Al_2O_3 phase (hexagonal, or corrundum), γ (cubic spinel), δ (tetragonal), θ (monoclinic), η (cubic spinel), κ (orthorombic), χ (cubic), β (hexagonal) and ι. Various routes of the phase transformation sequence are reported [207, 210–215], for example, a commonly reported transformation sequence for PVD deposited films is amorphous $\rightarrow \gamma \rightarrow (\theta + \delta) \rightarrow \alpha$, in which the transformation products at each stage may be a mixture of several phases [138].

The deposition technique and the substrate temperature during deposition of aluminum oxide have a strong impact on which of the phases forms. Bolt *et al.* [135] have studied the effect of the substrate temperature during deposition and they found that films deposited below 300°C were amorphous, at 400-750°C the γ-Al_2O_3 was dominant, α-Al_2O_3 was deposited at 800°C (with an applied bias voltage of -300 V). Furthermore, it was found that r.f. magnetron sputtered amorphous aluminum oxide films are relatively resistant to crystallization [207]. Brüesch *et al.* [208] reported that r.f. diode sputtered amorphous alumina films started to crystallize at 750°C.

Obviously, the film properties of aluminum oxide differ strongly between the different phases due to their crystalline structure. But also the deposition parameters of each technique have a strong influence on the film formation and therefore also on the film properties. A detailed survey of the different alumina phases and their properties can be found in [37].

List of Figures

List of Tables

Bibliography

[1] A. Pochettino, Atti Acad. Lincei Rend. **15(1)**, 355 (1906).

[2] A. Pochettino, Atti Acad. Lincei Rend. **15(2)**, 171 (1906).

[3] M. Pope and C. E. Swenberg, *Electronic Processes in Organic Crystals and Polymers* (Oxford University Press, Clarendon, Oxford, 1999).

[4] *Physics of Organic Semiconductors*, edited by W. Brütting (Wiley-VCH, Weinheim, 2005).

[5] G. Horowitz, J. Mater. Res. **19**, 1946 (2004)
Organic thin film transistors: From theory to real devices.

[6] S. R. Forrest, Nature **428**, 911 (2004)
The path to ubiquitous and low-cost organic electronic appliances on plastic.

[7] C. D. Dimitrakopoulos and P. R. L. Malenfant, Adv. Mater. **14**, 99 (2002)
Organic thin film transistors for large area electronics.

[8] A. Dodabalapur, J. Laquindanum, H. E. Katz, and Z. Bao, Appl. Phys. Lett. **69**, 4227 (1996)
Complementary circuits with organic transistors.

[9] H. E. A. Huitema, G. H. Gelinck, J. B. P. H. van der Putten, K. E. Kuijk, C. M. Hart, E. Cantatore, P. T. Herweg, A. J. J. M. van Breemen, and D. M. de Leeuw, Nature **414**, 599 (2001)
Plastic transistors in active-matrix displays.

[10] J. R. Sheats, H. Antoniadis, M. Hueschen, W. Leonard, J. Miller, R. Moon, D. Roitman, and A. Stocking, Science **273**, 884 (1996)
Organic Electroluminescent Devices.

[11] M. Münch, Ph.D. thesis, Universität Stuttgart, 2001.

[12] A. C. Dürr, F. Schreiber, M. Münch, N. Karl, B. Krause, V. Kruppa, and H. Dosch, Appl. Phys. Lett. **81**, 2276 (2002)
High structural order in thin films of the organic semiconductor diindenoperylene.

[13] S. Sellner, A. Gerlach, S. Kowarik, F. Schreiber, N. Kasper, H. Dosch, S. Meyer, J. Pflaum, and G. Ulbricht, submitted (2005)
Roughness evolution of sputtered aluminum oxide films on organic and inorganic substrates.

[14] S. Sellner, A. Gerlach, F. Schreiber, M. Kelsch, N. Kasper, H. Dosch, S. Meyer, J. Pflaum, M. Fischer, and B. Gompf, Adv. Mater. **16**, 1750 (2004)
Strongly enhanced thermal stability of crystalline organic thin films induced by aluminum oxide capping layers.

[15] S. Sellner, A. Gerlach, F. Schreiber, M. Kelsch, N. Kasper, H. Dosch, S. Meyer, J. Pflaum, M. Fischer, B. Gompf, G. Ulbricht, H. Paulus, and W. Bolse, J. Mater. Res. **21**, 455 (2006)
Mechanisms for the enhancement of the thermal stability of organic thin films by aluminum oxide capping layers.

[16] S. Meyer, S. Sellner, F. Schreiber, H. Dosch, G. Ulbricht, M. Fischer, B. Gompf, and J. Pflaum, submitted (2005)
Operating aluminum oxide-capped pentacene thin film transistors at elevated temperatures.

[17] J. Niemax, A. K. Tripathi, and J. Pflaum, unpublished .

[18] H. Hoppe and N. S. Sacriciftci, J. Mater. Res. **19**, 1924 (2004)
Organic solar cells: An overview.

[19] K. M. Coakley and M. D. McGehee, Chem. Mater. **16**, 4533 (2004)
Conjugated Polymer Photovoltaic Cells.

[20] M. Berggren, A. Dodabalapur, R. E. Slusher, and Z. Bao, Synth. Met. **91**, 65 (1997)
Organic lasers based on Förster transfer.

[21] F. Garnier, R. Hajlaoui, A. Yassar, and P. Srivastava, Science **265**, 1684 (1994)
All-polymer field-effect transistor realized by printing techniques.

[22] J. A. Rogers, Z. Bao, M. Meier, A. Dodabalapur, O. J. A. Schueller, and G. M. Whitesides, Synth. Met. **115**, 5 (2000)
Printing, molding, and near-field photolithographic methods for patterning organic lasers, smart pixels and simple circuits.

[23] C. C. Cedeño, J. Seekamp, A. P. Kam, T. Hoffmann, S. Zankovych, C. M. S. Torres, C. Menozzi, M. Cavallini, M. Murgia, G. Ruani, F. Biscarini, M. Behl, R. Zentel, and J. Ahopelto, Microelectr. Eng. **61–62**, 25 (2002)
Nanoimprint lithography for organic electronics.

[24] W. Clemens, W. Fix, J. Ficker, A. Knobloch, and A. Ullmann, J. Mater. Res. **19**, 1963 (2004)
From polymer transistors towards printed electronics.

[25] A. C. Dürr, F. Schreiber, M. Kelsch, H. D. Carstanjen, and H. Dosch, Adv. Mater. **14**, 961 (2002)
Morphology and Thermal Stability of Metal Contacts on Crystalline Organic Thin Films.

[26] M. Scharnberg, J. Hu, J. Kanzow, K. Rätzke, R. Adelung, F. Faupel, C. Pannemann, U. Hilleringmann, S. Meyer, and J. Pflaum, Appl. Phys. Lett. **86**, 024104 (2005)
Radiotracer measurements as a sensitive tool for the detection of metal penetration in molecular-based organic electronics.

[27] R. Farchioni and G. Grosso, *Organic Electronic Materials* (Springer-Verlag, Berlin, 2001).

[28] F. Schreiber, Phys. Stat. Sol. (a) **201**, 1037 (2004)
Organic molecular beam deposition: Growth studies beyond the first monolayer.

[29] W. R. Salaneck, K. Seki, and J.-J. Pireaux, *Conjugated Polymer and Molecular Interfaces: Science and Technology for Photonic and Optoelectronic Applications* (Marcel Dekker, New York, 2002).

[30] P. Peumans, S. Uchida, and S. R. Forrest, Nature **425**, 158 (2003)
Efficient bulk heterojunction photovoltaic cells using small-molecular weight organic thin film.

[31] A. C. Dürr, F. Schreiber, M. Kelsch, H. D. Carstanjen, H. Dosch, and O. H. Seeck, J. Appl. Phys. **93**, 5201 (2003)
Morphology and interdiffusion behavior of evaporated metal films on crystalline DIP organic thin films.

[32] N. Koch, A. C. Dürr, J. Ghijsen, R. L. Johnson, J.-J. Pireaux, J. Schwartz, F. Schreiber, H. Dosch, and A. Kahn, Thin Solid Films **441**, 145 (2003)
Optically induced electron transfer from conjugated organic molecules to charged metal clusters.

[33] F. Faupel, R. Willecke, and A. Thran, Mat. Sci. Eng. C **R22**, 1 (1998)
Diffusion of metals in polymers.

[34] J. H. Lee, S. H. Kim, G. H. Kim, S. C. Lim, H. Lee, J. Jang, and T. Zyung, Synth. Met. **139**, 445 (2003)
Pentacene thin film transistors fabricated on plastic substrates.

[35] W. H. Ha, M. H. Choo, and S. Im, J. Non-Cryst. Sol. **303**, 78 (2002)
Electrical properties of Al_2O_3 film deposited at low temperatures.

[36] R. G. Munro, J. Am. Ceram. Soc. **80**, 1919 (1997)
Evaluated material properties for a sintered α-Alumina.

[37] W. H. Gitzen, *Alumina as a ceramic material* (The American Ceramic Society, Inc., Columbus, Ohio, 1970).

[38] X. Zhou, J. He, L. S. Liao, M. Lu, X. M. Ding, X. Y. Hou, X. M. Zhang, X. Q. He, and S. T. Lee, Adv. Mater. **12**, 265 (2000)
Real-Time Observation of Temperature Rise and Thermal Breakdown Process in Organic LEDs Using an IR Imaging and Analysis System.

[39] P. N. M. dos Anjos, H. Aziz, N.-X. Hu, and Z. D. Popovic, Organic Electronics **3**, 9 (2002)

Temperature dependence of electroluminescence degradation in organic light emitting devices without and with a copper phthalocyanine buffer layer.

[40] F. Schreiber, M. C. Gerstenberg, H. Dosch, and G. Scoles, Langmuir **19**, 10004 (2003)
Melting point enhancement of a self-assembled monolayer induced by an van der Waals bound capping layer.

[41] P. Fenter, F. Schreiber, V. Bulović, and S. R. Forrest, Chem. Phys. Lett. **277**, 521 (1997)
Thermally induced failure mechanisms of organic light emitting structures probed by X-ray specular reflectivity.

[42] B. Krause, A. C. Dürr, F. Schreiber, H. Dosch, and O. H. Seeck, J. Chem. Phys. **119**, 3429 (2003)
Thermal stability and partial dewetting of crystalline organic thin films: 3,4,9,10-perylenetetracarboxylic dianhydride on Ag(111).

[43] G. H. Kim, J. Oh, Y. S. Yang, L.-M. Do, and K. S. Suh, Thin Solid Films **467**, 1 (2004)
Lamination process encapsulation for longevity of plastic-based organic light-emitting devices.

[44] K. M. Kim, B. J. Jang, W. S. Cho, and S. H. Ju, **5**, 64 (2005)
The property of encapsulation using thin film multi layer for application to organic light emitting devices.

[45] J. von Braun and G. Manz, *Patent-Nr.: 595 024: Verfahren zur Herstellung von Kondensationsprodukten des Fluoranthens* (Deutsches Reichspatentamt, Berlin, 1934).

[46] I. C. Lewis and L. S. Singer, in *Further electron spin resonance studies of the pyrolysis of aromatic hydrocarbons* (Carbon, Pergamon Press Ltd., Great Britain, 1967), Vol. 5, pp. 373–381.

[47] L. J. E. Hofer and W. C. Peebles, Anal. Chem. (1951)
X-ray powder diffraction patterns of solid aromatic hydrocarbons.

[48] L. J. E. Hofer, W. C. Peebles, and E. H. Bean, *X-ray powder diffraction patterns of solid hydrocarbons, derivatives of hydrocarbons, phenols, and organic bases* (U.S Bureau of Mines, Bulletin 613, Washingtin, D.C., 1963).

[49] J. Pflaum, S. Hirschmann, W. Frey, and N. Karl, submitted (2005).

[50] R. Strohmaier, J. Petersen, B. Gompf, and W. Eisenmenger, Surf. Sci. **418**, 91 (1998)
A systematic STM study of planar aromatic molecules on inorganic substrates: I. Submolecular image contrast.

[51] A. C. Dürr, N. Koch, M. Kelsch, A. Rühm, J. Ghijsen, R. L. Johnson, J.-J. Pireaux, J. Schwartz, F. Schreiber, H. Dosch, and A. Kahn, Phys. Rev. B **68**, 115428 (2003)
Interplay between morphology, structure and electronic properties at diindenoperylene-gold interfaces.

[52] A. Hoshino, S. Isoda, and T. Kobayashi, J. Cryst. Growth **115**, 826 (1991)
Epitaxial growth of organic crystals on organic substrates polynuclear aromatic hydrocarbons.

[53] J. O. Ossó Torné, Ph.D. thesis, Universitat Autònoma de Barcelona, Institut de Ciència de Materials de Barcelona, - Max-Planck-Institut für Metallforschung, Stuttgart, Barcelona, 2004.

[54] N. Karl, in *Charge Carrier Mobility in Organic Molecular Crystals*, Vol. 41 of *Springer Series in Materials Science*, edited by R. Farchioni and G. Grosso (Springer, Berlin, 2001), Chap. 3.

[55] A. C. Dürr, F. Schreiber, M. Kelsch, and H. Dosch, Ultramicroscopy **98**, 51 (2003)
Optimized preparation of cross-sectional TEM specimens of organic thin films.

[56] A. C. Dürr, F. Schreiber, K. A. Ritley, V. Kruppa, J. Krug, H. Dosch, and B. Struth, Phys. Rev. Lett. **90**, 016104 (2003)
Rapid roughening in thin film growth of an organic semiconductor (Diindenoperylene).

[57] A. C. Dürr, Ph.D. thesis, Max-Planck-Insitut für Metallforschung - Institut für Theoretische und Angewandte Physik der Universität Stuttgart, Stuttgart, 2002.

[58] N. Karl, Synth. Met. **133–134**, 649 (2003)
Charge-carrier transport in organic semiconductors.

[59] M. Heilig, M. Domhan, and H. Port, J. Luminescence **110**, 290 (2004)
Optical properties and morphology of thin diindenoperylene films.

[60] J. M. Robertson, J. Chem. Soc. 615 (1935)
An X-Ray Study of the Structure of the Phthalocyanines. Part I. The Metal Free, Nickel, Copper, and Platinum Compounds.

[61] J. M. Robertson, J. Chem. Soc. 1195 (1936)
An X-ray study of the phthalocyanines. Part II. Quantitative structure determination of the metal-free compound.

[62] J. M. Robertson and I. Woodward, J. Chem. Soc. 219 (1937).

[63] S. Matsumoto, K. Matsuhama, and J. Mizuguchi, Acta Cryst. **C55**, 131 (1999)
β metal-free phthalocyanine.

[64] C. J. Brown, J. Chem. Soc. A. 2488 (1968)
Crystal Structure of β-Copper Phthalocyanine.

[65] R. D. Gould, Coord. Chem. Rev. **156**, 237 (1996)
Structure and electrical conduction properties of phthalocyanine thin films.

[66] S. M. Bayliss, S. Heutz, G. Rumbles, and T. S. Jones, Phys. Chem. Chem. Phys. **1**, 3673 (1999)
Thin film properties and surface morphology of metal free phthalocyanine films grown by organic molecular beam deposition.

[67] O. Berger, W.-J. Fischer, B. Adolphi, S. Tierbach, V. Melev, and J. Schreiber, J. Mat. Sci.: Mat. Electr. **11**, 331 (2000)
Studies on phase transformations of Cu-phthalocyanine thin films.

[68] Z. Bao, Adv. Mater. **12**, 227 (2000)
Materials and fabrication needs for low-cost organic transistor circuits.

[69] Z. Bao, A. J. Lovinger, and J. Brown, J. Am. Chem. Soc. **120**, 207 (1998)
New air-stable n-channel organic thin film transistor.

[70] J. O. Ossó, F. Schreiber, V. Kruppa, H. Dosch, M. Garriga, M. I. Alonso, and F. Cerdeira, Adv. Funct. Mater. **12**, 455 (2002)
Controlled molecular alignment in phthalocyanine thin films on stepped sapphire surfaces.

[71] E. Barrena, J. O. Ossó, F. Schreiber, M. Garriga, M. I. Alonso, and H. Dosch, J. Mater. Res. **19**, 2061 (2004)
Self-organization of phthalocyanines on $Al_2O_3(11\bar{2}0)$ in aligned and ordered films.

[72] R. Wyckoff, *Crystal structures* (John Wiley, New York, 1971).

[73] T. Minakata, H. Imai, M. Ozaki, and K. Saco, J. Appl. Phys. **72**, 5220 (1992)
Structural studies of highly ordered and highly conductive thin films of pentacene.

[74] R. Ruiz, D. Choudhary, B. Nickel, T. Toccoli, K.-C. Chang, A. C. Mayer, P. Clancy, J. M. Blakely, R. L. Headrick, S. Iannotta, and G. G. Malliaras, Chem. Mater. **16**, 4497 (2004)
Pentacene Thin Film Growth.

[75] E. A. Silinsh, *Organic Molecular Crystals. Their Electronic States* (Springer Verlag, Berlin, 1980).

[76] R. B. Campbell, J. M. Robertson, and J. Trotter, Acta Cryst. **15**, 289 (1962)
The crystal structure of hexacene, and a revision of the crystallographic data for tetracene.

[77] R. G. Della Valle, E. Venuti, A. Brillante, and A. Girlando, J. Chem. Phys. **118**, 807 (2003)
Inherent structures of crystalline pentacene.

[78] C. D. Dimitrakopoulos, A. R. Brown, and A. Pomp, J. Appl. Phys. **80**, 2501 (1996)
Molecular beam deposited thin films of pentacene for organic field-effect transistor applications.

[79] I. P. M. Bouchoms, W. A. Schoonveld, J. Vrijmoeth, and T. M. Klapwijk, Synth. Met. **104**, 175 (1999)
Morphology identification of the thin film phases of vacuum evaporated pentacene on SiO_2 substrates.

[80] Y. Y. Lin, D. J. Gundlach, and T. N. Jackson, in *High mobility pentacene organic thin film transistors* (IEEE Electron Devices Society, New York, 1996), Vol. 54th Annual Device Research Conference Digest, pp. 80–81.

[81] Y. Y. Lin, D. J. Gundlach, S. F. Nelson, and T. N. Jackson, IEEE Electr. Dev. Lett. **44**, 1325 (1997).

[82] D. J. Gundlach, Y. Y. Lin, T. N. Jackson, S. F. Nelson, and D. G. Schlom, IEEE Electr. Dev. Lett. **18**, 87 (1997)
Pentacene Organic Thin-Film Transistors - Molecular Ordering and Mobility.

[83] J. G. Laquindanum, H. E. Katz, A. J. Lovinger, and A. Dodabalapur, Chem. Mater. **8**, 2542 (1996)
Morphological Origin of High Mobility in Pentacene Thin-Film Transistors.

[84] D. F. Barbe and C. R. Westgate, J. Phys. Chem. Solids **31**, 2679 (1970).

[85] M. L. Petrova and L. D. Rozenshtein, Fiz. Tverd. Tela (Sov. Phys.-Solid State) **12**, 961 (1970).

[86] F. Ebisawa, T. Kurokawa, and S. Nara, J. Appl. Phys. **54**, 3255 (1983)
Electrical properties of polyacetylene/polysiloxane interface.

[87] A. Tsumura, K. Koezuka, and T. Ando, Appl. Phys. Lett. **48**, 1210 (1986)
Macromolecular electronic device: Field-effect transistor with a polythiophene thin film.

[88] G. Horowitz, D. Fichou, X. Z. Peng, Z. G. Xu, and F. Garnier, Solid State Commun. **72**, 381 (1989)
A field-effect transistor based on conjugated alpha-sexithienyl.

[89] P. K. Weimer, Proc. IRE **50**, 1462 (1962)
The TFT - a new thin film transistor.

[90] G. Horrowitz, Adv. Mater. **10**, 365 (1998)
Organic field-effect transistors.

[91] C. R. Newman, C. D. Frisbie, D. A. da Silva Filho, J.-L. Brédas, P. C. Ewbank, and K. R. Mann, Chem. Mater. **16**, 4436 (2004)
Introduction to Organic Thin Film Transistors and Design of n-Channel Organic Semiconductors.

[92] C. Dimitrakopoulos, S. Purushothaman, J. Kymissis, A. Callegari, and J. Shaw, Science **283**, 822 (1999)
Low-voltage organic transistors on plastic comprising high-dielectric constant gate insulators.

[93] N. Tessler and Y. Roichman, in *Organic Field Effect Transistors*, edited by J. C. deMello and J. J. M. Halls (Wiley and Son, New York, 2003).

[94] G. Horrowitz, R. Hajlaoui, H. Bouchriha, R. Bourguiga, and M. Hajlaoui, Adv. Mater. **10**, 923 (1998)
The concept of 'Threshold Voltage' in Organic Field-Effect Transistors.

[95] G. Horrowitz, R. Hajlaoui, D. Fichou, and A. El Kassmi, J. Appl. Phys. **85**, 3202 (1999)
Gate voltage dependent mobility of oligothiophene field-effect transistors.

[96] S. M. Sze, *Physics of Semiconductor Devices* (Wiley and Son, New York, 1981).

[97] T. Muck, V. Wagner, U. Bass, M. Leufgen, J. Geurts, and L. W. Molenkamp, Synth. Met. (2004)
In situ electrical characterization of DH4T field-effect transistors.

[98] R. W. I. de Boer, M. E. Gershenson, A. F. Morpurgo, and V. Podzorov, Phys. Stat. Sol. (a) **201**, 1302 (2004)
Organic single-crystal field-effect transistors.

[99] H. E. Katz, C. Kloc, V. Sundar, J. Zaumseil, and A. L. Briseno, J. Mater. Res. **19**, 1995 (2004)
Field-Effect transistors made from macroscopic single crystals of tetracene and related semiconductors on polymer dielectrics.

[100] J. Niemax, A. K. Tripathi, and J. Pflaum, Appl. Phys. Lett. **86**, 122105 (2005)
Comparison of the electronic properties of sublimation- and vapor-Bridgman-grown crystals of tetracene.

[101] S. R. Forrest, Chem. Rev. **97**, 1793 (1997)
Ultrathin organic films grown by organic molecular beam deposition and related techniques.

[102] G. Witte and C. Wöll, J. Mater. Res. **19**, 1889 (2004)
Growth of aromatic molecules on solid substrates for applications in organic electronics.

[103] F. Garnier, A. Yassar, R. Hajlaoui, G. Horowitz, and F. Deloffre, Electrochimica Acta **39**, 1339 (1994)
Control of the mesocopic organization of conjugated thiophene oligomers, induced by self-assembly properties.

[104] J. Bernstein, *Polymorphism in Molecular Crystals* (Oxford University Press, New York, 2002).

[105] T. W. Kelley and C. D. Frisbie, J. Phys. Chem. B **105**, 4538 (2001)
Gate voltage dependent resistance of a single organic semiconductor grain boundary.

[106] A. B. Chwang and C. D. Frisbie, J. Appl. Phys. **90**, 1342 (2001)
Temperature and gate voltage dependent transport across a single organic semiconductor grain boundary.

[107] G. Horowitz and M. E. Hajlaoui, Synth. Met. **122**, 185 (2001)
Grain size dependent mobility in polycrystalline organic field-effect transistors.

[108] F.-J. Meyer zu Heringdorf, M. C. Reuter, and R. M. Tromp, Nature **412**, 517 (2001)
Growth dynamics of pentacene thin films.

[109] M. Shtein, J. Mapel, J. B. Benziger, and S. R. Forrest, Appl. Phys. Lett. **81**, 268 (2002)

Effects of film morphology and gate dielectric surface preparation on the electrical characteristics of organic-vapor-phase-deposited pentacene thin-film transistors.

[110] S. Lukas, S. Vollmer, G. Witte, and C. Wöll, J. Chem. Phys. **114**, 10123 (2001)
Adsorption of Acenes on Flat and Vicinal Cu(111) Surfaces: Step Induced Formation of Lateral Order, .

[111] R. Schmechel and H. von Seggern, Phys. Stat. Sol. (a) **201**, 1215 (2004)
Electronic traps in organic transport layers.

[112] G. Horrowitz, M. E. Hajlaoui, and R. Hajlaoui, J. Appl. Phys. **87**, 4456 (2000)
Temperature and gate voltage dependence of hole mobility in polycrystalline oligothiophene thin film transistors.

[113] A. Dodabalapur, L. Torsi, and H. E. Katz, Science **268**, 270 (1995)
Organic Transistors: Two-Dimensional Transport and Improved Electrical Characteristics.

[114] F. Dinelli, M. Murgia, P. Levy, M. Cavallini, and F. Biscarini, Phys. Rev. Lett. **92**, 1168021 (2004)
Spatially Correlatred Charge Transport in Organic Thin film Transistors.

[115] J. A. Venables, *Surface and Thin Film Processes* (Cambridge University Press, Cambridge, United Kingdom, 2000).

[116] Alberto Pimpinelli and Jacques Villain, *Physics of Crystal Growth*, *Monographs and Texts in Statistical Physics* (Cambridge University Press, Cambridge, 1999).

[117] W. K. Burton, N. Cabrera, and F. C. Frank, Philosophical Transactions of the Royal Society of London. Series A, Mathematical and Physical Sciences **243**, 299 (1951)
The growth of crystals and the equilibrium structure of their surfaces.

[118] M. Ohring, *The Materials Science of Thin Films* (Academic Press, San Diego, California, 1992).

[119] R. W. Vook, Int. Metals Rev. **27**, 209 (1982)
Structure and growth of thin films (vacuum evaporation).

[120] R. Waser, *Nanoelectronics and Information Technology* (Wiley-VCH, Weinheim, 2005).

[121] H. Lüth, *Surfaces and Interfaces of Solid Materials* (Springer-Verlag, Heidelberg, 1995).

[122] B. A. Joyce, Rep. Prog. Phys. **48**, 1673 (1985)
Molecular beam epitaxy.

[123] M. A. Herman and H. Sitter, *Molecular Beam Epitaxy: Fundamentals and Current Status* (Springer, Berlin, 1996).

[124] R. Heckingbottom, in *Molecular Beam Epitaxy and Heterostructures*, edited by L. L. Chang and K. Ploog (Nijhoff, Dordrecht, 1985), (c).

[125] N. Karl and C. Günther, Cryst. Res. Technol. **34**, 243 (1999)
Structure and ordering principles of ultrathin organic molecular films on surfaces of layered semiconductors organic-on-inorganic MBE.

[126] G. K. Wehner and G. S. Anderson, in *Handbook of Thin Film Technology*, edited by L. I. Maissel and R. Glang (McGraw-Hill, New York, 1970), pp. 3.1–3.38.

[127] L. I. Maissel, in *Handbook of Thin Film Technology*, edited by L. I. Maissel and R. Glang (McGraw-Hill, New York, 1970), pp. 4.1–4.44.

[128] B. A. Movchan and A. V. Demchishin, Phys. Met. Metallogr. **28**, 83 (1969)
Investigations of the structure and properties of thick Ni, Ti, W, Al_2O_3 and ZrO_2 vacuum condensates.

[129] J. V. Sanders, in *Chemisorption and Reactions on Metallic Films* (Academic, London & New York, 1971), p. 555.

[130] J. A. Thornton, Ann. Rev. Mater. Sci. **7**, 239 (1977)
High rate thick film growth.

[131] Y. H. Sohn, R. R. Biederman, and R. Sisson Jr., Thin Solid Films **250**, 1 (1994)
Microstructural development in physical vapour-deposited partially stabilized zirconia thermal barrier coatings.

[132] S. Schiller, K. Goedicke, J. Reschke, V. Kirchhoff, and F. Milde, Surf. and Coatings Technology **61**, 331 (1993).

[133] F. Fietzke, K. Goedicke, and W. Hempel, Surf. and Coatings Technology **86–87**, 657 (1996)
The deposition of hard crystalline Al_2O_3 layers by means of bipolar pulsed magnetron sputtering.

[134] O. Zywitzki, G. Hoetsch, F. Fietzke, and K. Goedicke, Surf. and Coatings Technology **82**, 169 (1996).

[135] H. Bolt, F. Koch, J. L. Rodet, D. Karpov, and S. Menzel, Surf. and Coatings Technology **116–119**, 956 (1999)
Al_2O_3 coatings deposited by filtered vacuum arc characterization of high temperature properties.

[136] O. Zywitzki and G. Hoetzsch, Surf. and Coatings Technology **86–87**, 640 (1996)
Influence of coating parameters on the structure and properties of Al_2O_3 layers reactively deposited by means of pulsed magnetron sputtering.

[137] P. Vuoristo, T. Mäntylä, and P. Kettunen, Thin Solid Films **204**, 297 (1991)
Stoichiometry and impurities in sputtered alumina films on copper.

[138] T. C. Chou, T. G. Nieh, S. D. McAdams, and G. M. Pharr, Thin Solid Films **25**, 2203 (1991)
Microstructure and mechanical properties of thin films of aluminum oxide.

[139] C. S. Bhatia, G. Guthmiller, and A. M. Spool, J. Vac. Sci. Technol. A **7**, 1298 (1989)
Alumina films by sputter deposition with Ar/O_2: Preparation and characterization.

[140] K. Koski, J. Hölsä, and P. Juliet, Surf. and Coatings Technology **116–119**, 716 (1999)
Deposition of aluminium oxide thin films by reactive magnetron sputtering.

[141] K. Koski, J. Hölsä, P. Juliet, Z. H. Wang, R. Aimo, and K. Pischow, Mat. Sci. Eng. B **65**, 94 (1999)

Characterisation of aluminium oxide thin films deposited on polycarbonate substrates by reactive magnetron sputtering.

[142] K. Koski, J. Hölsä, and P. Juliet, Thin Solid Films **339**, 240 (1999)
Properties of aluminium oxide thin films deposited by reactive magnetron sputtering.

[143] B. M. Henry, A. G. Erlat, A. McGuigan, C. R. M. Grovenor, G. A. D. Briggs, Y. Tsukahara, T. Miyamoto, N. Noguchi, and T. Niijima, Thin Solid Films **382**, 194 (2001)
Characterization of transparent aluminium oxide and indium tin oxide layers on polymer substrates.

[144] J. Lee, S. S. Kim, and S. Im, J. Vac. Sci. Technol. B **21**, 953 (2003)
Electrical properties of aluminium oxide films deposited on indium-tin-oxide glasses.

[145] J. A. Thornton and G. E. McGuire, *Semiconductor Materials and Process Technology Handbook* (Noyes, New Jersey, 1988).

[146] D. W. Hoffman and J. A. Thornton, Thin Solid Films **40**, 355 (1977)
Internal stresses in sputtered chromium.

[147] D. W. Hoffman and J. A. Thornton, Thin Solid Films **45**, 387 (1977)
The compressive stress transition in Al, V, Zr, Nb and W metal films sputtered at low working pressures.

[148] R. Cueff, G. Baud, J. P. Besse, and M. Jacquet, Thin Solid Films **266**, 198 (1995)
Study of thin alumina coatings sputtered on polyethylene terephthalate films.

[149] P. Duchatelard, G. Baud, J. P. Besse, and M. Jacquet, Thin Solid Films **250**, 142 (1994)
Alumina coatings on PMMA: optimization of adherence.

[150] E. Caudron, G. Baud, J. P. Besse, G. Blondiaux, and M. Jacquet, Solid State Ionics **70/71**, 629 (1994)
Elaboration of ionic conductivity of Li-Al-O thin films.

[151] H. Windischmann, J. Appl. Phys. **62 (5)**, 1800 (1987)
An intrinsic stress scaling law for polycrystalline thin films prepared by ion beam sputtering.

[152] C. C. Fang, F. Jones, and V. Prasad, J. Appl. Phys. **74**, 4472 (1993)
Effect of gas impurity and ion bombardment on stress in sputter-deposited thin films: A molecular dynamics approach.

[153] L. I. Maissel and R. Glang, *Handbook of Thin Film Technology* (McGraw Hill, New York, 1970).

[154] B. Krause, Ph.D. thesis, Max-Planck-Institut für Metallforschung - Institut für Theoretische und Angewandte Physik der Universität Stuttgart, Stuttgart, 2002.

[155] H. Dosch, *Critical Phenomena at Surfaces and Interfaces*, Vol. 126 of *Springer Tracts in Modern Physics* (Springer, Heidelberg, 1999).

[156] Jens Als-Nielsen and Des McMorrow, *Elements of Modern X-ray Physics* (John Wiley & Sons, Ltd, New York, 2000).

[157] M. Tolan, *X-Ray Scattering from Soft-Matter Thin Films* (Springer, Heidelberg, 1999).

[158] B. E. Warren, *X-Ray Diffraction* (Addison-Wesley, New York, 1990).

[159] *X-ray and Neutron Reflectivity : Principles and Applications*, Vol. 58 of *Lecture notes in physics*, edited by Jean Daillant and Alain Gibaud (Springer, Berlin, 1999).

[160] R. Feidenhans'l, Surf. Sci. Rep. **10**, 105 (1989)
Surface structure determination by X-ray diffraction.

[161] U. Pietsch, V. Holý, and T. Baumbach, *High-Resolution X-Ray Scattering from Thin Films to Lateral Nanostructures* (Springer, Berlin, 2004).

[162] A. Gibaud and S. Hazra, Current Science **78**, 1467 (2000)
X-ray reflectivity and diffuse scattering.

[163] L. V. Azaroff, R. Kaplow, N. Kato, R. J. Weiss, A. J. C. Wilson, and R. A. Young, *X-Ray Diffraction* (McGraw-Hill, New York, 1974).

[164] Z. G. Pinsker, *Dynamical Scattering of X-Rays in Crystals* (Springer, Berlin, 1978).

[165] L. G. Parratt, Phys. Rev. **95**, 359 (1954)
Surface studies of solids by total reflection of X-rays.

[166] A. Guinier, *Théorie et technique de la Radiocrystallographie* (Dunod, Paris, 1956).

[167] J. M. Cowley, *Diffraction Physics* (North-Holland, Amsterdam, 1975).

[168] S. K. Sinha, E. B. Sirota, S. Garoff, and H. B. Stanley, Phys. Rev. B **38**, 2297 (1988)
X-ray and neutron scattering from rough surfaces.

[169] J. Als-Nielsen, D. Jacquemain, K. Kjaer, F. Leveiller, M. Lahav, and L. Leiserowitz, Phys. Rev. **246**, 251 (1994)
Principles and applications of grazing incidence x-ray and neutron scattering from ordered molecular monolayers at the air-water interface.

[170] G. Binnig and H. Rohrer, Sci. Am. **253**, 40 (1985)
The scanning tunneling microscope.

[171] G. Binnig, C. F. Quate, and C. Gerber, Phys. Rev. B **56**, 930 (1986)
Atomic force microscope.

[172] M. I. Alonso, M. Garriga, J. O. Ossó, F. Schreiber, E. Barrena, and H. Dosch, J. Chem. Phys. **119**, 6335 (2003)
Strong optical anisotropies of F_{16}CuPc thin films studied by spectroscopic ellipsometry.

[173] D. Garcia de Oteyza Feldermann, unpublished (2005).

[174] R. B. Campbell, J. M. Robertson, and J. Trotter, Acta Cryst. **14**, 705 (1961)
The crystal and molecular structure of Pentacene.

[175] C. C. Mattheus, A. B. Dros, J. Baas, G. T. Oostergetel, A. Meetsma, J. L. de Boer, and T. T. M. Palstra, Synth. Met. **138**, 475 (2003)
Identification of polymorphs of pentacene.

[176] R. G. Della Valle, A. Brillante, E. Venuti, L. Farina, A. Girlando, and M. Masino, Organic Electronics **5**, 1 (2004)
Exploring the polymorphism of crystalline pentacene.

[177] J. Krug, Adv. Phys. **46**, 139 (1997)
Origins of scale invariance in growth processes.

[178] A.-L. Barabási and H. E. Stanley, *Fractal Concepts in Surface Growth* (Cambridge University Press, Cambridge, 1995).

[179] T. Michely and J. Krug, *Islands, Mounds and Atoms. Patterns and Processes in Crystal Growth Far from Equilibrium* (Springer, Berlin, 2003).

[180] A. C. Mayer, R. Ruiz, R. L. Headrick, A. Kazimirov, and G. G. Malliaras, Organic Electronics **5**, 257 (2004)
Early stages of pentacene film growth on silicon oxide.

[181] B. Krause, F. Schreiber, H. Dosch, A. Pimpinelli, and O. H. Seeck, Europhysics Letters **65**, 372 (2003)
Temperature-dependence of the 2D-3D transition in the growth of PTCDA on Ag(111): a real-time x-ray and kinetic Monte-Carlo study.

[182] B. Krause, A. C. Dürr, F. Schreiber, H. Dosch, and O. H. Seeck, Surf. Sci. **572**, 385 (2004)
Late growth stages and post-growth diffusion in organic epitaxy: PTCDA on Ag(111).

[183] S. Kowarik, unpublished .

[184] K. Christmann, in *Introduction to Surface Physical Chemistry*, edited by H. Baumgärtel, E. U. Franck, and W. Grünbein (Steinkopff Verlag, Darmstadt, Springer Verlag, New York, 1991).

[185] D. P. Woodruff and T. A. Delchar, *Modern techniques of surface science* (Cambridge University Press, Cambridge, Great Britain, 1986).

[186] T. T. Magkoev and G. G. Vladimirov, J. Phys. Condens. Matter. **13**, L655 (2001)
Aluminium oxide ultrathin-film growth on the Mo(110) surface: a work-function study.

[187] A. Kuznetsova, I. Popova, V. Zhukov, J. T. Yates, Jr., G. Zhou, J. C. Yang, and X. Chen, J. Vac. Sci. Technol. A **19**, 1971 (2001)
Making superior corrosion resistant aluminum oxide films using ozone-electrochemial and electron microscopy studies.

[188] H. Pulker, *Coatings on glass* (Elsevier, Amsterdam, 1984).

[189] L. Parfitt, M. Goldiner, J. W. Jones, and G. S. Was, J. Appl. Phys. **77**, 3029 (1995)
Residual stresses in amorphous alumina films synthesized by ion beam assisted deposition.

[190] F. M. D'Heurle and J. M. E. Harper, Thin Solid Films **171**, 81 (1989)
Note on the origin of intrinsic stresses in thin films deposited via evaporation and sputtering.

[191] H. Paulus, W. Bolse, S. Meyer, J. Pflaum, S. Sellner, F. Schreiber, M. Fischer, B. Gompf, and G. Ulbricht, unpublished .

[192] M. Voigt and M. Sokolowski, Mat. Sci. Eng. B **109**, 99 (2004)
Electrical properties of thin rf sputtered aluminium oxide films.

[193] F. Family and T. Vicsek, J. Phys. A: Math. Gen. **18**, L75 (1985)
Scaling of the active zone in the Eden process on percolation networks and the ballistic deposition model.

[194] F. Family, J. Phys. A: Math. Gen. **19**, L441 (1986)
Scaling of rough surfaces: effects of surface diffusion.

[195] M. Kardar, G. Parisi, and Y.-C. Zhang, Phys. Rev. Lett. **56**, 889 (1986)
Dynamic Scaling of Growing Interfaces.

[196] F. Family, Physica A **168**, 561 (1990)
Dynamic scaling and phase transitions in interface growth.

[197] E. D. Wolf and J. Villain, Europhysics Letters **13**, 389 (1990)
Growth with surface diffusion.

[198] J. Chevier, V. L. Thanh, R. Buys, and J. Derrien, Europhysics Letters **16**, 737 (1991).

[199] Y.-L. He, H.-N. Yang, T.-M. Lu, and G.-C. Wang, Phys. Rev. Lett. **69**, 3770 (1992)
Measurements of Dynamic Scaling from Epitaxial Growth Front: Fe Film on Fe(001).

[200] C. Thompson, G. Palasantzas, Y. P. Feng, S. K. Sinha, and J. Krim, Phys. Rev. B **49**, 4902 (1994)
X-ray reflectivity study of the growth kinetics of vapor-deposited silver films.

[201] H. You, R. P. Chiarello, H.-K. Kim, and K. G. Vandervoort, Phys. Rev. Lett. **70**, 2900 (1993)
X-Ray Reflectivity and Scanning-Tunneling-Microscope Study of Kinetic Roughening of Sputter-Deposited Gold Films during Growth.

[202] J. Wang, G. Li, P. Yang, M. Cui, X. Jiang, B. Dong, and H. Liu, Europhysics Letters **42**, 283 (1998)
X-ray reflectivity and scanning-tunneling-microscopy study of surface roughness scaling of molybdenum films.

[203] G. W. Collins, S. A. Letts, E. M. Fearon, R. L. McEachern, and T. P. Bernat, Phys. Rev. Lett. **73**, 708 (1994)
Surface Roughness Scaling of Plasma Polymer Films.

[204] J.-P. Schlomka, M. Tolan, L. Schwalowsky, O. H. Seeck, J. Stettner, and W. Press, Phys. Rev. B **51**, 1995 (2311–2321)
X-ray diffraction from Si/Ge layers: Diffuse scattering in the regions of total external reflection.

[205] P. Viville, R. Lazzaroni, J. L. Brédas, P. Moretti, P. Samorí, and F. Biscarini, Adv. Mater. **10**, 57 (1998)
The Influence of Thermal Annealing on the Morphology of Sexithienyl Thin Films.

[206] R. Ben Chaabane, A. Ltaief, C. Dridi, H. Rahmouni, A. Bouazizi, and H. B. Ouada, Thin Solid Films **427**, 371 (2003)

Study of organic thin film transistors based on nickel phthalocyanine: effect of annealing.

[207] J. A. Thornton and J. Chin, Ceram. Bull. **56**, 504 (1977).

[208] P. Brüesch, R. Kötz, H. Neff, and L. Pietronero, Phys. Rev. B **29**, 4691 (1984)
Vibrational properties of Al_2O_3 films on gold, aluminium and silicon.

[209] K. Kristiansen, Vacuum **27**, 227 (1977)
A statistical approach to the analysis of dielectric breakdown strength of thin insulating films.

[210] R. G. Frieser, J. Electrochem. Soc. **113**, 357 (1966)
Phase Changes in Thin Reactively Sputtered Alumina Films.

[211] C. A. T. Salama, J. Electrochem. Soc. **117**, 913 (1970).

[212] I. H. Pratt, Solid State Technol. **12**, 49 (1969).

[213] A. L. Dragoo and J. J. Diamond, J. Am. Ceram. Soc. **50**, 568 (1967).

[214] K. Iida and T. Tsujide, Jpn. J. Appl. Phys. **11**, 840 (1973)
Physical and Chemical Properties of Aluminum Oxide Thin Film Deposited by $AlCl_3$-CO_2-H_2 system.

[215] C. Chatfield, J. N. Lindstrom, and M. E. Sjostrand, J. De Physique **C5**, 377 .

Danksagung

An erster Stelle möchte ich Herrn Professor Dr. Helmut Dosch für die Ermöglichung dieser Doktorarbeit in einem angenehmen Umfeld und unter exzellenten Arbeitsbedingungen danken.

Herrn Professor Dr. Jörg Wrachtrup danke ich für die Übernahme des Koreferats.

Für die interessante Aufgabenstellung, die gute Betreuung, die zahlreichen Diskussionen, die zum Gelingen dieser Arbeit beigetragen haben, und für das Korrekturlesen dieser Arbeit danke ich Herrn Professor Dr. Frank Schreiber.

Der Deutschen Forschungsgemeinschaft möchte ich für die finanzielle Unterstützung im Rahmen des Schwerpunktprogrammes 1121 "Organische Feldeffekt-Transistoren: strukturelle und dynamische Eigenschaften" danken.

Dr. Alexander Gerlach hat bei zahlreichen Synchrotron Experimenten mitgeholfen und mit zahlreichen Diskussionen an diesem Projekt mitgewirkt. Dafür möchte ich ihm an dieser Stelle danken.

Herrn Dr. Jens Pflaum möchte ich für die enge Zusammenarbeit, die zahlreichen Diskussionen und das Korrekturlesen dieser Arbeit danken. In seiner Gruppe wurden die thermische Desorptionsspektroskopie (TDS) Messungen durchgeführt. In diesem Zusammenhang möchte ich Stephan Meyer, der diese Messungen durchgeführt hat, danken. Außerdem möchte ich Stephan Hirschmann für das Aufreinigen der Moleküle danken.

Für die Bereitstellung ihrer Sputteranlagen, entsprechenden Einweisungen und Unterstützungen möchte ich Dr. Bruno Gompf und Matthias Fischer aus dem 1. Physikalischen Institut der Universität Stuttgart und Gerhard Ulbricht aus der Abteilung von Herrn Professor Dr. Klaus von Klitzing am Max-Planck-Institut für Festkörperforschung danken.

Beim ANKA-Team mit Dr. Andreas Stierle, Dr. Adrian Rühm, Dr. Nikolai Kasper und Ralf Weigel und bei Dr. Bernd Struth von der ID10B an der ESRF möchte ich mich für die Unterstützung während den Meßzeiten bedanken.

Marion Kelsch vom Max-Planck-Institut für Metallforschung möchte ich für die aufwendige Präparation der TEM-Proben und den entsprechenden Messungen danken.

Herrn Hartmut Paulus und Herrn Professor Dr. Wolfgang Bolse vom Institut für Strahlenphysik möchte ich für die RBS Messungen danken.

Der Arbeitsgruppe Dosch möchte ich für die angenehme Arbeitsatmosphäre danken.

Desweiteren möchte ich der Gruppe "organische dünne Schichten" in der Abteilung Dosch, allen voran Dr. Esther Barrena, Dimas Garcia de Oteyza Feldermann, Xuena Zhang, Tobias Krauss und den ehemaligen Arbeitskollegen Dr. Bärbel Krause, Dr. Volker Kruppa und Dr. Arndt Christian Dürr, für die angenehme Arbeitsatmosphäre und die zahlreichen Diskussionen und technischen Unterstützungen danken. Derselbe Dank richtet sich auch an Stefan Kowarik und Max Skoda aus der Arbeitsgruppe Schreiber. Besonders möchte ich meinem langjährigen Bürokollegen Herrn Dr. Josep Oriol Ossó de Torné für die zahlreichen wissenschafltichen und technischen Ratschläge, der Mithilfe bei verschiedenen Experimenten und auch für alle außerwissenschaftlichen Gespräche danken.

Zuletzt möchte ich mich herzlich bei meinen lieben Eltern und Brüdern für ihre ständige Unterstützung bedanken.